STUDY OF OPTICAL, ELECTRICAL AND MAGNETIC PROPERTIES OF $CoWO_4/PbWO_4$ NANOCOMPOSITES

THESIS

SUBMITTED TO

GOA UNIVERSITY

FOR THE AWARD OF THE DEGREE OF

DOCTOR OF PHILOSOPHY

IN

PHYSICS

BY

M. JEYAKANTHAN

UNDER THE GUIDANCE OF

PROF. UMA SUBRAMANIAN (Guide)

PROF. R. B. TANGSALI (Co-guide)

DEPARTMENT OF PHYSICS

GOA UNIVERSITY

TALEIGAO PLATEAU

GOA 403206

INDIA

FEBRUARY 2020

DECLARATION

I declare that this Ph.D thesis entitled ''**Study of optical, electrical and magnetic properties of $CoWO_4/PbWO_4$ nanocomposites**'' represents work which has been carried out by me and that it has not been submitted to any other University or Institution for the award of any Degree, Diploma, Associateship, Fellowship or any other such title.

Place: Goa University, Goa. **M. Jeyakanthan**

Date:

CERTIFICATE

We hereby certify that the above Declaration of the candidate M. Jeyakanthan is true and that this Ph.D thesis represents his independent work.

Prof. Uma Subramanian
(Research Guide)
Department of Physics,
Goa University, Goa.

Prof. R. B. Tangsali
(Co - Guide)
Department of Physics,
Goa University, Goa.

ACKNOWLEDGEMENT

I take the opportunity to acknowledge all those who have helped me directly or indirectly throughout my Ph.D research work in the Department of Physics, Goa University.

I have been very fortunate to be guided by **Prof. Uma Subramanian**, Professor, Department of Physics, Goa University, for her decisive advice and valuable guidance, motivation and encouragement throughout my Ph. D. tenure.

I would also like to extend my sincere thanks to my Co-guide **Prof. R. B. Tangsali** for his patience, help and understanding for the last five years and also for the valuable comments during the faculty research committee (FRC) meetings.

Special thanks to the members of FRC **Prof**. **V. M. S. Verenkar** my subject expert, School of Chemical sciences, **Prof. Gourish Naik,** Dean Faculty of Natural sciences and **Prof. A.V. Salkar,** Former Dean, Faculty of Natural sciences for their constructive suggestions during annual presentations.

I wish to express my thanks to **Prof. K. R. Priolkar,** Head, Department of Physics and **Prof. R.V. Pai,** former Head, Department of Physics, **Prof. R. B. Tangsali,** former Head, Department of Physics, Goa University for their support and providing experimental facilities in the Department of Physics.

I also thank **Prof. J. A. Erwin Desa** (former Head of the Department of Physics and former Dean of Faculty of Natural Sciences, Goa University), for his kind help, useful discussions and suggestions as and when it was needed.

I extremely thankful to **Prof. R. Wordenweber,** Peter Grünberg Institute (PGI) and JARA-Fundamentals of Future Information Technology, Jülich, Germany and **Dr. Bholanath Pahari**, Department of Physics, Goa University for their valuable discussions about Vogel – Fulcher law analysis.

I acknowledge **Prof. K. R. Priolkar** and **Dr. Venkatesha R Hathwar**, Department of Physics, Goa University for valuable discussion on thermoelectric study and helping to get crystal structure model from VESTA program respectively.

I express my deep gratitude to **Mr. Girish Prabhu and Mr. Areef Sardar**, NIO-Goa, for XRD and EDS measurements, **Mr. Madhusudan Lanjewar**, USIC, Goa University, for SEM measurements. Thanks to **Mr. Ramesh Chandra Prajapati** technical assistant at MNIT, Jaipur for zeta potential measurements. I am indebted to **Dr. Venkata Saravanan, Mr. Roshan Jose and Dr. A. Ramesh** Department of Physics, Central Univeristy of Tamilnadu for ferroelectric and electrochemical measurements. I am gratefull to **Mr. Pratik Asogekar** and **Miss. Prajothi Gouns Dessai**, School of chemical sciences, Goa University for helping me to do magnetic measurements.

I thank **Mr. Rahul Kerkar, Mr. Vishnu Chari, Mr. Chandan Naik, Mr. Vishal Pawar,** School of chemical sciences and **Miss. Prabha Tiwari, Mr. Dhillan, Miss. Shravani Korgaonkar, Miss. Rutuja Kolte,** Department of Botany for helping to get distilled water for my Ph.D work.

I extend my heartfelt thanks to all the **faculty members and research scholars, Department of Physics, Goa University** for their suggestions and discussions. I am

also extremely grateful to **Non-teaching staff** of the Department of Physics, Goa University.

I would like to thank **UGC- BSR** for providing Junior / Senior research fellowships and contingency for my Ph.D work.

DEDICATED TO MY FAMILY MEMBERS

CONTENTS

List of Figures

List of Tables

CHAPTER 1

GENERAL INTRODUCTION AND LITERATURE REVIEW

1.1. Introduction

Huge demands for solid state lighting devices along with multifunctional properties have been evaluated by several authors together with the performance of materials used in them. In the interest of reducing the energy demand of these appliances, extensive research has been carried out in search of alternative light sources. In the last decade researchers have explored many synthesis methods for ceramic nanophosphors to improve the emission intensity as well as other properties such as magnetic, electrical and thermoelectric properties. Nanophosphors are widely used in various potential applications such as white light emitting diodes (WLEDs), display devices, bioimaging, monitor screens, optoelectronics, therapeutics, lumino-magnetic applications and biological labelling and its demand increases day-by-day as novel devices keep emerging. A nanocomposite with interface of type I band alignment of two semiconductors is one of the best methods to improve emission intensity. In this chapter the importance of nanocomposites, types of band alignment, the basic phenomena of luminescence, energy transfer processes involved in tungstates, and a brief review of the studied system are discussed. An introduction to the electrical properties of this system along with scope and objective of the thesis are also examined.

1.2. Introduction to Nanocomposites

Nanocomposites are materials in which at least one of the phases or both phases show particles or crystallites in the nanometer range with different chemical, physical and mechanical properties [1]. Reducing the size of materials lead to a significant increase in optical, electrical, magnetic and thermoelectric properties.The properties of nanocomposites are not only dependent on their individual properties of different phases but also on their combined nature such as surface morphology and interfacial characteristics[2]. Some advantages of nanocomposites are summarized below:

- Improvement in mechanical properties such as tensile strength, flexibility, ductile strength, modulus and stability of dimension

- Higher thermal stability and heat distortion temperature
- Higher chemical and radiation hardness
- Higher electrical conductivity
- Enhanced thermoelectric power factor
- Enhanced photocatalytic and photoluminescence

Generally, the nanocomposites are classified into three different categories: ceramic matrix nanocomposites, metal matrix nanocomposites and polymer matrix nanocomposites [3]. Ceramic matrix nanocomposite consisting of a ceramic matrix combined with a ceramic (oxides, carbides) dispersed phase. Metal matrix nanocomposites refer to materials consisting of a ductile metal or alloy matrix in which some nanosized reinforcement material is implanted. Polymer nanocomposites are materials in which nanoscopic inorganic particles are dispersed in an organic polymer matrix. Energy of the surface/interface essentially controls the properties of materials. Interfaces provide inhomogeneity in solid materials and this cause significant change in their thermal, optical, electrical, magnetic and mechanical properties of the materials. Particular mixing of different phases of materials with different morphology as well as the high percentage of interface area lead to materials with enhanced properties [4].

1.3. Ceramic nanocomposites

The concept of ceramic nanocomposites was first reported in 1991 by Niihara et al [5]. According to Niihara, ceramic nanocomposites are classified into four categories: intragranular, intergranular, hybrid, and nano/nano composites. Except in the case of nano/nano composites, the matrix phase can be a microstructure ceramic or glass while reinforced phase can be nanoparticle, nanotube, nanoplatelets and hybrid of these materials. In nano/nano composites both the matrix and reinforced phase are composed of nano dimensions. The nano/nano composites are further divided by their material combination into two categories; semiconductor – semiconductor nanocomposites, semiconductor – metal nanocomposites. Conjoining two or more semiconductors in single composite material with adjustable band alignment leads to develop a new degree of multifunctional nanocomposites. According to the band alignments, the semiconductor-semiconductor nanocomposites are

divided into three types [4]: 1.Type I band alignment, 2. Type II band alignment and 3.Type III band alignment as shown in the Fig. 1.1.

Type I band alignment nanosystems are assembled by mixing two semiconductors in such a way that conduction and valence band positions of one semiconductor is falling entirely within the band gap of another semiconductor to create an interfacepotential barrier. In type II band alignment nanocomposites the conduction band of the smaller band gap material might lie above that of the larger band gap material or its valence band might lie below that of the larger gap material. Type II band alignment in systems lead to electron-hole separation and these nanocomposites are potential candidates for photocatalytic and solar cell applications. The type III is identical to Type II except for the much more pronounced difference in valence band and conduction band positions which gives a higher driving force for charge transfer[6–8].

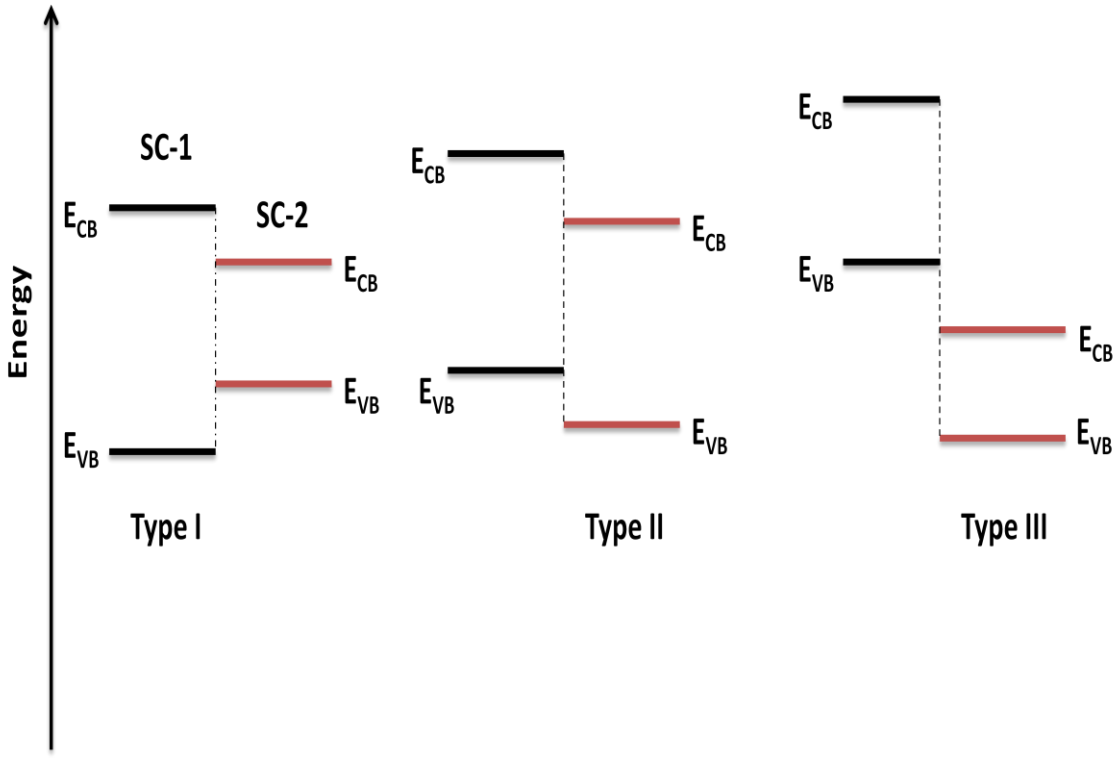

Fig. 1.1. Band alignments of the semiconductor – semiconductor nanocomposites. SC-1, SC-2, E_{VB}, E_{CB} in figure represents the semiconductor 1, semiconductor 2, valance band position and conduction band position respectively.

1.4. Introduction to Luminescence

Luminescence is the emission of light from the substance when electrons in the substance are excited by some form of energy. The term luminescence is introduced by Weidmann in 1888. Luminescence is a process in which part of absorbed energy isre-emitted in the form of electromagnetic radiation in the ultraviolet, visible and near visible region of the spectrum. The process of luminescence contains two steps which are the excitation of the electron and the subsequent emission of photons [9]. Based on the source of excitation energy, the luminescence is classified into the following types[10].

- Photoluminescence – Excitation by photon
- Electroluminescence - strong electric field
- Cathode luminescence – impinging high energy electron beam
- Chemiluminescence – due to chemical reactions
- Thermoluminescence - thermally stimulated emissions from the already excited samples
- Mechanoluminescence - excited by mechanical action on the solid

Among all the types, photoluminescence is the main interest of this research in which higher energy photons are absorbed by phosphors and re-emitted as a photons having lower energy.

1.4.1. Photoluminescence

Photoluminescence (PL) is a process in which molecules of matter absorb energy when they are excited by photons and then emit the energy in the form of the photons as the excited electrons return to their lower energy state. Generally, the energy of an emitted photon is lower than the exciting photon [11]. Photoluminescence can be either fluorescence or phosphorescence based on their average lifetime of the excited state which is much larger ($>10^{-8}$S) for phosphorescence than fluorescence. PL spectra of the molecular species are different from PL spectra of the atomic species. There are several possibilities of the electrons returning from the excited state to the ground state. The processes competing in luminescence are radiative and nonradiative transitions [9,12].

1.4.2. Radiative transition

Radiative transition can be explained through Franck-Condon principle. The configuration coordinate diagram is shown in Fig. 1.2.

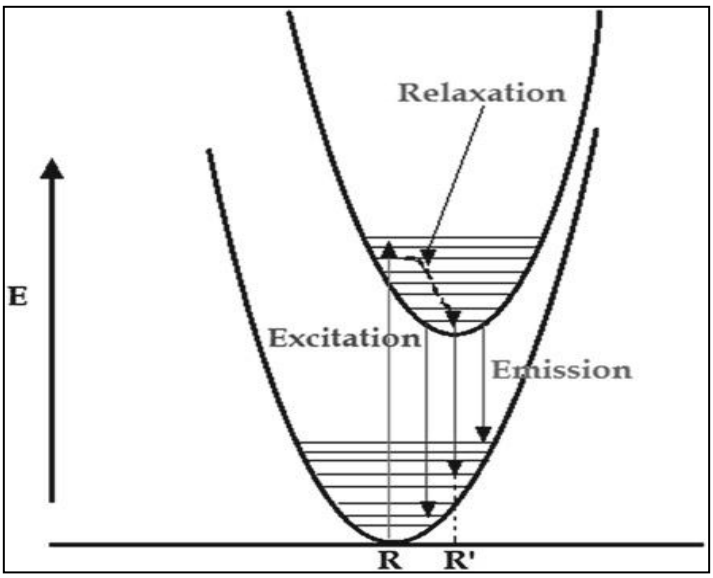

Fig. 1.2.Radiative transition (**From**:*Kartik N. Shinde, S.J. Dhoble, H.C. Swart and Kyeongsoon Park (2012), Basic Mechanisms of Photoluminescence. In: Phosphate Phosphors for Solid-State Lighting. Springer Series in Materials Science ,Springer, Berlin.)*

When the material is excited, the electron jumps from ground state to excited state, which has a higher vibrational level than vibrational level of the ground state. The electron relaxes very fast to the lowest vibrational level of the excited state, giving up the excess energy to vicinity. This relaxation process usually occurs nonradiatively. From the lowest vibrational level of the excited state, the electron returns to the ground state by means of photon emission. Therefore the emission wavelength is longer than the excitation wavelength. The difference in energy between the maximum of emission and excitation band is called Stoke shift.

1.4.3. Non-radiative transition

The energy absorbed by the luminescent materials during excitation, which is not emitted as radiation and it is dissipated to the crystal lattice, is characteristic of non-radiative transition. The non-radiative transition is also explained by the configurational coordinated diagram as shown in Fig. 1.3. From Fig. 1.3(a) we can observe the Stoke shift between the ground state and excited state. If the temperature is high enough the relaxed-excited state [11] may reach the crossing of the parabolas. So the excited electron can return to the ground state through the crossing in a non-radiative manner. The excitation energy is transferred as heat to the lattice during the nonradiative process.

In Fig. 1.3(b), the parabolas are parallel and will never cross. It is impossible to reach the ground state in the way described for Figure 1.3(a). However, also here non-radiative return to the ground state is possible if certain conditions are fulfilled, viz. the energy difference ΔE is equal to or less than 4-5 times the higher vibrational frequency of the surroundings. In that case, this amount of energy can simultaneously excite a few high-energy vibrations and is then lost for the radiative process. Usually this non-radiative process is called multi-phonon emission.

In Fig. l.3(c) both processes are possible in a three-parabolas-diagram. The parallel parabolas will belong to the same configuration so that they are connected by forbidden optical transitions only. The third one originates from a different configuration and is probably connected to the ground state by an allowed transition. This situation occurs often. Excitation (absorption) occurs now from the ground state to the highest parabola in the allowed transition. From here the system relaxes to the relaxed excited state of the second parabola. Fig. 1.3(c) shows that the non-radiative transition between the two upper parabolas is easy. Emission occurs now from the second parabola[13].

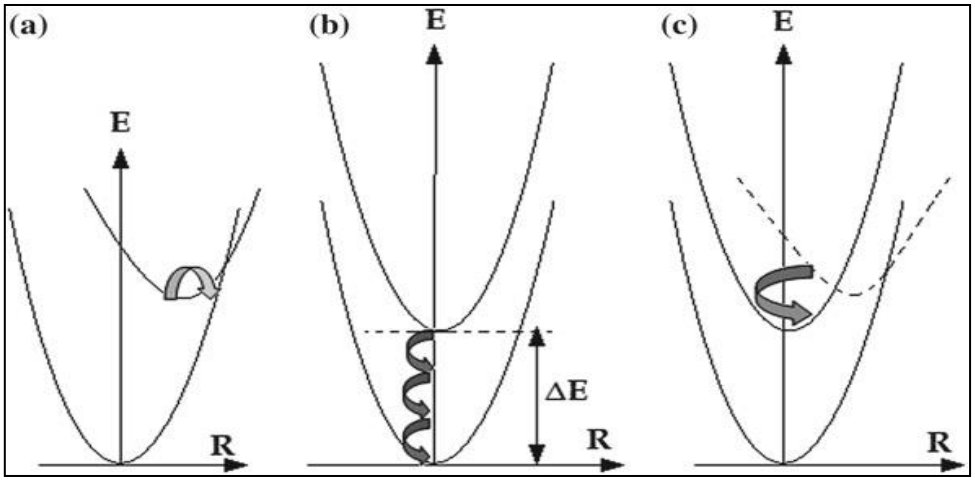

Fig. 1.3. Non-radiative transition(**From**:*Kartik N. Shinde, S.J. Dhoble, H.C. Swart and Kyeongsoon Park (2012), Basic Mechanisms of Photoluminescence. In: Phosphate Phosphors for Solid-State Lighting. Springer Series in Materials Science, Springer, Berlin.)*

1.5. Introduction to the Tungstates

Tungstates are a class of ternary oxides and they are self activating luminescence materials. Along with tungstates, other ternary oxides such as molybdates, vanadates are also self activators [14–16]. Metal tungstates are an important class of self-activated luminescent materials and some also act as a host material for rare earth doping for luminescence applications [17–20]. They crystallize into two structures based on their cationic radii, i.e., wolframite ($r < 0.77$ Å) and scheelite ($r > 0.90$ Å) [21,22].

In scheelite structure, W ion is coordinated with four oxygen atoms forming tetrahedral coordination while bivalent cation is coordinated with eight oxygen atoms forming polyhedral coordination as shown in Fig. 1.4(a). $CaWO_4$, $SrWO_4$, $BaWO_4$, $PbWO_4$ etc are examples of scheelite type tungstates. In wolframite structured tungstates the tungsten ion is coordinated with six oxygen atoms forming the octahedral coordination while bivalent cation also forms the octahedral coordination. The crystal structure of the wolframite tungstate is shown in Fig. 1.4(b). $CoWO_4$, $NiWO_4$, $MgWO_4$, $MnWO_4$, $FeWO_4$, $CdWO_4$ are some examples of wolframite tungstates. The intrinsic luminescence of scheelite and wolframite arises due to annihilation of the self-trapped exciton (STE), which forms excited $[WO_4]^{2-}$ or $[WO_6]^{6-}$ complexes respectively [23,24]. Some of the divalent transition metal

tungstates have also gained commercial interest in lasers and fluorescent lamps [15,25]. In addition, these materials also find applications as catalysts and humidity sensors[26–28].

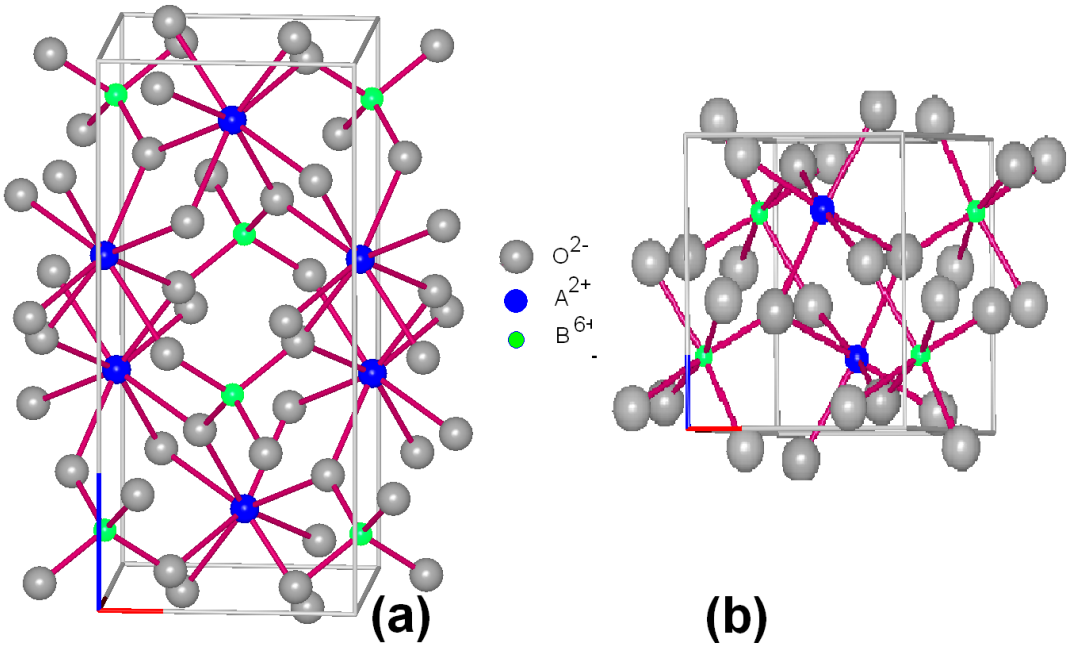

Fig. 1.4. The conventional unit cell of (a) Scheelite and (b) wolframite structures. A, B and O are the metal cations, tungsten and oxygen respectively [**From**: *https://shodhganga.inflibnet.ac.in/bitstream/10603/4722/11/11_chapter%201.pdf*].

1.6. Excitonic emission

Bound state of an electron-hole pair which is attracted to each other by electrostatic force is called exciton. An exciton is formed when energy is absorbed by the semiconductors or insulators. Electron from the valence band goes to the conduction band leaving behind a hole in valence band forming a free electron – hole pair. Free electron and free hole can form a bound pair state called as an exciton. Recombination of bound electron – hole pair gives rise to excitonic emission having energy equal to band gap energy – exciton binding energy [11]. Excitons are classified into three basic types such as Frenkel exciton, Wannier-Mott exciton and charge transfer exciton [29]. Wannier–Mott excitons extend over many lattice constants and are free to move through the lattice, while Frenkel excitons have a radius comparable to the interatomic distance. Frenkel excitons are localized and resemble an atomic excited state.

Charge transfer (CT) excitons are formed when an electron and a hole occupy adjacent molecules. They occur primarily in organic and molecular crystals; in this case, unlike Frenkel and Wannier excitons, CT excitons display a static electric dipole moment. The energy level diagrams of $CoWO_4$ and $PbWO_4$ are given in Fig. 1.5(a) and Fig. 1.5 (b) respectively [30,31].

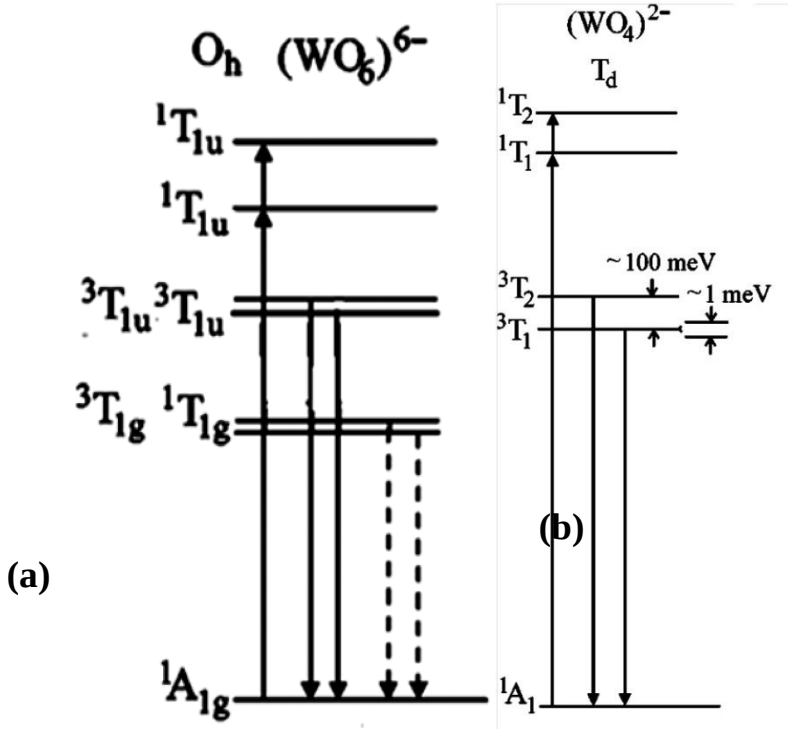

Fig. 1.5 (a) Energy level diagram of $CoWO_4$**(b)** Energy level diagram of $PbWO_4$

1.7. Self-trapped exciton

The self-trapped excitons play an important role in the intrinsic luminescence of tungstates [23,32]. In semiconductor and insulators, the excitons interact with lattice. If the interaction is strong enough, the exciton may cause lattice to distort, which strongly diminishes the movement of exciton across the crystal. Distortion of the lattice generally occurs for a lattice having weak bonds. This process is called self-trapping of the exciton. When the interaction is strong, the corresponding intrinsic luminescence spectrum will be broad. Exciton self-trapping process can be explained in the following way: the translational movement of the exciton is driven by its hole. The movement of the heavy hole is then very slow. The hole thus strongly polarizes the surrounding lattice and thereby its movement is

further slowed down resulting in a total localization of the hole close to some atom constituting the host lattice. A light electron accompanying the hole will then describe its orbit in the close vicinity.

1.8. Charge transfer luminescence

Charge transfer luminescence plays an important role in tungstate materials. In the case of charge transfer, the optical transition takes place between different kinds of orbitals or between electronic states of different ions. During this process charge distribution on the optical centre is changed and chemical bonding also changes considerably [33–35]. Due to this very broad emission spectra are expected. Very well-known examples are scheelite and wolframite type tungstates such as $CaWO_4$, $PbWO_4$ and $MgWO_4$. These materials have been used for decades for the detection of X-rays, scintillators and fluorescent lamps which show luminescence originating from the $[WO_4]^{2-}$ and $[WO_6]^{6-}$ groups. The transition involves charge transfer from oxygen ions to empty d-levels of the tungsten ion. In these materials, no intentional dopant is introduced and for this reason, it is also called as self-activated materials.

There are two types of charge transfer mechanisms involved in metal tungstates: Metal to ligand (MLCT) charge transfer and ligand to metal charge transfer (LMCT) [36] as shown in Fig. 1.6 (a) and 1.6 (b) respectively. The scheelite type tungstates with $[WO_4]^{2-}$ anion have a characteristic ligand to metal charge transfer (LMCT) [37]. In this transition, an electron is transferred from the highest occupied molecular orbital (HOMO) which has oxygen 2p nonbonding orbital character to the lowest unoccupied molecular orbital (LUMO), which is an antibonding orbital with W 5d orbital parentage. The tungsten environment in the wolframite structure is not the isolated tetrahedron as found in $CaWO_4$; nevertheless, LMCT transitions are still an important contributor to the optical absorption of these compounds. Metal to ligand charge transfer arises from the transition of an electron from the molecular orbital with metal-like character to those with ligand like character. Furthermore, the presence of cation with partially filled d orbital of transition metal tungstates leads to familiar d-d transition. A third possibility is transfer of electrons from the partially filled d-orbitals of the cation to the empty W 5d based molecular orbitals on the tungstate group. Because this effectively amounts to the transfer of an electron from the A^{2+} cation to the W^{6+} ion, this transition can be labelled a metal to metal charge transfer (MMCT) [36].

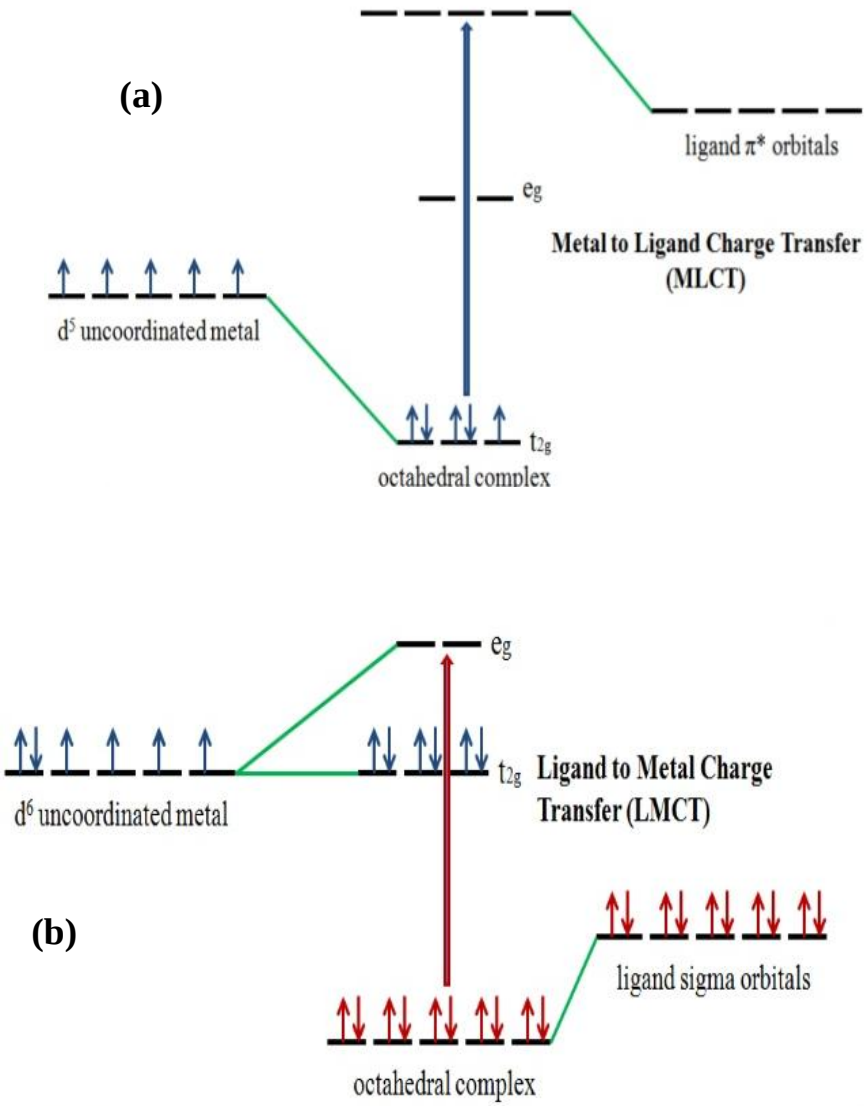

Fig. 1.6.(a) Metal to ligant charge transfer (b) Ligand to metal charge transfer

1.9. Introduction to dielectric properties

Tungstates are one of the special classes of ceramic materials for electrical applications. All the tungstates are insulators. It is well known that dielectric properties of ceramic materials depend on their composition, structure and experimental conditions [38]. This section presents a brief description of dielectric materials and its mechanism and corresponding theory as well as a ferroelectric phenomenon. The crystalline dielectric materials are classified into two major categories[39]:

- Polar (dipole) dielectrics
- Non-polar (neutral) dielectrics

A permanent polarization (P_s) exists in polar dielectrics even without an external electric field. No such permanent polarization observed in non-polar dielectrics [40]. Dielectric material is commonly known as an insulator. It can store the electrical energy by resisting the current flow in the circuit. The dielectric response arises from the short-range motion of charge carriers under the influence of an externally applied electric field while capacitance is a measure of the ability of any two conducting plates in proximity to store a charge Q when a potential difference V is applied across them. The capacitance C is given as,

$$C=Q/V \qquad (1.1)$$

For a dielectric material placed between the plates of a capacitor, it may be shown that: The capacitance of the capacitor without the dielectric is given by

$$C_0 = \varepsilon_0 A/L \qquad (1.2)$$

The capacitance of the capacitor with dielectrics is termed as

$$C = \varepsilon A/L \qquad (1.3)$$

where ε, L and C are permittivity or dielectric constant, thickness and area of the dielectric materials respectively.

1.9.1. Dielectric relaxation

In dielectric material, the change of polarization is time dependent process and given by the equation

$$P(t) = P_0[1-\exp(-t/\tau)] \qquad (1.4)$$

where P_0 is a maximum polarization and τ is the relaxation time for relaxation of the polarization (dielectric relaxation). The relaxation time varies for different polarization processes. The space charge polarization is the slowest process as it involves the diffusion of ion over several inter-atomic distances. The relaxation time for this process is based on the jump of the ions during the applied electric field. Typical frequency of applied ac electric field for this process is 10^2 Hz. If the frequency of electric field is increased, the space charge

polarization diminishes and dipole orientation polarization occurs. The orientation polarization dominates from the audio frequency range [22] till tens of MHz. If frequency is increased above tens of MHz, the ionic polarization dominates till 10^{13} Hz. Above this frequency, electronic polarization dominates till 10^{15} Hz. Typical frequency dependence of different polarization processes is shown schematically in Fig. 1.7.

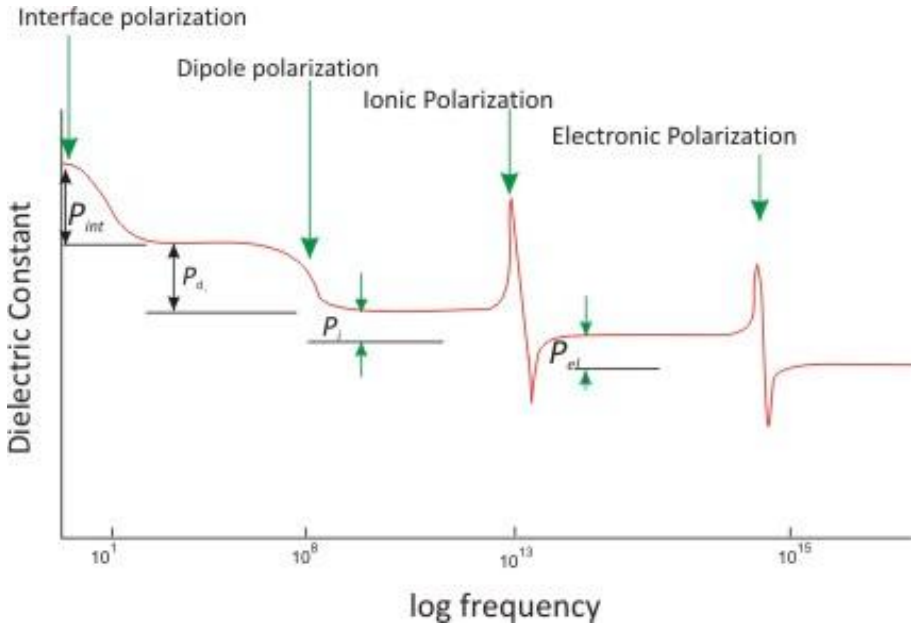

Fig. 1.7. Variation of polarization with frequency.

1.9.2. Maxwell - Wagner polarization effect

The Maxwell–Wagner (MW) effect reveals the charge buildup at the interface of the two materials or interface between the sample and electrodes. This effect is on the basis of charge carrier relaxation times in the two materials and this effect is commonly known as interfacial charging effect. This will occur especially at low frequencies. The real and imaginary part of the dielectric for MW model is given by the following equations [41]

$$\varepsilon'(\omega) = \frac{1}{C_0(R_i+R_b)} \frac{\tau_i+\tau_b-\tau+\omega^2\tau_i\omega_b\tau}{1+\omega^2\tau^2} \qquad (1.5)$$

$$\varepsilon''(\omega) = \frac{1}{\omega C_0(R_i+R_b)} \frac{1-\omega^2\tau_i\tau_b+\omega^2\tau(\tau_i+\tau_b)}{1+\omega^2\tau^2} \qquad (1.6)$$

where$\tau_i = C_i R_i$

$$\tau_b = C_b R_b$$

$$\tau = \frac{\tau_i R_b + \tau_b R_i}{R_i + R_b} \qquad (1.7)$$

where τ_i, τ_b, C_i, C_b, R_i, $R_b$are relaxation times, capacitance, resistance respectively and subscript *i* and *b* refers to the interfacial-like and bulk like layers, respectively.

1.10. Space charge layer (SCL) in nanocomposites

In nanocomposites, crystalline symmetry is broken at interfaces between two grains (homophase interface) or between two different phases (heterophase interface), resulting in a local space charge region due to the redistribution of ionic and electronic defects [42]. Ionic defects from the bulk phases adjacent to the interface are depleted in the space charge region, while those with opposite charge are accumulated [2]. In the case of an oxygen-ion conductor with Frenkel equilibrium for the anionic sublattice, segregation of interstitial oxygen ions at the phase boundary increases the concentration of oppositely charged point defects (oxygen vacancy) in the space charge region. The fundamental concept is that ions can be trapped at the interface core. (This process is equivalent to a segregation phenomenon.) The counter species, in general a trapped ion vacancy, is then accumulated in the adjacent space charge regions. Driving force is the chemical affinity of a second phase to the trapped ion.

1.11. Ferroelectricity

A material which is consisting of permanent electric dipole moment with spontaneous polarization is called ferroelectric materials. The arrangement of cations and anions within the ferroelectric gives rise to dipole moments within each unit cell. A unique property of ferroelectric material is hysteresis behaviour in polarization vs. electric field. Spontaneous polarization exists even after the removal of electric field and is called remnant polarization, P_r. Ferroelectric materials getting transformation from ferroelectric to paraelectric at certain temperature is called Curie temperature (T_C). Paraelectric materials will behave as a normal dielectric with no hysteresis [43].

1.12. Relaxor ferroelectrics (RFE)

Relaxor is a unique trait of disordered ferroelectric (FE). It can be prepared either in polycrystalline or single crystalline materials. Relaxors are also utilized in non-linear optic applications because an extraordinarily large electro-optic Kerr effect can be observed even in the so-called paraelectric state. Most of the relaxor ferroelectrics are perovskite type and tungsten bronze type structure. Upon cooling, the relaxor materials transform into the ergodic state**,** in which polar nano-regions are randomly distributed along directions of dipole moments**,** appears [44]. The temperature corresponding to the transformation is called Burn's temperature (T_B). The polar nano-region is mobile and behaves like an ergodic state at temperature close to T_B. When the ferroelectric materials are undergoing cooling**'**the dynamics of the polar nano-region becomes frozen at low temperature, this temperature is called freezing temperature. Polar nanoregions (PNRs) are widely believed to be responsible for the unusual physical properties of relaxor ferroelectrics, such as the strong frequency dispersion of the dielectric constant and the freezing-in of the polarization below the temperature peak in the dielectric constant T_m. They typically appear below the Burns temperature T_B as a consequence of strong compositional fluctuations found in relaxors. On cooling, the number, size (some of them) and the interaction of the PNRs increase. The increase of such interactions promotes the freezing of some regions around certain temperatures below T_m, known as the freezing temperature (T_f).

Because of the diffuseness in the dielectric anomaly, relaxors are often called "ferroelectrics with diffuse phase transition" though no structural transition really occurs [45]. The relaxor behaviour was first observed in perovskite compounds due to the disorder of non-isovalent ions e.g. $Pb(Mg_{1/2}Nb_{2/3})O_3$ (PMN- lead magnesium niobate) [46].

1.13. Introduction to thermoelectricity

Thermoelectricity refers to the class of phenomena in which a temperature difference creates an electric potential or an electric potential creates a temperature difference. The first important discovery relating to thermoelectricity was made in 1821 when a German scientist, Thomas Seebeck, found that electric current continuously flows in a closed circuit made up of two dissimilar metals, provided that the junctions of the metals are maintained at two different temperatures.

1.13.1. Seebeck effect

"The Seebeck effect is a phenomenon in which temperature difference between two dissimilar electrical conductors or semiconductors produces a voltage difference between the two substances".

Under the external heat to one conductor or semiconductors, the hot electrons flow toward the cooler side. If the pair is connected through an electrical circuit, direct current (DC) flows through that circuit. An electron in solids carries an electrical current as an elementary particle with a negative charge of e (<0). Since an enormous number of electrons are at thermal equilibrium in solids, they carry heat and entropy at the same time. Thus in the presence of temperature gradient, they can flow from a hot side to a cold side to cause an electrical current. This implies a coupling between thermal and electrical phenomena, which is known as the thermoelectric effects.

Thermopower studies are used as sensitive probes of transport mechanisms. The sign of thermopower (Seebeck coefficient)depends on the (i) sign of the charge carriers, unlike electrical and thermal conductivities (which depend on the magnitude of the charge), and (ii) energy dependence of the momentum relaxation time of the scattering mechanism at Fermi energy. It has two contributions, namely, diffusion thermopower (S_d) and phonon drag thermopower (S_p)**.** The total = $S_d + S_p$**.** Under a temperature gradient, diffusion of electrons through the specimen which leads to setting up an electric field produces, S**.** A state of equilibrium is established between electrons moved down the temperature gradient and electrostatic repulsion due to excess charge at the cold end arises due to flow of phonon wind dragging electrons due to electron-phonon coupling from hot end to the cold end.

1.13.2. Thermoelectric power factor

Thermoelectric power factor (P) defined as the multiplication of squared thermopower with DC electrical conductivity (σ) and is given by

$$P = S^2\sigma \ (W/mK^2) \qquad (1.8)$$

Thermoelectric materials with a higher power factor are able to generate more energy (move more heat or extract more energy from that temperature difference) this is only true for a thermoelectric device with fixed geometry and unlimited heat source and cooling. The efficiency of the thermoelectric materials

$$ZT = S^2 \sigma T/k$$

$$ZT = PT/ k \qquad (1.9)$$

The higher value of power factor and low value of thermal conductivity (k) leads to massive efficiency of thermoelectric (TE) materials as well as devices. Thermoelectric materials are characterized by ZT, that is, they show large Seebeck coefficient, high conductivity, and low thermal conductivity at the same time. Such requirements are difficult to be satisfied, because the three parameters are functions of carrier concentration, which cannot be tuned independently. The S decreases with increasing carrier concentration while σ increases. As a result, the carrier concentration takes an optimum value for maximizing the power factor $S^2\sigma$. In other words, conventional metals have very small Seebeck coefficient, while conventional semiconductors have very low conductivity. Hence, an optimum carrier concentration is evaluated to be 10^{19}–10^{20} cm^3 that is a typical carrier concentration of degenerate semiconductors. Once the carrier concentration is set to be the optimum value, the only way to maximize the conductivity is to maximize the mobility.

1.13.3. Interfacial energy barrier scattering

The strategy of rationally engineering semiconductor interfaces could enhance the thermoelectric figure of merit ZT in thermoelectric (TE) materials with the heterostructures, where the significant enhancement performance is believed to result from the growth of the Seebeck coefficient by the preferential scattering of low-energy carriers more effectively than high ones and the reduction of the thermal conduction via scattering phonons at the heterostructured interfaces. Carrier energy filtering effect in TE nanocomposites was reported to be one promising way to effectively improve the TE performance. This effect was elucidated in the way that the low-energy carriers in the composites could be selectively scattered by the energy barriers between the component interfaces, which would be over passed by the high-energy carriers.

1.14. Literature review on the studied system

Tungstate materials have aroused much interest because of their, structural properties and potential applications in the fields of luminescence, microwave, electrical, optical, scintillating, magnetic, photocatalytic and humidity sensing. There exist two types of structure in tungstates: wolframite and scheelite. As a self-activating phosphor, tungstate has some advantages, e.g., high chemical stability, high X-ray absorption coefficient, high light yield, and low afterglow to luminescence. Its luminescence originates due to the intrinsic structure which resulted in the charge transfer from excited 2p orbits of O^{2-} to the empty orbits of the central W^{6+} ions, and due to the structural defects. This section explores the brief review of the studied system $CoWO_4$ and $PbWO_4$ nanomaterials.

Among the wolframite structure tungstates, cobalt tungstate ($CoWO_4$) aroused much attention in the electrical, optical and photocatalytic applications. $CoWO_4$ crystallized into wolframite monoclinic structure. Moreover, the tungsten ion surrounded by six oxygen atoms whilst cobalt ion also preferred octahedral coordination and surrounded by six oxygen atoms.

In 1947 luminescence study of bulk tungstates and molybdates of calcium, strontium, magnesium was reported by F.A.Kroger [47]. Very few studies are reported for luminescence on $CoWO_4$ nanomaterials. Ce doped $CoWO_4$ nanomaterial shows 40 times better luminescence intensity as compared to the bulk $CoWO_4$ [48]. Upconversion luminescence of $CoWO_4$ nanomaterials is first time reported by Uma et al [49]. The blue-green emission at 495 and 530 nm are due to electronic transition from two close $^3T_{1u}$ levels to $^1A_{1g}$ and from T_{1g} to $^1A_{1g}$ allowed partly from spin-orbit coupling, respectively and strong NIR(near-infrared) emission also observed in cobalt tungstate nanowires[30]. Solid state studies on Cu doped $CoWO_4$ shows blue-green emission centered at 468 nm and DC conductivity changed from extrinsic to intrinsic at higher temperature[50]. Sodium dodecyl sulfate(SDS) assisted synthesis of $CoWO_4$ nanorods shows very strong emission peak at 453 nm and this SDS method may be used in other tungstate preparation[51]. Yb doping in $CoWO_4$ reduces the intrinsic emission of $CoWO_4$ and interestingly undoped and Yb doped samples show weak ferromagnetic nature at room temperature[52]. Facile hydrothermal approach for large scale synthesis yields 10-30 nm of diameter and 100-300 nm length of $CoWO_4$ nanorods[53]. Doping effect on optical bandgap and photoluminescence of Nd doped $CoWO_4$ nanomaterials studied by Juliet Josephine Joy. J et al[54]. The presence of 18 Raman active modes observed

in Mn-doped $CoWO_4$ with rod-like morphology[55]. Spray pyrolysis synthesis of cobalt tungstate nanomaterials has shown narrow PL peak at 411-419 nm[56]. $CoWO_4$ on silk material prepared by ultrasound irradiation was found to possess significant antibacterial activity and also the size of $CoWO_4$ nanoparticles were the key factors for influencing the fluorescence property of the products[57]. Particle size and sintering temperature dependent photoluminescence (PL) of cobalt tungstate nanomaterials were prepared by molten salt method[58]. Enhanced PL intensity of $CoWO_4$ nanomaterial in $CoWO_4/PbWO_4$ nanocomposites reported by Jeyakanthan et al. The mechanism of enhanced PL emission for the $CoWO_4/PbWO_4$ nanocomposites can be attributed to charge transfer between $[WO_4]^{2-}$ and $[WO_6]^{6-}$ complexes due to intra particle agglomeration leading to possible interface[59].

Cobalt tungstate nanomaterials are also beneficial materials for photocatalytic applications due to easy electron-hole formation. The enhanced photocatalytic studies of $CoWO_4$ with composites as well as doping are reported by many authors. The greatly enhanced photocatalytic activity (3–8 times) of $CdS/CoWO_4$ is due to the efficient separation of electron-hole pairs by the heterojunction structure and strong visible light absorption of CdS [60]. A novel $CoWO_4/CdS$ binary photocatalyst is synthesized by an in-situ hydrothermal method, and the enhanced activities of H_2 production and dye degradation are attained [61]. Tungstates have been very scarcely studied as photocatalysts for the production of hydrogen from the dissociation of the water molecule. Metal transition tungstates can be considered as potential photocatalysts for H_2 production via the splitting of the water molecule under visible light irradiation[62]. The optical properties and photocatalytic activity of these tungstates strongly depend on the nature of the transition metal [63]. Photodegradation of methanol and 4-chlorophenol was used to evaluate the photoactivity of the transition metal tungstate [64]. The essential parameters such as the amount of catalyst, dye concentration and initial pH influence the photocatalytic efficiency of $CoWO_4$[65]. Oxygen evolution reaction on nanosized $CoWO_4$ and $NiWO_4$ has been done through electrochemical impedance spectroscopy[66]. A series of novel magnetically separable $Fe_3O_4/ZnO/CoWO_4$ nanocomposites with different contents of $CoWO_4$ were fabricated using a facile refluxing method at 96 °C for enhanced photocatalytic as well as magnetic applications[67]. Nanosized $CoWO_4$ act as an efficient oxygen evolution

electrocatalysts with superior to several other Co based oxides recently reported [68]. Novel magnetic visible-light-driven photocatalyst $TiO_2/Fe_3O_4/CoWO_4$ with significantly enhanced catalytic activity through p-n heterojunction reported for degradation of Rhodamine B(RhB) pollutants[69]. Approximately 94% brilliant green dye degraded with 120 minutes of visible light irradiation with highly crystalline cobalt tungstate nanomaterials [70].The photocatalytic activity of $Fe_3O_4/CoWO_4$ magnetic nanocomposites was investigated by degradation of rhodamine B (RhB) in aqueous solution under visible light irradiation. The results indicate that about 98% of RhB was degraded after 180 min[71]. The theoretical work related to first principle study of $CoWO_4$ as oxygen evolution reaction catalyst reported by Chen Ling et al [72].

Electrical transport study of $CoWO_4$ single crystal prepared with solid-state sintering method studied by Bharathi et al and they explained about electrical conduction as well as a thermoelectric study [73]. At lower temperature the hopping of charge carrier in the narrow 3d band and at high temperature normal band like conduction in the 2p band are responsible conduction mechanisms in $CoWO_4$ bulk materials. Previous researchers have reported that $CoWO_4$ is a p- type semiconductor [30,73–75]. This is due to the commonly present Co^{3+} impurities in $CoWO_4$. Hole polarons hopping and band type conduction are the conduction processes in $CoWO_4$ at low and higher temperatures respectively. The optical and dielectric study of $CoWO_4$ nanomaterials were reported by Sagadevan et al [76]. The microwave dielectric study of MWO_4(where M= Mg, Zn, Ni, Co) bulk ceramics were reported and higher quality factor observed for $CoWO_4$ and $ZnWO_4$[77]. Colossal dielectric constant observed for $MPr_2W_2O_{10}$ tungstates (M = Cd, Co, Mn) due to those ions which have unscreened electrons on the unfilled shells [78]. The effect on sintering of CuO modified $CoWO_4$ reported [79] and it becomes a promising candidate for low temperature co-fired ceramics (LTCC) application. S.Shanmugapriya et al briefly given the electrical and magnetic properties of cobalt tungstate nanomaterial prepared by sonochemical method [80].

Magnetic properties of $CoWO_4$ bulk and nanomaterials are studied by few authors. In 1969, the experimental and theoretical investigations on magnetic properties of bulk cobalt tungstate are detailed studied and antiferromagnetic nature observed at low temperature[81]. Heat capacities of antiferromagnetic $CoWO_4$ bulk materials briefly explained by C.P. Lande et al [82]. Spatial distribution of magnetization in cobalt tungstate has been explored [83].

Room temperature paramagnetic and antiferromagnetic below the Neel temperature was observed for bulk as well as nano $CoWO_4$ by many authors[80,84,85]. Interestingly magnetic properties of Yb doped $CoWO_4$ nanomaterial shows ferromagnetic nature [52]. The antiferromagnetic transition temperature is lowest for $CoWO_4$ nanomaterials due to crystallite size effect[80]. Room temperature superparamagnetism was observed $Fe_3O_4/CoWO_4$ nanocomposites [71]. Local symmetry and magnetic anisotropy of antiferromagnetic $CoWO_4$ has been studied by soft X-ray absorption spectroscopy. The orbital moment of the $CoWO_4$ is responsible for the collinear antiferromagnetism [86].

Structural properties of $CoWO_4$ nanomaterials have been explored by few authors. Flower-like $CoWO_4$ nanostructured prepared by alcohol mediated thermal synthesis reported by Ting you et al [87]. Low cost and high-quality cobalt tungstate nanorods have been synthesised by the facile hydrothermal method [53]. Hydrothermal synthesis of $CoWO_4$ nanomaterials characterized by X-ray emission spectroscopy (XES) and X-ray absorption spectroscopy (XAS) to find out the electronic properties [88].

Recently $CoWO_4$ nanomaterials have been used in capacitor applications. High supercapacitive performance of cobalt tungstate nanoparticles prepared by co-precipitation method [89]. Nitrogen-doped reduced graphene oxide (rGO) with $CoWO_4$ (NrGO/$CoWO_4$) nanocomposites shows high capacitance, good rates and cycling performance[90]. Facile synthesis of reduced graphene oxide/$CoWO_4$nanocomposites serves as an electrode in supercapacitors[91]. $CoWO_4$@$NiWO_4$ nanocomposite combines the high capacity of $NiWO_4$ and the excellent stability of $CoWO_4$ and shows the Faradaic redox properties with a higher capacity and better stability than single materials [92]. The high rate capability of mesoporous $NiWO_4$–$CoWO_4$ nanocomposite was used as a positive material in hybrid supercapacitor [93]. High-quality $WO_3/CoWO_4$ core-shell p-n junction nanowires have been prepared by hydrothermal route [94]. Different catalytic behaviours of the amorphous and crystalline $CoWO_4$ for electrochemical water oxidation reported [95]. Conversion efficiency and fill factor of the $CoWO_4$ thin film used as an electrolyte for the photovoltaic cell [96]. $CoWO_4$ nanospheres were used in nonenzymatic glucose sensor due to its ultra-high sensitivity, wide linear range with lower detection limit, long-term stability and reproducibility properties[97].

1.15. Motivation, scope and objective of the present work

1.15.1. Motivation

Enhancing the PL emission intensity of phosphors along with multifunctional properties are great challenges for the researchers. Tungstate nanomaterials are important inorganic materials for their vast applications in many technological fields. Because of easy charge separation behaviour in tungstate materials, it is used in photocatalytic and photoluminescent applications frequently. From the brief review on wolframite type monoclinic $CoWO_4$, we came to know that there is no report on the nanocomposites of $CoWO_4$ with scheelite type tungstates. The inspiration of the research problem came from the reported research papers entitled "Optical absorption and photoluminescent studies of cerium-doped cobalt tungstate nanomaterials" by S.J.Naik et al [48]. In this report the secondary phase of Ce_2WO_6 was responsible for the enhanced emission and also the giant emission of ZnO/TiO_2nanocomposites reported by H.Y. Lin et al shortly explained about electron and hole transfer from one phase to another phase due to type I band alignment in the nanocomposites [98]. So it was decided to synthesize and characterize the $CoWO_4/PbWO_4$ nanocomposites.

Interfaces play an important role in oxide hetero-structure nanocomposites. Interfacial effects in oxide heterostructure thin film have been studied widely [42]. Even though heterostructures powder nanocomposites are still in their infancy, they have already demonstrated great potential owing to their enhanced ionic conductivity [99]. The creation of surface charge layer (SCL) at the interface is the reason for enhancing the electrical properties in nanocomposites samples. So it was decided to study the electrical properties $CoWO_4$ and $CoWO_4/PbWO_4$ nanocomposites.

The interface plays a crucial role in enhancing the magnetic properties of many important magnetic materials by regulating magnetic exchange coupling. The spirit of the magnetic properties study originated from the paper entitled "Interfacial magnetism and exchange coupling in $BiFeO_3$–CuO nanocomposites" by Kaushik Chakrabarti et al.[100]. The large exchange bias effect and multiferroicity in $BiFeO_3$ and CuO make the nanocomposite more attractive for multifunctional devices. So we wanted to study interface effect on magnetic properties of $CoWO_4/PbWO_4$ nanocomposites.

Higher thermal conductivity is one of the major disadvantages in thermoelectric materials. There is a big challenge to improve the efficiency of energy conversion which can be characterized by the figure of merit (*ZT*). In the past two decades it is seen that nanomaterials showed enhanced ZT [101]. Interfacial energy barrier scattering leads to increase in Seebeck coefficient and reduce the thermal conductivity in PbTe based nanocomposites[102]. So there was interest in studying thermoelectric properties of $CoWO_4/PbWO_4$ nanocomposites.

At present many researchers are developing various novel electro-active materials with low cost, high electrochemical properties and environmental safety. Transition metal oxides and other composites have been widely applied in electrode materials of pseudo capacitors due to their diverse oxidation states, good conductivity and high capacitance. In addition, transition metal tungstate composites not only have been used for luminescent materials, pigments, catalyst and sensors, but also have been applied in electrochemistry for storage devices. Recently, more researchers are devoted to study the electrochemical performances of metal tungstate compounds such as 3D nanoporous $ZnWO_4$[103], $NiCo_2O_4$@$NiWO_4$[104], $CoWO_4$ [15], $FeWO_4$ [16] , RGO/$CoWO_4$ [17], $NiWO_4$/reduced graphene oxide[105], Co_3O_4@$CoWO_4$/rGO [101] and so on. Metal tungstates composites are promising candidates of electro-active materials and hence we opted to study the electrochemical properties of $CoWO_4/PbWO_4$ nanocomposites.

1.15.2. Scope of the present work

Metal tungstates are an important class of self-activated luminescent materials and some also act as a host for rare earth elements for luminescence applications [17–20]. They crystallize into two structures based on their cationic radii, i.e., scheelite ($r > 0.90$ Å) and wolframite ($r < 0.77$ Å) [21,22]. The intrinsic luminescence of scheelite and wolframite arise due to annihilation of the self-trapped exciton (STE), which forms excited $[WO_4]^{2-}$ or $[WO_6]^{6-}$ complexes respectively. These materials have found applications in scintillation counters, lasers and optical fibers. Some of the divalent transition metal tungstates have also gained commercial interest in lasers and fluorescent lamps, while some are of special importance due to their electrical conductivity and magnetic properties. In addition, these materials also find applications as catalysts and humidity sensors[106] .

Among the transition metal tungstates, $CoWO_4$ plays an important role in applications and can be produced at low cost. It is used in photoluminescence, photocatalytic, electrochemical switching devices and super capacitive materials[48,49,64,107]. The optical properties of $CoWO_4$ nanomaterials have been studied and listed in the literature survey. However not much work has been reported for luminescence studies of $CoWO_4$ bulk and nanomaterials. The PL intensity of $CoWO_4$ nanomaterial is reported to be 40 times higher than that of $CoWO_4$ bulk material [48]. Magnetic properties of $CoWO_4$ have been extensively studied due to its magnetic structure and phase transition. $CoWO_4$ is a wolframite structured compound which exhibits antiferromagnetic properties below the Neel temperature T_N=55 K and paramagnetic properties above T_N. The reduction in T_N of $CoWO_4$ is also reported for nanomaterials due to reduced exchange coupling from the nanoparticles [108].

Nanocomposites are materials with a nanoscale structure that improve the macroscopic properties of products. The ceramic nanocomposites reported until now are either a ceramic nanophase in a ceramic matrix, a carbonaceous nanophase in a ceramic matrix or a ceramic nanophase in a polymer matrix. Experimental work has generally shown that virtually all types and classes of nanocomposite materials lead to new and improved properties, when compared to their macrocomposite counterparts [4]. Therefore, nanocomposites promise new applications in many fields such as mechanically-reinforced lightweight components, non-linear optics, battery cathodes and ionics, nanowires, sensors and other systems[109]. Heterostructured composites have been widely used in the industry and research field such as semiconductor lasers, Highly-efficient LEDs (heterostructure light-emitting diodes), low-noise high-electron-mobility transistors (HEMTs), high-frequency devices, solar cells, photodetectors, Bipolar wide-gap transistors, High-power diodes and thyristors and Infrared to visible converters[110].

The drawbacks in inorganic nanostructured materials can be overcome by fabricating nanocomposites with an interface [5]. The interfacing with nanocomposites can provide high-performance novel materials that find applications in photoluminescent, photocatalytic, photovoltaic, electrochemical and thermoelectric related fields. In nanocomposites accumulation of electrons and hole in one of the phases due to charge transfer increases the number of recombination in that phase. This process enhances the PL intensity of that phase.

The formation of space charge layer (SCL) at interface enhances the dielectric constant and conductivity (AC and DC) of the nanocomposites. As in the case of thermoelectric materials the interfacial energy barrier carrier scattering is an effective method to improve the thermoelectric performance.

Samples were prepared by the co-precitation method without using surfactants. Co-precipitation reactions involve simultaneous occurrence of nucleation, growth, coarsening, and/or agglomeration processes. The advantages of the co-precipitation method are high yield, high product purity, the lack of necessity to use organic solvents, easily reproducible, and low cost [111,112]. Generally a surfactant in the co-precipitation method is used to disperse the nanoparticles. But in our work the non utilization of surfactant and sintering of samples resulted in agglomeration of nanoparticles. Agglomeration was found to support interfacing thus enhancing optical, electrical and thermoelectric properties of $CoWO_4/PbWO_4$nanocomposites. Also the absence of surfactants avoids the possible risk of contamination of the samples [113].

In this thesis we report the enhanced optical, electrical and thermoelectric properties of $CoWO_4/PbWO_4$ nanocomposites. $CoWO_4$ and $PbWO_4$ align in Type I band position. Intrinsic bluish-green emission of $CoWO_4$ nanomaterials is enhanced four times in $CoWO_4/PbWO_4$ nanocomposite (Pb/Co = 0.028) due to the possible excitonic charge transfer from the $PbWO_4$ phase to the $CoWO_4$ phase. Presence of a very small amount of $PbWO_4$ phase in the $CoWO_4/PbWO_4$ nanocomposite has been quite effective in enhancing the intrinsic luminescence of the $CoWO_4$ phase. The dielectric constant of the present nanocomposite is 17 times higher than that of $CoWO_4$ due to the Maxwell – Wagner polarization. Relaxor like behavior is observed in both $CoWO_4$ and the $CoWO_4/PbWO_4$ nanocomposites. This effect is due to the $CoWO_4$ phase of the samples.Enhanced AC and DC conductivity were observed for the nanocomposites as compared to the bare $CoWO_4$ due to the SCL formation at the interface. Maximum Seebeck coefficient and power factor were observed for the same $CoWO_4/PbWO_4$ nanocomposite which might be due to the interfacial energy barrier scattering at the interface. $CoWO_4$ nano sample shows good electrochemical activity with high specific capacity of 700 F/g making it a promising electrode for pseudo capacitor applications. Presence of the $PbWO_4$ phase in $CoWO_4$ does not alterer the magnetic properties

of $CoWO_4$ except for a small reduction in magnetization and Neel temperature $T_N$due to the small exchange coupling between the Pb^{2+} and Co^{2+} ions. $CoWO_4/PbWO_4$ nanocomposite (Pb/Co = 0.028) could be considered as a multifunctional material due to its enhanced optical, electrical and thermoelectric properties.

1.15.3. Objectives of the present work

1. Synthesis of $CoWO_4$ and $CoWO_4/PbWO_4$ nanocomposites at room temperature using co-precipitation method without using any surfactant, optimizing the Pb/Co atomic ratio and sintering the sample at 600^0C to get the possible interface.
2. Room temperature XRD characterization to find the phase purity, crystallite size, lattice strain and lattice constant.
3. SEM, TEM, EDAX, Zeta potential, FTIR and XPS measurements at room temperature to check the surface morphology, particle size, elemental composition, agglomeration, stretching vibrations and elemental oxidation states respectively of the prepared samples.
4. UV-Vis reflectance spectra to calculate the band gap and band positions of $CoWO_4$ and $PbWO_4$ phases to check the band alignment between the two phases.
5. Recording of PL emission spectra and PL lifetime measurements at room temperature to check the effect of $PbWO_4$ phase on the PL emission and PL lifetime of $CoWO_4$ phase.
6. AC electrical measurements in the frequency range of 20Hz to 3MHz at the temperature range of 30^0C to 350^0C and DC electrical measurements in the temperature range of 350K to 770K to study the role of defects in the $CoWO_4/PbWO_4$ interface on the dielectric constant, AC conductivity and DC conductivity respectively.
7. Ferroelectric P-E hysteresis study at room temperature and at various temperatures (50^0C, 170^0C, 200^0C) to confirm the ferroelectric nature of the prepared samples.
8. Magnetic measurements such as field dependent magnetization in the range of -30 kOe to +30 kOe at room temperature and temperature dependent magnetization in the range of 5K to 400K at constant field to check the effect of interface on the magnetic properties.

9. Thermoelectric study in the temperature range of 400K to 750K to study the interfacial energy barrier scattering effect on the Seebeck coefficient and power factor of the $CoWO_4/PbWO_4$ samples.
10. Room temperature electrochemical studies such as cyclic voltammetry (CV), galvanostatic charge discharge (GCD) and electrochemical impedance spectra to find specific capacity and the corresponding equivalent circuit of the samples.

1.16. Organization of chapters in the thesis

- **Chapter 2**: Lists the various instruments used to characterize the $CoWO_4$ and $CoWO_4/PbWO_4$ nanocomposites.

- **Chapter 3**: Explains the Co-precipitation synthesis of $CoWO_4/PbWO_4$ nanocomposites and initial characterization of the prepared nanocomposites.

- **Chapter 4:** Showcases the optical study and mechanism behind the enhanced PL intensity of $CoWO_4/PbWO_4$ nanocomposites.

- **Chapter 5:** Covers the electrical, magnetic, electrochemical and thermoelectric properties of $CoWO_4/PbWO_4$ nanocomposites.

- **Chapter 6**: Summary of the results, overall conclusions and future scope within the area of research are presented.

References

1. Pedro Henrique Cury Camargo, Kestur Gundappa Satyanarayana, and Fernando Wypych, Mater. Res. **12**, 1 (2009).

2. R. Bogue, Assem. Autom. **31**, 106 (2011).

3. J. Njuguna, F. Ansari, S. Sachse, H. Zhu, and V. M. Rodriguez, in *Heal. Environ. Saf. Nanomater. Polym. Nancomposites Other Mater. Contain. Nanoparticles* (Woodhead Publishing Limited, UK, 2014), pp. 3–27.

4. M. Zamkov and C. S. S. R. Kumar, *UV-VIS and Photoluminescence Spectroscopy for Nanomaterials Characterization* (Springer Heidelberg New York Dordrecht London, 2013).

5. Koichi Niihara, Ceram. Soc. Japan **99**, 945 (1991).

6. L. Wei, C. Shifu, Z. Huaye, and Y. Xiaoling, J. Exp. Nanosci. **6**, 102 (2011).

7. F. Ansari, A. Sobhani, and M. Salavati-Niasari, J. Colloid Interface Sci. **514**, 723 (2018).

8. A. Hamrouni, N. Moussa, A. Di Paola, L. Palmisano, A. Houas, and F. Parrino, J. Photochem. Photobiol. A Chem. **309**, 47 (2015).

9. A. Kitai, *Luminescent Materials and Applications* (John Wiley & Sons Ltd, West Sussex, England, 2008).

10. C. Ronda, *Luminescence From Theory to Applications* (WILEY-VCH Verlag GmbH & Co., Weinheim, 2008).

11. G. Blasse and B. C. Grabmaier, *Luminescent Materials* (Springer.VerJag Berlin Heidelberg, VerJag Berlin Heidelberg 1994, 1994).

12. J. R. Lakowicz, *Principles of Fluorescence Spectroscopy*, Third Edit (New York, 2006).

13. R. Liu, *Phosphors , Up Conversion Nano Particles , Quantum Dots and Their Applications* (Springer Science+Business, Singapore, 2016).

14. V. N. Shevchuk and I. V. Kayun, Radiat. Meas. **42**, 847 (2007).

15. M. Guzik, E. Tomaszewicz, Y. Guyot, J. Legendziewicz, and G. Boulon, J. Mater. Chem. **22**, 14896 (2012).

16. A. A. Annenkov, M. V. Korzhik, and P. Lecoq, Nucl. Instruments Methods Phys. Res. Sect. A Accel. Spectrometers, Detect. Assoc. Equip. **490**, 30 (2002).

17. I. M. Pinatti, I. C. Nogueira, W. S. Pereira, P. F. S. Pereira, R. F. Gonçalves, J. A. Varela, E. Longo, and I. L. V. Rosa, Dalt. Trans. **44**, 17673 (2015).

18. J. Liao, B. Qiu, H. Wen, and W. You, Opt. Mater. (Amst). **31**, 1513 (2009).

19. L. Lv, J. Wang, W. Wang, and L. Han, J. Alloys Compd. **635**, 25 (2015).

20. K. G. Sharma and N. R. Singh, J. Rare Earths **30**, 310 (2012).

21. S. J. NAIK, CATALYTIC AND SOLID STATE STUDIES OF METAL TUNGSTATES AND MOLYBDATES, Goa University, 2010.

22. J. Macavei and H. Schulz, Zeitschrift Fiir Krist. **207**, 193 (1993).

23. M. Nikl, P. Bohacek, E. Mihokova, M. Kobayashi, M. Ishii, Y. Usuki, V. Babin, A. Stolovich, S. Zazubovich, and M. Bacci, J. Lumin. **87**, 1136 (2000).

24. A. Kalinko and V. Pankratov, Cent. Eur. J. Phys. **9**, 432 (2014).

25. S. Ye, F. Xiao, Y. X. Pan, Y. Y. Ma, and Q. Y. Zhang, Mater. Sci. Eng. R Reports **71**, 1 (2010).

26. M. A. Rauf and S. S. Ashraf, Chem. Eng. J. **151**, 10 (2009).

27. L. H. Hoang, P. Van Hanh, N. D. Phu, X. B. Chen, and W. C. Chou, J. Phys. Chem. Solids **77**, 122 (2015).

28. G. Bai, M. K. Tsang, and J. Hao, Adv. Funct. Mater. **26**, 6330 (2016).

29. K. W. Böer and U. W. Pohl, *Exciton. In: Semiconductor Physics* (Springer, Switzerland, 2015).

30. C. Zhang, D. Guo, C. Hu, Y. Chen, H. Liu, H. Zhang, and X. Wang, Phys. Rev. B **84**, 035416 (2013).

31. V. B. Mikhailik, H. Kraus, G. Miller, M. S. Mykhaylyk, and D. Wahl, J. Appl. Phys. **97**, 083523 (2005).

32. V. V. Laguta, M. Nikl, and S. Zazubovich, Radiat. Meas. **42**, 515 (2007).

33. E. Sreeja, S. Gopi, V. Vidyadharan, P. Remya Mohan, C. Joseph, N. V. Unnikrishnan, and P. R. Biju, Powder Technol. **323**, 445 (2018).

34. G. Blasse, Philips Res. Repts **25**, 231 (1970).

35. Toshihiro Yamase and M. Sugeta, J. CHEM. Soc. Dalt. TRANS **20**, 759 (1993).

36. S. Dey, R. A. Ricciardo, H. L. Cuthbert, and P. M. Woodward, Inorg. Chem. **53**, 4394 (2014).

37. S. M. M. Zawawi, R. Yahya, A. Hassan, H. N. M. E. Mahmud, and M. N. Daud, Chem. Cent. J. **7**, 1 (2013).

38. J. K. Nelson and Y. Hu, J. Phys. D. Appl. Phys. **38**, 213 (2005).

39. S. DEVI and A. K. JHA, Bull. Mater. Sci. **33**, 683 (1993).

40. C. E. Ciomaga, A. M. Neagu, M. V. Pop, M. Airimioaei, S. Tascu, G. Schileo, C. Galassi, and L. Mitoseriu, J. Appl. Phys. **113**, 0 (2013).

41. G. Catalan, D. O'Neill, R. M. Bowman, and J. M. Gregg, Appl. Phys. Lett. **77**, 3078 (2000).

42. E. Fabbri, D. Pergolesi, and E. Traversa, Sci. Technol. Adv. Mater. **11**, 054503 (9pp) (2010).

43. M. Ivanov, J. Macutkevic, R. Grigalaitis, and J. Banys, in *Magn. Ferroelectr. Multiferroic Met. Oxides* (2018), pp. 5–33.

44. Z.-G. Ye, *Handbook of Dielectric, Piezoelectric and Ferroelectric Materials Synthesis,*

Properties and Applications (Woodhead Publishing and Maney Publishing, Cambridge England, n.d.).

45. I. Rivera, A. Kumar, N. Ortega, R. S. Katiyar, and S. Lushnikov, Solid State Commun. **149**, 172 (2009).

46. S. M. Gupta and A. R. Kulkarni, Mater. Chem. Phys. **39**, 98 (1994).

47. P. A. Kröger, Nature **159**, 674 (1947).

48. S. J. Naik, U. Subramanian, R. B. Tangsali, and A. V Salker, J. Phys. D. Appl. Phys. **44**, 115404 (2011).

49. U. Subramanian, S. J. Naik, R. B. Tangsali, and A. V Salker, J. Lumin. **134**, 464 (2013).

50. S. J. Naik and A. V. Salker, Solid State Sci. **12**, 2065 (2010).

51. X. C. Song, E. Yang, R. Ma, H. F. Chen, and Y. Zhao, J. Nanoparticle Res. **10**, 709 (2008).

52. J. Juliet Josephine Joy and N. Victor Jaya, J. Mater. Sci. Mater. Electron. **24**, 1788 (2013).

53. L. Zhen, W. S. Wang, C. Y. Xu, W. Z. Shao, and L. C. Qin, Mater. Lett. **62**, 1740 (2008).

54. J. Juliet Josephine Joy, Int. J. Chem. Concepts **01**, 44 (2015).

55. C. Stella, N. Soundararajan, and K. Ramachandran, 050153 (2015).

56. S. Thongtem, S. Wannapop, and T. Thongtem, Ceram. Int. **35**, 2087 (2009).

57. A. Azadbakht, A. R. Abbasi, N. Noori, E. Rafiee, and M. Taran, Fibers Polym. **14**, 687 (2013).

58. Z. Song, J. Ma, H. Sun, Y. Sun, J. Fang, Z. Liu, C. Gao, Y. Liu, and J. Zhao, Mater. Sci. Eng. B Solid-State Mater. Adv. Technol. **163**, 62 (2009).

59. M. Jeyakanthan, U. Subramanian, and R. B. Tangsali, J. Mater. Sci. Mater. Electron. **29**, (2018).

60. Xu Yan, Z. Wu, C. Huang, K. Liu, and W. Shi, Ceram. Int. **43**, 5388 (2017).

61. H. Cui, B. Li, Y. Zhang, X. Zheng, X. Li, Z. Li, and S. Xu, Int. J. Hydrogen Energy **43**, 18242 (2018).

62. X. A. López, A. F. Fuentes, M. M. Zaragoza, J. A. Díaz Guillén, J. S. Gutiérrez, A. L. Ortiz, and V. Collins-Martínez, Int. J. Hydrogen Energy **41**, 23312 (2016).

63. T. Montini, V. Gombac, A. Hameed, L. Felisari, G. Adami, and P. Fornasiero, Chem. Phys. Lett. **498**, 113 (2010).

64. U. M. García-Pérez, A. Martínez-De La Cruz, and J. Peral, Electrochim. Acta **81**, 227 (2012).

65. K. Jothivenkatachalam, S. Prabhu, A. Nithya, S. Chandra Mohan, and K. Jeganathan, Desalin. Water Treat. **54**, 3134 (2015).

66. V. K. V. P. Srirapu, A. Kumar, N. Kumari, and R. N. Singh, Indian J. Chem. - Sect. A Inorganic, Phys. Theor. Anal. Chem. **57A**, 1100 (2018).

67. M. Shekofteh-Gohari and A. Habibi-Yangjeh, Ceram. Int. **43**, 3063 (2017).

68. V. K. V. P. Srirapu, A. Kumar, P. Srivastava, R. N. Singh, and A. S. K. Sinha, Electrochim. Acta **209**, 75 (2016).

69. S. Feizpoor and A. Habibi-Yangjeh, J. Colloid Interface Sci. **524**, 325 (2018).

70. P. Taneja, S. Sharma, A. Umar, S. K. Mehta, A. O. Ibhadon, and S. K. Kansal, Mater. Chem. Phys. **211**, 335 (2018).

71. B. Maddah, F. Jookar-Kashi, and M. Akbari, J. Mater. Sci. Mater. Electron. **29**, 13723 (2018).

72. C. Ling, L. Q. Zhou, and H. Jia, RSC Adv. **4**, 24692 (2014).

73. R. Bharati, R. A. Singh, and B. M. Wanklyn, J. Mater. Sci. **16**, 775 (1981).

74. R. B. Yadav, J. Phys. Chem. Solids **44**, 697 (1983).

75. K. Hoang, M. Oh, and Y. Choi, RSC Adv. **8**, 4191 (2018).

76. S. Sagadevan, J. Podder, and I. Das, J. Mater. Sci. Mater. Electron. **27**, 9885 (2016).

77. R. C. Pullar, S. Farrah, and N. M. N. Alford, J. Eur. Ceram. Soc. **27**, 1059 (2007).

78. Z. Kukua, E. Tomaszewicz, S. Mazur, T. Gro, H. Duda, S. Pawlus, S. M. Kaczmarek, H. Fuks, and T. Mydlarz, Philos. Mag. **92**, 4167 (2012).

79. B. Zhang and L. Li, J. Mater. Sci. Mater. Electron. **28**, 3523 (2017).

80. S. Shanmugapriya, S. Surendran, V. D. Nithya, P. Saravanan, and R. Kalai Selvan, Mater. Sci. Eng. B **214**, 57 (2016).

81. V. M. Gredescul, S. A. Gredescul, V. V Eremenko, and V. M. Naumenko, J. Phys. Chem. Solids **33**, 859 (1972).

82. C. P. Landee and E. F. Westrum, J. Chem. Thermodyn. **8**, 471 (1976).

83. J. B. Forsyth and C. Wilkinson, J. Phys. Condens. Matter **6**, 3073 (1994).

84. J. Deng, L. Chang, P. Wang, E. Zhang, J. Ma, and T. Wang, Cryst. Res. Technol. **47**, 1004 (2012).

85. F. Ahmadi, M. Rahimi-Nasrabadi, A. Fosooni, and M. Daneshmand, J. Mater. Sci. Mater. Electron. **27**, 9514 (2016).

86. N. Hollmann, Z. Hu, T. Willers, L. Bohatý, P. Becker, A. Tanaka, H. H. Hsieh, H. J. Lin, C. T. Chen, and L. H. Tjeng, Phys. Rev. B - Condens. Matter Mater. Phys. **82**, 1 (2010).

87. T. You, G. Cao, X. Song, C. Fan, W. Zhao, Z. Yin, and S. Sun, Mater. Lett. **62**, 1169 (2008).

88. S. Rajagopal, V. L. Bekenev, D. Nataraj, D. Mangalaraj, and O. Y. Khyzhun, J. Alloys Compd. **496**, 61 (2010).

89. K. Adib, M. Rahimi-Nasrabadi, Z. Rezvani, S. M. Pourmortazavi, F. Ahmadi, H. R. Naderi, and M. R. Ganjali, J. Mater. Sci. Mater. Electron. **27**, 4541 (2016).

90. N. Kumari and R. N. Singh, AIMS Mater. Sci. **3**, 1456 (2016).

91. X. Xu, J. Shen, N. Li, and M. Ye, Electrochim. Acta **150**, 23 (2014).

92. X. Xu, J. Gao, G. Huang, H. Qiu, Z. Wang, J. Wu, Z. Pan, and F. Xing, Electrochim. Acta **174**, 837 (2015).

93. Y. Wang, C. Shen, L. Niu, Z. Sun, F. Ruan, M. Xu, S. Shan, C. Li, X. Liu, and Y. Gong, Mater. Chem. Phys. **182**, 394 (2016).

94. B. Sun, H. Li, L. Wei, and P. Chen, CrystEngComm **16**, 9891 (2014).

95. H. Jia, J. Stark, L. Q. Zhou, C. Ling, T. Sekito, and Z. Markin, RSC Adv. **2**, 10874 (2012).

96. P. K. Pandey, N. S. Bhave, and R. B. Kharat, J. Mater. Sci. **42**, 7927 (2007).

97. M. Sivakumar, R. Madhu, S. M. Chen, V. Veeramani, A. Manikandan, W. H. Hung, N. Miyamoto, and Y. L. Chueh, J. Phys. Chem. C **120**, 17024 (2016).

98. H. Y. Lin, Y. Y. Chou, C. L. Cheng, and Y. F. Chen, **15**, 13832 (2007).

99. S. Takai, K. Sugiura, and T. Esaka, Mater. Res. Bull. **34**, 193 (1999).

100. K. Chakrabarti, B. Sarkar, V. D. Ashok, K. Das, S. S. Chaudhuri, and S. K. De, Nanotechnology **24**, (2013).

101. E. M. M. Ibrahim, A. M. Abu-Dief, A. Elshafaie, and A. M. Ahmed, Mater. Chem. Phys. **192**, 41 (2017).

102. J. Martin, L. Wang, L. Chen, and G. S. Nolas, Phys. Rev. B **79**, 1 (2009).

103. T. N. Nikolaenko, Y. A. Hizhnyi, and S. G. Nedilko, J. Lumin. **128**, 807 (2008).

104. X. Du, Q. Shao, and X. Zhang, Int. J. Hydrogen Energy **44**, 2883 (2019).

105. N. Poudel, B. Lorenz, B. Lv, Y. Q. Wang, F. Ye, J. Wang, J. A. Fernandez-Baca, and C. W. Chu, Integr. Ferroelectr. **166**, 17 (2015).

106. L. Zhang, C. Lu, Y. Wang, and Y. Cheng, Mater. Chem. Phys. **103**, 433 (2007).

107. X. Xing, Y. Gui, G. Zhang, and C. Song, Electrochim. Acta **157**, 15 (2015).

108. L. Meddar, M. Josse, M. Maglione, A. Guiet, C. La, P. Deniard, R. Decourt, C. Lee, C. Tian, S. Jobic, M. H. Whangbo, and C. Payen, Chem. Mater. **24**, 353 (2012).

109. B. G. Rao, D. Mukherjee, and B. M. Reddy, in *Nanostructures Nov. Ther. Synth. Charact. Appl.* (2017), pp. 1–36.

110. N. Pryds and V. Esposito, J. Electroceramics **38**, 1 (2017).

111. N. Sivakumar, A. Narayanasamy, K. Shinoda, C. N. Chinnasamy, B. Jeyadevan, and J. M. Greneche, J. Appl. Phys. **102**, (2007).

112. L. S. Cavalcante, J. C. Sczancoski, L. F. Lima, J. W. M. Espinosa, P. S. Pizani, J. A. Varela, and E. Longo, Cryst. Growth Des. **9**, 1002 (2009).

113. A. V. Rane, K. Kanny, V. K. Abitha, and S. Thomas, *Methods for Synthesis of Nanoparticles and Fabrication of Nanocomposites* (Elsevier Ltd., 2018).

CHAPTER 2

INSTRUMENTATION TECHNIQUES

2.1. Introduction

Instrumentation techniques have been discussed in this chapter which includes X-ray diffraction(XRD) techniques, scanning electron microscopy (SEM), transmission electron microscope (TEM), Fourier transform Infra-red spectrometer (FTIR), energy dispersive analysis using X-rays (EDS), Zeta potential instrument, X-ray photoelectron spectroscopy (XPS), Spectroflourometer, UV-Vis diffuse reflectance spectrophotometer, Vibrating sample magnetometer (VSM), Dielectric spectroscopy, DC conductivity set up, thermoelectric set up and electrochemical analyzing set up.

2.2. XRD techniques

X-ray diffraction (XRD) is a nondestructive tool for structural characterization of materials. It provides information on structures, phases, preferred crystal orientations and other structural parameters such as average crystallite size, crystallinity, strain, and crystalline defects[1].

Photograph of the RIGAKU Ultima IV powder X-ray diffractometer is shown in Fig. 2.1(a). XRD patterns were recorded using RIGAKU Ultima IV powder X-ray diffractometer with Cu-Kα radiation (λ = 0.15418 nm). The measurement was recorded in the 2θ range of 20^o – 80^o with a step size of 0.02^o. X-ray source, a sample chamber and an X-ray detector are the three important components of X-ray diffractometer. Fig. 2.1(b) shows the schematic diagram of computer controlled X-ray powder diffractometer. X-rays from the source are collimated and directed towards the sample. Then, the intensities of diffracted X-rays are recorded using detector. The XRD patterns were identified with comparing the experimental 2θ values of the peak intensities to the Joint Commision Powder Diffraction (JCPDS) pattern files.

Fig. 2.1(a). RIGAKU Ultima IV powder X-ray diffractometer, NIO, Goa.

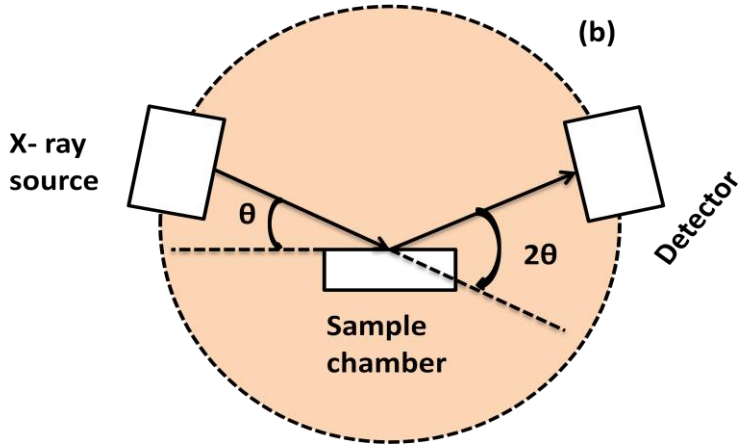

Fig. 2.1(b). Schematic diagram of X-ray diffractogram

2.3. Scanning electron microscope (SEM) and Energy dispersive X-ray spectroscopy (EDS)

SEM is a microscope that uses electrons to form an image instead of light which will be used in optical microscope. The SEM is used to determine the surface morphology of materials. The resolution of SEM is one order of magnitude less than and two orders of magnitude greater than the TEM and optical microscope respectively [2]. We have used

CARL ZEISS EVO 18 model for recording the SEM images of the samples. Surface of the samples were made conductive by gold coating. CARL ZEISS EVO 18 SEM modelis shown in Fig.2.2.

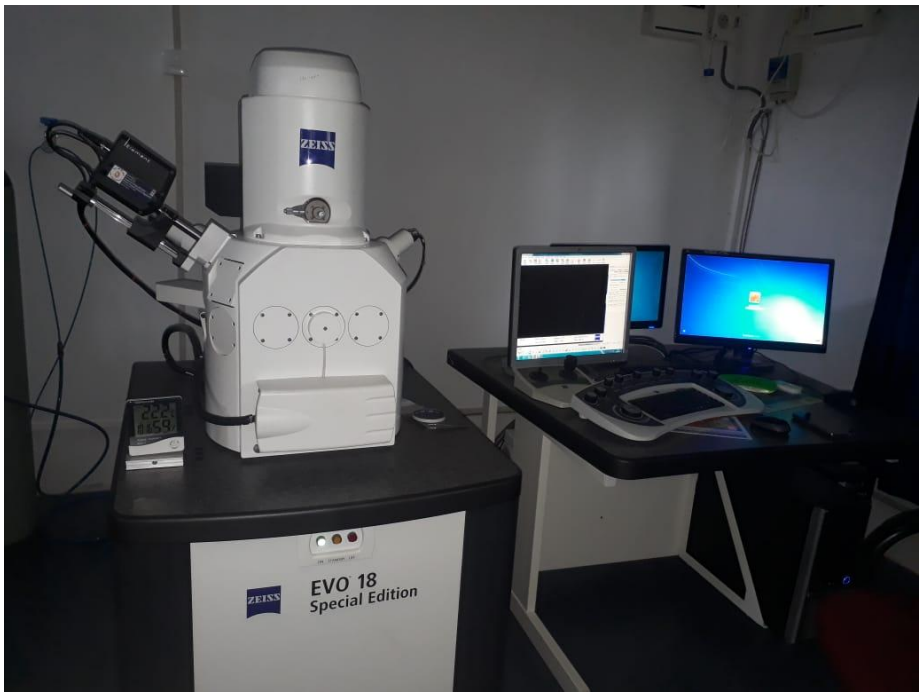

Fig. 2.2.CARLZEISS EVO 18 SEM, USIC, Goa University, Goa.

Specifications of CARL ZEISS EVO 18 SEM:

Filament: Tungsten

Secondary e- image resolution: 50 nm (depends on sample)

BSD detector: Available

Magnification: Upto 50X – 100kX (depends on sample)

EDS analysis was carried out for prepared samples to find the elemental composition present in the samples. It was carried out by JEOL-JSM 5800 LV scanning electron microscope instrument. It involves a beam of X-rays, incident onto the sample which may elevate an electron to an excited state. The arrival of the electron to the ground state results in characteristic x-ray emission. These x-rays are then detected and utilized to give useful information about the constituent elements present in the compound.

Specifications of JEOL-JSM 5800 LV:

Magnification range: 18 to 300kX

Number elements mapping at a time: 32 elements

2.4. Transmission electron microscopy (TEM):

In materials science, TEM plays an important part in determining the particle form, shape, size, defects, surface layers or impurities, dislocations, grain boundaries etc. allowing visuals at the atomic scale and offering high resolution. Beam of electrons strike the specimen and parts of it are transmitted depending upon the thickness and electron transparency of the specimen. This transmitted segment is focused into an image on a phosphor screen or charge coupled device (CCD) camera wherein the stroked image generates light to make it visible. When more electrons get transmitted through, the image carries lighter areas whereas the darker areas of the image signify those areas of the sample that fewer electrons are transmitted through. In the present study, TEM images were recorded using the instrument Hitachi H-600 TEM is shown in Fig.2.3.

Fig. 2.3. Hitachi H-600 TEM, Sree Chitra Tirunal Institute for Medical Sciences and Technology, Trivandrum.

2.5. Zeta potential measurement

Zeta potential is the electrostatic potential (charge repulsive or attractive) between the particles in liquids. It's an important parameter to identify the stability of the particles. When charged particles are dispersed in liquid, the negatively charged particles attract the positive ions from the liquid and conversely positive charged particles attract the negative ions from the liquid. The zeta potential measurements of the samples were done by using a Zetasizer Nano Malvern Instrument. Powder samples were dispersed in ethanol for analysis. Zeta potential data are collected in the phase-analysis light scattering (PALS) mode, in which a laser light illuminates the particles in an electric field, and the scattered light is compared with a reference laser light for phase difference. This technique analyzes the scattered light phase shift from particle movements. The phase shift then can be used to determine electrophoretic mobility. The Smoluchowski approximation is used to calculate the zeta potential (ζ) from the measured electrophoretic mobility (μ) of the samples by using equation

$$\mu=\varepsilon\zeta(1.5)/\eta \qquad (2.1)$$

where ε is the dielectric constant and η is the absolute viscosity of the medium. The Zetasizer Nano Malvern instrument is shown in Fig. 2.4.

Fig. 2.4. Zetasizer Nano Malvern instrument, Materials Research center, MNIT, Jaipur.

Specifications:

Measurement range: 3.8 nm – 100microns

Sensitivity: 10mg/ml

Minimum sample volume: 150μL

2.6. Fourier Transform Infra-Red (FTIR) Spectroscopy

Infrared spectroscopy gives information about the vibrational characteristics of chemical functional groups in a samples [3]. We have used Shimadzu FTIR 8900 spectrophotometer to record IR spectra of the samples. The wave number (IR) range is 5000 to 400 cm^{-1} and for far IR range 700 to 50 cm^{-1} with a resolution of 0.5 cm^{-1}. For FTIR measurements 1mg of sample was mixed with 100mg of KBr and pelletized with 3 ton pressure for 5 minutes. 100mg KBr pellets were made with the same conditions and was used as a reference sample. This ensured that the final spectra are due to the vibrational modes present in the sample under study. Shimadzu FTIR 8900 assembly is shown in Fig. 2.5.

Fig. 2.5. Shimadzu FTIR 8900 assembly, Department of Physics, Goa University

Specifications:

Model: Shimadzu FTIR 8900

Wavenumber range: $7800cm^{-1} – 350cm^{-1}$

Detector: High sensitivity pyroelectric detector

Accuracy : $0.125cm^{-1}$

Resolution: $0.5\ cm^{-1}$

S/N ratio: 20000: 1

2.7. X-Ray Photoelectron Spectroscopy (XPS)

XPS is the most powerful characterization technique for identifying the valence state of elements present in materials. It makes use of photoionization and energy-dispersive analysis of the emitted photoelectrons to study the composition and electronic state of the surface region of a sample. In XPS the photons are absorbed by atoms in a molecule or solid, leading to ionization and the emission of core (inner shell) electrons. The kinetic energies of the emitted photoelectrons E_K, is measured by electron spectrometer and since the emitted electrons' kinetic energies are known, the electron binding energy of each of the emitted electron can be determined by using an equation that is based on the conservation of energy:

$$E_B = h\nu - E_K - \Phi \qquad (2.2)$$

Where $E_B$is the binding energy (BE) of the electron which is the characteristic of the orbital of the ejected photoelectron, $h\nu$ is the energy of the X-ray photons being used, $E_K$is the kinetic energy of the electron as measured by the instrument and Φ is the work function dependent on both the spectrometer and the material. This equation is essentially a conservation of energy equation. X-ray photoelectron spectrum (XPS) of the sample was measured using Omicron ESCA system with Al–K alpha source. First, a full scan or survey scan is recorded over a wide binding range, allowing the identification of elements present. Then a high resolution spectrum for the required element is obtained in their respective binding energy range, enabling us to plot a graph of intensity versus binding energy (eV).

Specifications:

Energy range: 0 to 1600 eV

Temperature range: Room temperature (integrated sample stage)

40-600K (L He cooled sample stage)

2.8. Ultraviolet - Visible Diffuse Reflectance Spectroscopy

Diffuse reflectance Ultraviolet - visible spectroscopy (DRS-UV-Vis) is known to be a very sensitive and useful technique for the opaque samples. Diffuse reflectance for the samples were carried out using SHIMADZU 2401 PC UV-Vis spectrophotometer is shown in Fig. 2.6.

Fig. 2.6.SHIMADZU 2401 PC UV-Vis spectrophotometer, Department of Physics, Goa University.

Light gets reflected from the surface of the opaque samples as shown in Fig. 2.7. There are two types of reflections: specular reflection and diffuse reflection. If the incident light gets scattered in different directions it is called diffuse reflection whereas symmetrical reflection with respect to the normal line is called specular reflection.

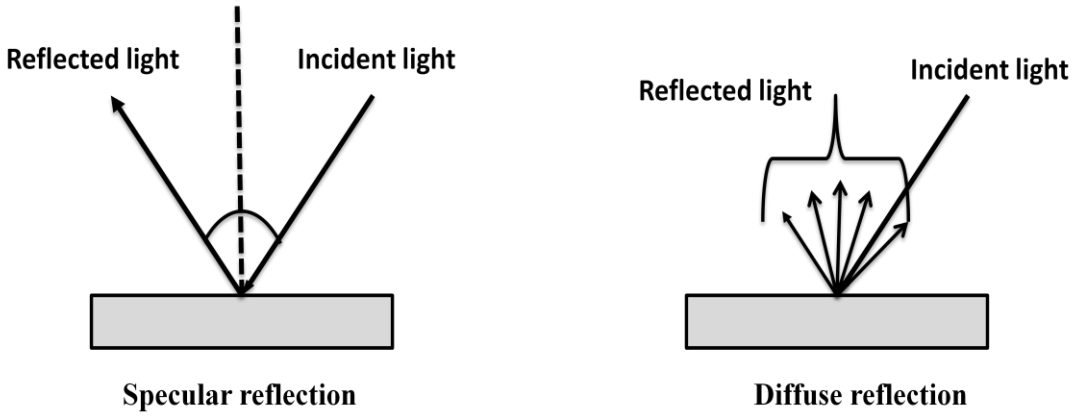

Fig. 2.7. Schematic diagram of specular and diffuse reflection.

Integrating sphere method is used to measure the diffuse reflectance spectra (DRS). The measurement is performed by placing the sample in front of the incident light window and the reflected light from the sample is concentrated on the detector using a sphere with $BaSO_4$ coated inside. Fig. 2.8 shows baseline compensation and sample measurement for DRS without including of specular reflection. The obtained reflectance light becomes relative reflectance with respect reference reflectance of the standard white board ($BaSO_4$). To avoid specular reflectance during the DRS measurements, the incident light is directed on the sample at an angle of 0^0. As a result only diffuse reflected light is measured.

The most popular continuum theory describing the diffuse reflectance effect is Kubelka - Munk (K-M) theory and is given by following equation

$$F(R) = \frac{(1-R)^2}{2R} \qquad (2.3)$$

The Kubelka-Munk function (K-M) was calculated from the diffuse reflectance spectra. The absorption coefficient(α) was calculated assuming a direct proportionality between K-M and α

$$\boldsymbol{F(R) = \frac{(1-R)^2}{2R} \propto \alpha}$$

where R is the diffuse reflectance (DR) of the sample and *F(R)* is K-M factor [4].

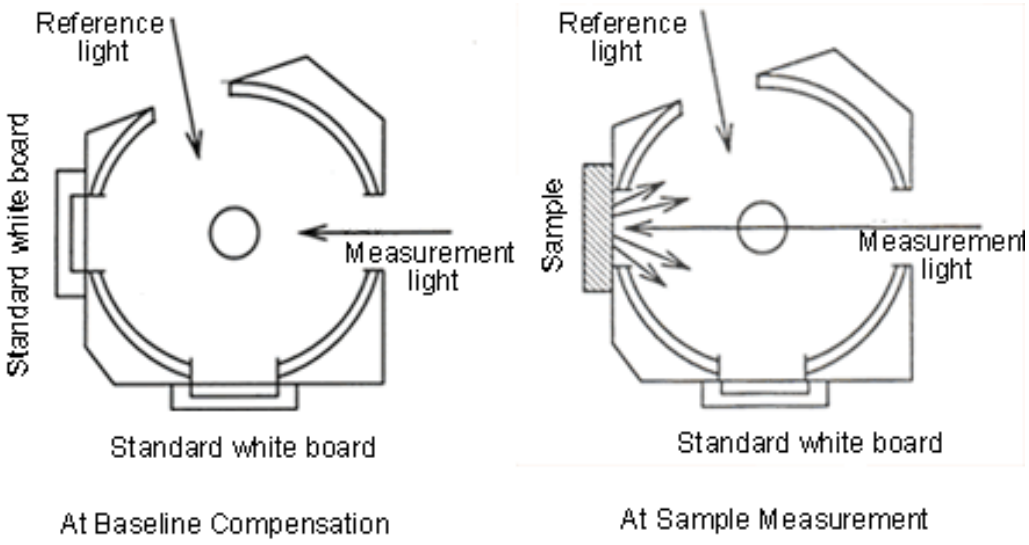

Fig. 2.8. Measurement of diffuse reflection not including specular reflection using an integrated sphere.

Specifications:

Model:	SHIMADZU UV-2401PC
Lamp:	50W halogen lamp, Deuterium (socket type)
Resolution:	0.1nm
Detectors:	Photomultiplier R-928
Wavelength Range:	190-800nm
Wavelength accuracy:	± 0.3 nm

2.9. PL Spectroscopy

Photoluminescence (PL) spectroscopy is a very useful nondestructive technique for studying the optical properties of the materials. PL emission spectra and PL life time decay curve of the samples were recorded using PTI QM-40 and QM-40Xe spectrofluorometer respectively controlled by FelixGX software. Cylindrical pellet of the samples were used to record the PL measurements. The emission spectra are measured by fixing the excitation wavelength and scanning the emissions. The instrumental set up for the PTI QM-40/40Xe spectrofluorometer is shown in Fig.2.9 and schematic diagram is shown in Fig. 2.10(a). The spectrum of Xenon arc lamb and Xenon pulsed lamp is shown in Fig. 2.10 (b) and 2. 10 (c).

Fig. 2.9. PTI QM-40/40Xe spectrofluorometer, Department of Physics, Goa University.

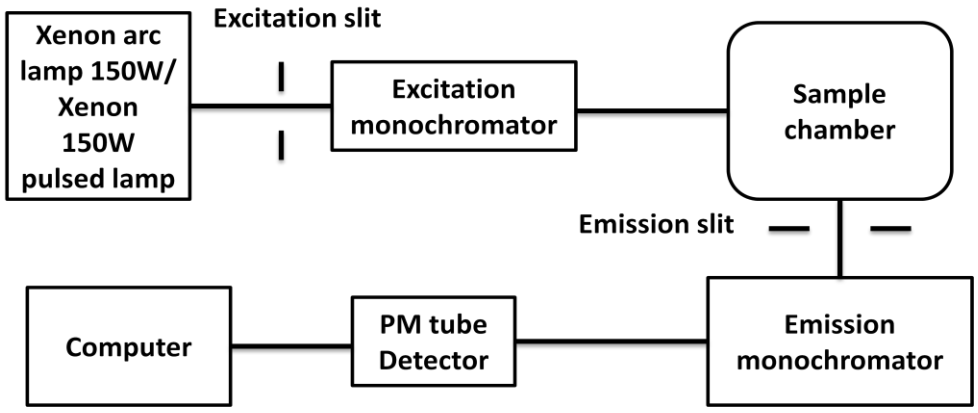

Fig. 2.10(a). Schematic diagram of PTI QM-40/40Xe spectrofluorometer.

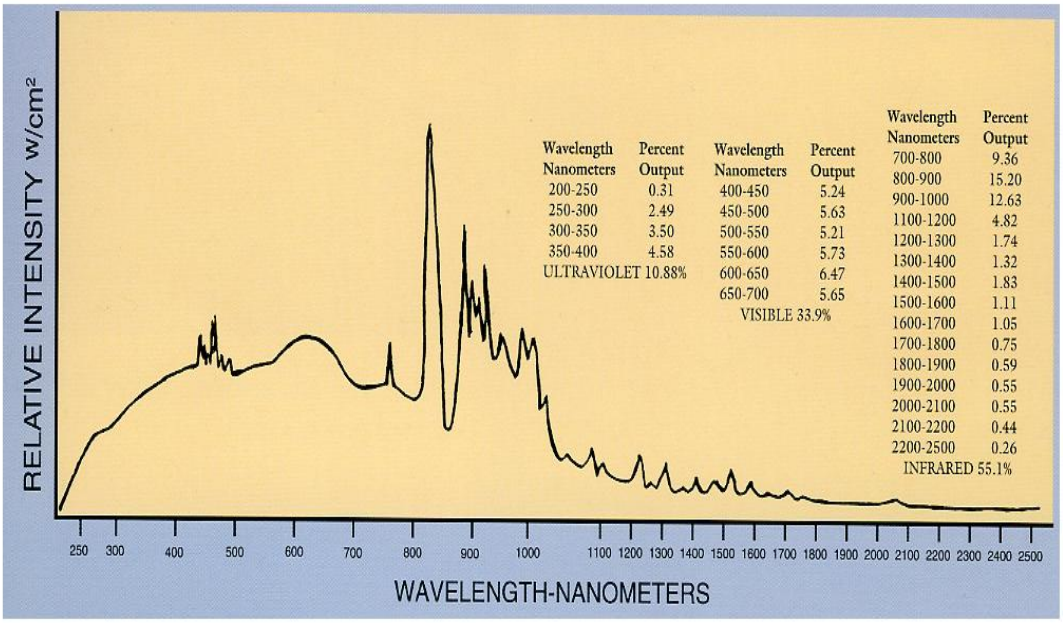

Fig. 2.10(b). Spectral distribution of Xenon arc lamp.

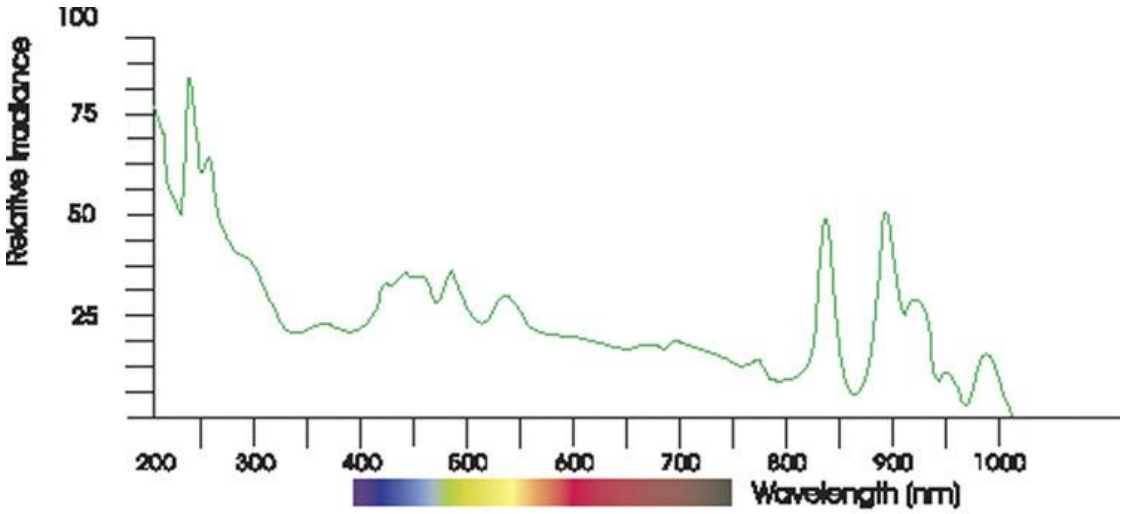

Fig. 2.10(c). Spectral distribution of Xenon pulsed lamp.

Specfications:

Model: PTI QM-40/40Xe spectrofluorometer

Lamp: 150W Xenon arc lamp, 150W Xenon pulsed lamp for lifetime Signal to

Noise Ratio: 10,000:1

Wavelength Accuracy: +/- 0.5 nm

Wavelength Resolution: 0.06 nm

Detection: Photon counting/analog

PMT type: R928

Lower limit for recording decay time: 1μS

2.10. Vibrating Sample Magnetometer (VSM)

VSM is widely used in magnetic materials research to study the magnetic properties. It operates based on the principle of Faraday's Law of electromagnetic induction, which states that a changing magnetic flux will produce an induced electric field. In VSM, the time rate of change of magnetic flux in the pick-up coil is produced by mechanically vibrating the magnetized sample and the induced field will be proportional to the magnetization of the sample.

The Quantum Design Versa Lab's 3Tesla Vibrating Sample Magnetometer (VSM) is a fast and sensitive DC magnetometer as shown in Fig.2.11. The basic measurement involves oscillation of sample in the vicinity of pickup coils and synchronous detection of induced voltage. With a compact gradiometer pickup coil configuration, comparatively large amplitudes of oscillation (1.3 mm peak) and 40 Hz frequency enables the system to resolve magnetization changes of the order 10-6 emu at a data acquisition rate of 1 Hz.

Fig. 2.11. Quantum Design's Versa Lab 3 Tesla Vibrating sample magnetometer (VSM), Department of Chemistry, Goa University.

The MultiVu software is equipped with advanced features incorporated in data acquisition, temperature and magnetic field control and is capable of sensing low levels of emu generated from extremely small quantity of material. The ambient temperature of the sample environment in instrumental set up could be lowered up to a minimum of 50K and can be raised up to 400 K. It is a cryogen free instrument uses cryo-cooler to achieve cryogenic temperatures.

2.11. Dielectric Spectroscopy

For the dielectric studies WAYNE KERR 6440B precision component analyzer has been used. It is one of the powerful impedance analyzers in the field of dielectric spectroscopy, and has great accuracy and sensitivity of the measured parameters. Samples were pressed into pallets of thickness ranging between 2.5mm to 1.5mm and the diameter of 6mm. The pellets were silver painted on both sides for establishing good ohmic contacts with the electrodes. Capacitance and dielectric loss were measured as a function of frequency over the range of 20Hz to 3MHz. Temperature dependence of capacitance and the dielectric loss was recorded over the temperature range of 300K to 773K at ten different frequencies (20Hz, 100Hz, 500Hz, 1kHz, 10kHz, 100kHz, 500kHz, 1MHz, 2MHz and 3MHz). Wayne Kerr precision component analyzer 6440B is shown in Fig. 2.12.

Fig. 2.12.WAYNE KERR 6440B Precision component analyzer, Department of Physics, Goa University, Goa.

2.12. DC conductivity measurement

DC conductivity of the samples were measured by two plate method. It is one of the simplest and cost effective methods. The schematic diagram of the two plate DC conductivity is shown in Fig. 2.13.

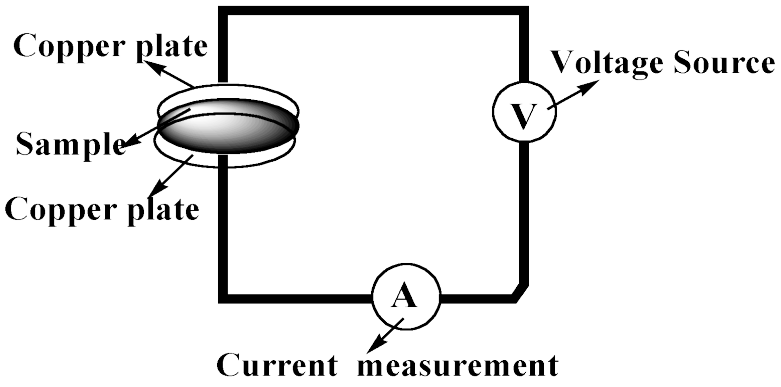

Fig. 2.13. Block diagram of DC conductivity measurement set up.

Sample preparation for conductivity measurement is same as the preparation done for dielectric measurements. DC conductivity measurements are carried out by measuring the current through a sample for a fixed voltage. 2V DC potential was applied across the sample and current was recorded by varying the temperature. DC conductivity of the samples were calculated by the following equation,

$$\sigma_{dc} = {}^{l}/_{RA} \qquad (2.4)$$

Where *l*, R and A is the thickness, resistance and area of the pellets respectively.

2.13. Thermoelectric measurement setup

Seebeck coefficients of the materials were measured by a computer interfaced thermopower measurement setup as shown in Fig.2.14. The measurement of thermoelectric power is simple and its sign gives vital information about the type of electric conduction in semiconductor i.e., whether it is due to holes or electrons. The carriers at hot surface move faster than that of carriers at cold surface which yield net transport of charges to the cold side. This results in negative voltage at the cold side for metals and n- type semiconductors whereas positive voltage for p- type semiconductors.

Fig. 2.14. Thermopower set up, Department of Physics, Goa University.

2.14. Ferroelectric measurements

Ferroelectric measurements for the samples were carried out using P-E hysteresis loop tracer (Marine india). The measurement system consists of four main parts such as P-E main unit, sample holder, furnace with temperature controller, Desktop PC. For the measurements the powder samples were made into circular pellets of thickness ranging between 2.5mm to 1.5mm and the diameter of 6mm using hydraulic press with pressure of 3tons.

Specifications:

- Voltage Range (without external amplifier): ±25 V or higher
- Voltage Range (with external amplifier): ±10 kV or higher
- Minimum hysteresis frequency: 0.03Hz or lower
- Maximum hysteresis frequency: 100 kHz or higher
- Minimum charge resolution: 1fC or lower
- Maximum charge resolution: 1 mC or higher

2.15. Electrochemical measurements

Electrochemical measurements were carried out with standard three electrode system using a BioLogic VSP-300 electrochemical workstation. Saturated calomel and platinum wire

were used as a reference and counter electrodes respectively. The working Electrodes were fabricated with active material i.e, ($CoWO_4$ (S0) nanomaterial and $CoWO_4/PbWO_4$ (S3) nanocomposites), conductive carbon black and PVDF were mixed together in the ratio of 70:20:10. Then this slurry-like mixture was coated on pre-cleaned nickel foam support (1 cm×1 cm) and then dried in hot air oven at 80°C for 5 h. Then nickel foam coated with sample was pressed using a hydraulic press in the order of 8 MPa. The mass loading of active materials for the electrode is about 3 to 5mg. The electrochemical tests were carried out using 1M KOH aqueous solution as the electrolyte. The electrochemical performances of the prepared electrodes were tested by CV, GCD and EIS measurements. The impedance spectroscopy is measured in the frequency range from 200 KHz to 10 mHz at the open circuit potentials, and the applied potential amplitude.

References

1. B.D. Cullity, *Elements of X-Ray Diffraction*, Second Edi (ADDISON-WESLEY PUBLISHING COMPANY INC., Philippines, 1978).

2. M. Zamkov and C. S. S. R. Kumar, *UV-VIS and Photoluminescence Spectroscopy for Nanomaterials Characterization* (Springer Heidelberg New York Dordrecht London, 2013).

3. B. Stuart, *Infrared Spectroscopy: Fundamentals and Applications* (John Wiley & Sons, Ltd, 2004).

4. C. J. Pereyra, F. Ferrer, C. Gómez, L. Campo, R. E. Marotti, F. Martin, D. Leinen, J. Ramos-Barrado, and E. A. Dalchiele, Matéria (Rio Janeiro) **20**, 747 (2015).

CHAPTER 3

SYNTHESIS AND CHARACTERIZATION OF $CoWO_4/PbWO_4$ NANOCOMPOSITES

3.1. Introduction

Nanocomposites have been studied extensively for enhancing the unique properties of metal oxide semiconductors[1]. Preparation of nanocomposites by wet chemical methods is used to make nanostructured materials with variable optical and electronic properties for the development of new multifunctional materials. In nanocomposites with type I band alignment the band gap of one material completely overlaps the band gap of other adjacent material. If the materials with appropriate band offsets are chosen to form the nanocomposites to trap electron-hole pairs in specific regions of the material then increase in recombinations leading to enhanced luminescent emission intensities occurs [2]. Tungstate nanocomposites have been reported to possess interesting photocatalytic, photoluminescent, electrochemical and thermoelectric applications [3–6]. In this work samples were prepared by coprecipitation method and characterized by various experimental techniques such as X-ray diffraction (XRD), scanning electron microscope (SEM), energy dispersive X- ray spectroscopy (EDS), transmission electron microscope (TEM), high resolution transmission electron microscope (HRTEM), Fourier transforms infrared spectroscopy (FTIR), Zeta potential analysis and X-ray photoelectron spectroscopy (XPS). Synthesis and characterization of $CoWO_4/PbWO_4$ nanocomposites have been briefly discussed in this current chapter.

3.2. Preparation of samples by coprecipitation method

The chemicals were purchased from Sigma-Aldrich and ACROSS organic (part of the fisher scientific). They were of analytical grade and used without further purification. Cobalt nitrate $Co(NO_3)_2 \cdot 6H_2O$ (purity 99.99%), sodium tungstate $Na_2WO_4 \cdot 2H_2O$ (99.99%), Lead nitrate $Pb(NO_3)_2$ were used for sample preparation.

$CoWO_4$ and $PbWO_4/CoWO_4$ nanocomposite samples were prepared at room temperature by co-precipitation method in aqueous medium without any surfactant [14]. $Co(NO_3)_2.6H_2O$, $Pb(NO_3)_2$ and $Na_2WO_4.2H_2O$ were separately dissolved in distilled water to make aqueous solutions and named

as A, B, and C respectively. The solutions A and B were mixed together and stirred for 10 minutes and then the solution C was slowly added to it. The final solution (A+B+C) was stirred for 3 hours and the purple colour precipitate was filtered out. The precursor was washed for several times with distilled water, dried at 100^0C and sintered at 600^0C for 1hour. The samples were labelled according to increase in Pb/Co atomic ratio 0, 0.01, 0.015, 0.028, 0.036 and as S0, S1, S2, S3 and S4 respectively. On the basis of cation percentage, compositions of different samples are given below

$CoWO_4$……S0

$0.99(CoWO_4) - 0.01(PbWO_4)$ …….S1

$0.98(CoWO_4) - 0.02(PbWO_4)$ …….S2

$0.975(CoWO_4) - 0.025(PbWO_4)$ …….S3

$0.97\ (CoWO_4) - 0.03(PbWO_4)$ ……S4

Following are the chemical reaction equations [14]:

$$Co(NO_3)_2.6H_2O_{(s)} + H_2O_{(aq)} \rightarrow Co^{2+}_{(aq)} + 2NO_3^-{}_{(aq)} \quad \textbf{solution A}$$

$$Pb(NO_3)_{2(s)} + H_2O_{(aq)} \rightarrow Pb^{2+}_{(aq)} + 2NO_3^-{}_{(aq)} \quad \textbf{solution B}$$

$$Na_2WO_4.2H_2O_{(s)} + H_2O_{(aq)} \rightarrow 2Na^+_{(aq)} + WO_4^{2-}{}_{(aq)} \quad \textbf{solution C}$$

$$Co^{2+}_{(aq)} + 2NO_3^-{}_{(aq)} + Pb^{2+}_{(aq)} + 2NO_3^-{}_{(aq)} + 4Na^+_{(aq)} + 2WO_4^{2-}{}_{(aq)} \rightarrow CoWO_4/PbWO_{4\ (s\downarrow)} + 4NaNO_{3(aq)}\ (\downarrow)$$

Graphical chart of the preparation method is shown in Fig. 3.1.

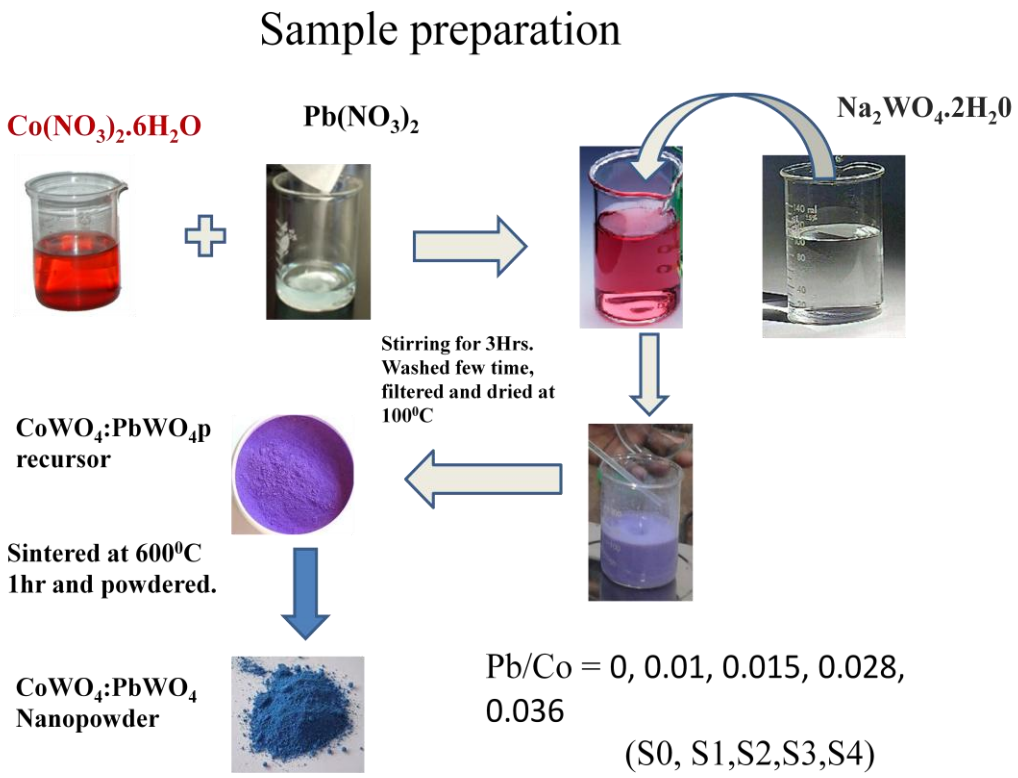

Fig. 3.1. Schematic of sample preparation techniques.

3.3. Characterization

The XRD patterns of the samples were recorded by Rigaku X-ray diffractometer with Cu-K_α radiation. The morphologies of synthesized samples were analyzed by EVO-18 Carl Zeiss scanning electron microscope and Hitachi H-600 TEM. Zeta potential value of the samples is measured by Zetasizer Nano Z Malvern Instruments. Vibrational frequencies of samples were recorded using SHIMADZU IR-8900 Spectrometer. Elemental compositions of the samples were obtained by analyzing EDS recorded with JEOL -JSM 5800 LV scanning electron microscope.

3.3.1. X-ray diffraction analyses

Powder XRD patterns of $CoWO_4$ and $CoWO_4/PbWO_4$ composites sintered at 600^oC are shown in Fig. 3.2.

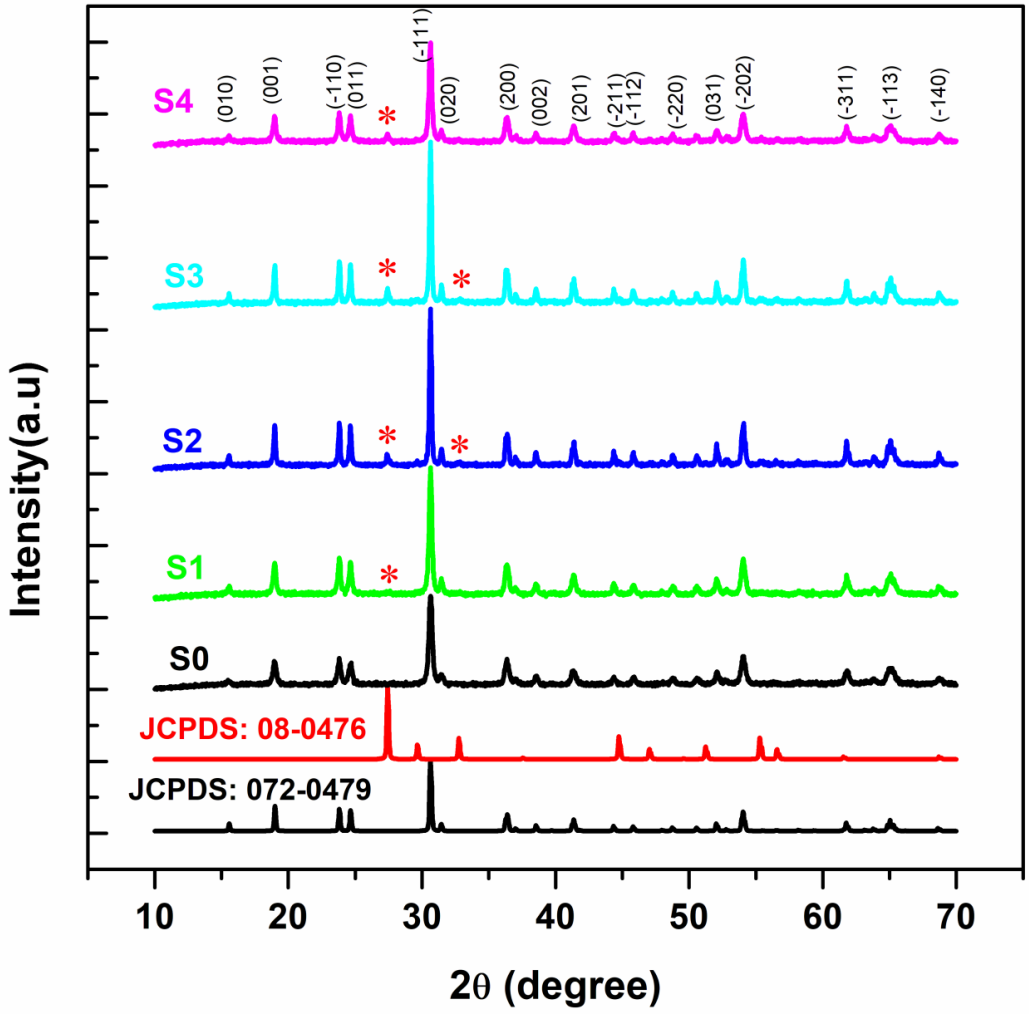

Fig. 3.2. XRD patterns of S0, S1, S2, S3, S4 and samples and '*' denotes $PbWO_4$ phase.

XRD patterns reveal that the sample S0 ($CoWO_4$) shows single phase formation having wolframite monoclinic structure and space group P2/c matching with JCPDS: 072-0479 [7]. All the composite samples [S1, S2, S3 and S4] showed wolframite monoclinic phase of $CoWO_4$, and $PbWO_4$ phase which coincides with the reported data of scheelite-type tetragonal structure with space group I41/a [JCPDS: 08-0476] [8].The location of additional peaks at 27.6^0, 32.8^0 (major peak (121) plane at 27.6^0) is marked by ('*') in the XRD patterns

confirm the $PbWO_4$ phase in the compositesamples. All peaks are exactly indexed to $CoWO_4$ and $PbWO_4$pattern and no other extra peaks of impurity were detected.

3.3.1.1. Crystallite size and lattice strain calculation

The crystallite size and strain of the nanocrystalline samples were calculated using Scherrer formula and Williamson- Hall methods [9] as given in equations (3.1) and (3.2) respectively.

$$D = \frac{K\lambda}{\beta \cos\theta} \qquad (3.1)$$

$$\beta \cos\theta = \frac{K\lambda}{D} + 4\varepsilon \sin\theta \qquad (3.2)$$

where *D*, λ, 2θ, β and ε are the average crystallite size of samples, wavelength of X- ray (1.5418 Å), Bragg angle,full width at half maximum of the XRD peaks and lattice strain respectively. Pseudo Voigt fit for the XRD peaks is shown Fig. 3.3. β value and fitting parameters are also given in the inset of Fig. 3.3. Lattice strain has been obtained from the slope of the linear fit of the Williamson-Hall plot as shown in Fig. 3.4.

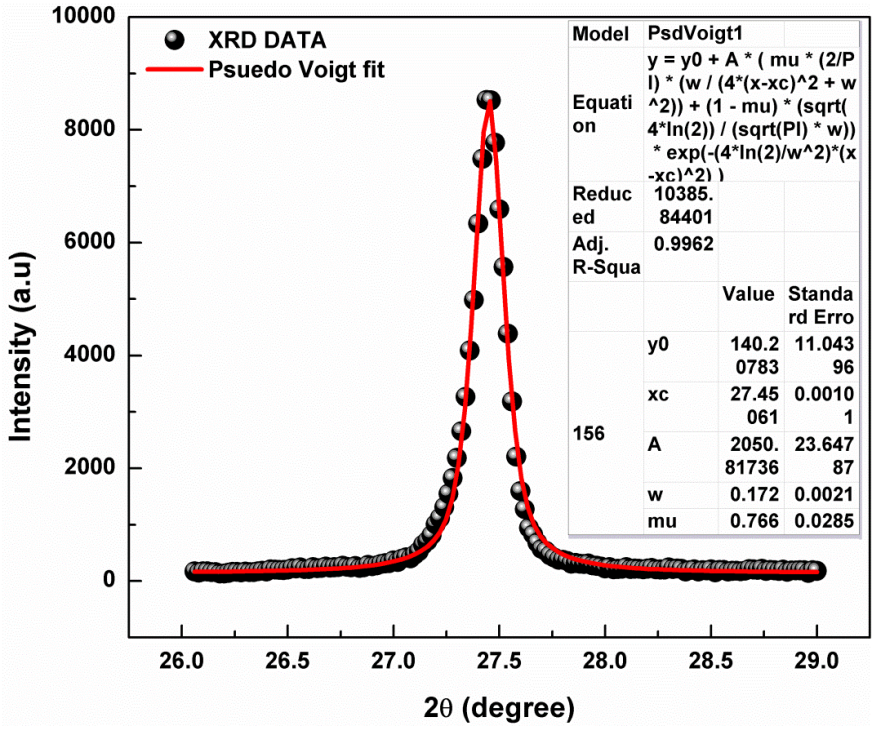

Fig. 3.3. Psuedo Voigt fit of XRD peak for finding the full width half maximum (β)

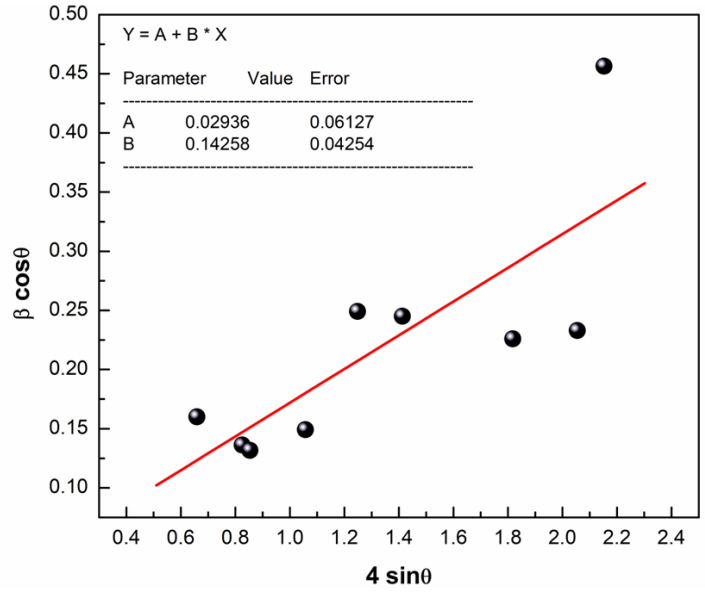

Fig. 3.4. W.H. plot for calculating lattice strain. Red line indicates the linear fit.

Scherrer formula and Williamson-Hall equation[9] are used to estimate the average crystallite sizes and strain for the prominent $CoWO_4$ peaks (001,-110, 011, -111, 200, 201, -202, -311and 113).

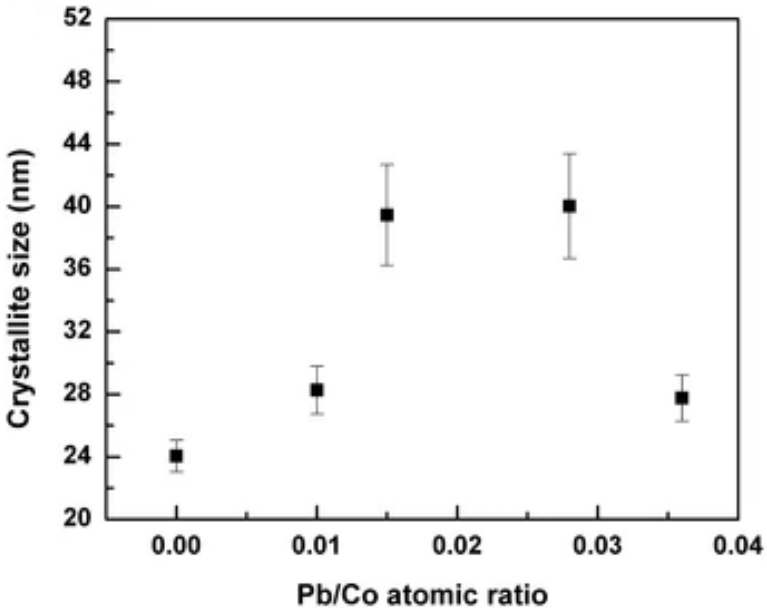

Fig. 3.5(a). Crystallite size (calculated by Scherrer formula) versus Pb/Co atomic ratio.

Fig. 3.5(a) shows the average crystallite size (calculated by Scherrer formula) variation of samples with an increase in Pb/Co atomic ratio. Initially, the crystallite sizes increase with an increase in Pb/Co atomic ratio and then decrease with further increase in Pb/Co atomic ratio. Larger crystallite sizes are observed for samples S2 and S3. Fig. 3.5(b) shows a variation of lattice strain (calculated using Williamson–Hall plots) with increasing Pb/Co atomic ratio. The lattice strain is minimum for S2 and S3 samples.

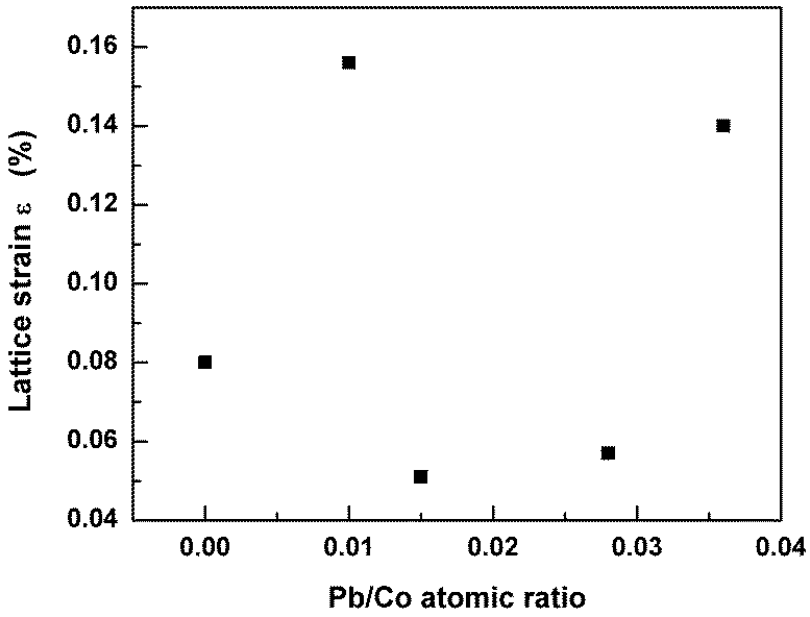

Fig. 3.5(b). Lattice strain versus Pb/Co atomic ratio of $CoWO_4$ and $CoWO_4/PbWO_4$composites.

3.3.1.2. Rietveld refinement analysis

Rietveld refinement of the prepared nanocomposites has been carried out by Fullprof suite software. The pseudo – Voigt function was used to fit the parameter. Rietveld refinement of the nanocomposites is shown in Fig. 3.6 and the obtained values for $CoWO_4$ and $PbWO_4$ phase are given in Table.3.1 and Table.3.2 respectively. These values are matched with the standard value of JCPDS: 072-0479 and JCPDS: 08-0476 for $CoWO_4$ and $PbWO_4$ respectively.

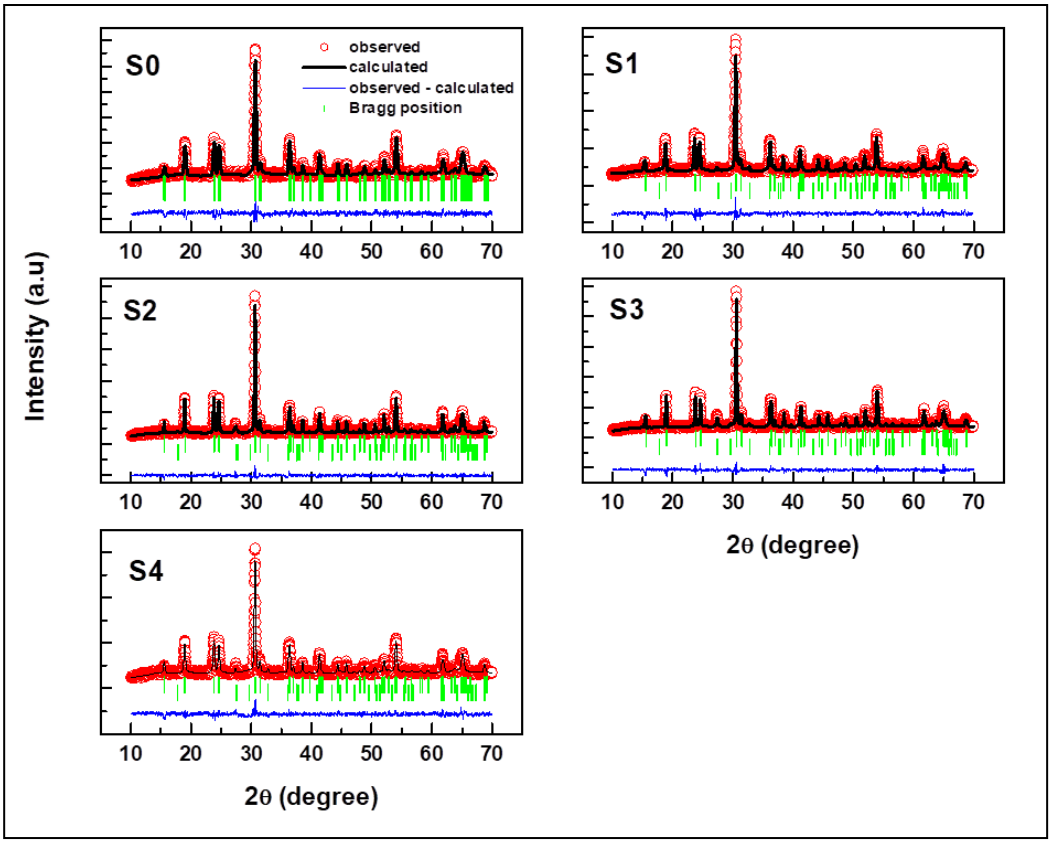

Fig. 3.6. Rietveld refinement patterns of $CoWO_4$ and $CoWO_4/PbWO_4$ composite samples.

Table. 3.1 Lattice constantsin the monoclinic phase of $CoWO_4$ in $CoWO_4/PbWO_4$ nanocomposites.

Samples	*a* (Å)	b(Å)	c (Å)	α =γ(°)	β(°)
S0	4.6658±0.0007	5.6784±0.0007	4.9484±0.0007	90.00	90.11±0.01
S1	4.6893±0.0000	5.7047±0.0000	4.9691±0.0000	90.00	90.10±0.00
S2	4.6729±0.0000	5.6877±0.0000	4.9524±0.0000	90.00	90.04±0.00
S3	4.6604±0.0000	5.6739±0.0000	4.9397±0.0000	90.00	90.08±0.00
S4	4.6739±0.0000	5.6855±0.0000	4.9539±0.0000	90.00	90.12±0.00

Table. 3.2 Lattice constants in tetragonalphase of $PbWO_4$ in $CoWO_4/PbWO_4$ nanocomposites

Samples	*a*=b(Å)	c(Å)	$\alpha = \gamma = \beta(^o)$
S1	5.4729±0.0008	12.0381±0.0015	90.000
S2	5.4381±0.0138	11.7718±0.0614	90.000
S3	5.4622±0.0008	12.0569±0.0050	90.000
S4	5.4616±0.0009	12.0460±0.0056	90.000

3.3.2. SEM, TEM and HRTEM analyses

The surface morphology of the prepared samples is analyzed by using the SEM and TEM. The SEM images of $CoWO_4$ and $CoWO_4/PbWO_4$ are shown in Fig. 3.7(a–e). The sample S0 has some clusters like particles. When $PbWO_4$ phase mixing is done for S1, particles of $PbWO_4$ and $CoWO_4$ start agglomerating. As the atomic ratio of Pb/Co are increased for sample S2 more agglomerations and merging of particles involving $CoWO_4$ and $PbWO_4$ occur. Further increase in the atomic ratio of Pb/Co in sample S3 leads to maximum agglomeration. When the atomic ratio of Pb/Co concentration is still increased in sample S4, agglomeration decreased considerably due to the starting of separation of particles of $PbWO_4$ and $CoWO_4$.

Nano-powder is prone to soft reunion due to its small particles and has a great specific surface. Surface atoms of powder are extremely active for the presence of a large number of vacancy bonds and make the van der Waals force which is quite large. The presence of van der Waals force is easy to cause the particle agglomeration [10]. Researchers found that zeta potential causes particle dispersion[11]. Enrichment of $PbWO_4$ particle in the powder surface is able to increase the surface potential of the powder and repulsive effects between the same kinds of particles. Thereby the action of the van der Waals force is offset and agglomeration of the powder is reduced for S4 sample. These results are also supported by the variation of crystallite size and lattice strain with an increase in molar ratio of Pb/Co as shown in Fig. 3.5(a) and 3.5(b) respectively.

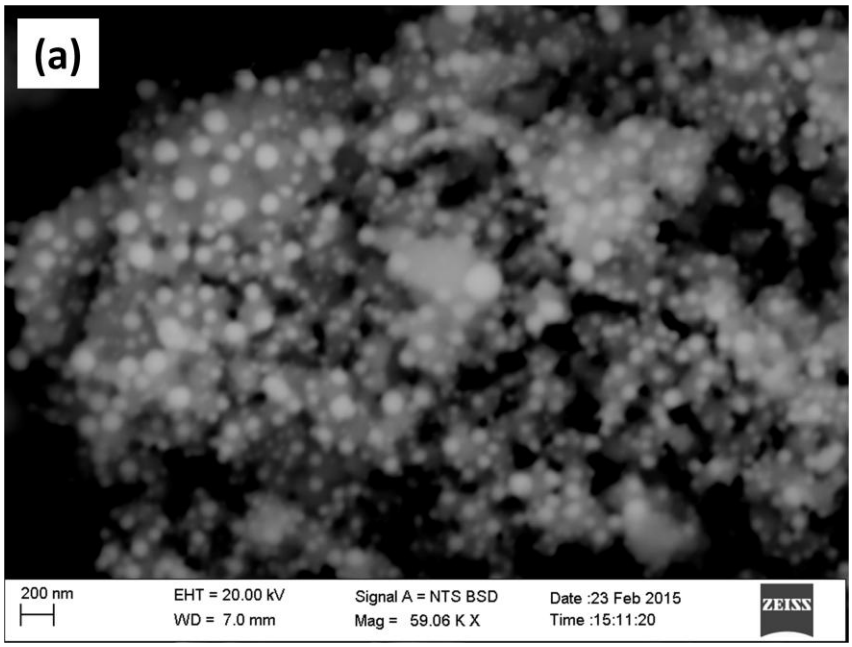
(a)
200 nm
EHT = 20.00 kV
WD = 7.0 mm
Signal A = NTS BSD
Mag = 59.06 K X
Date :23 Feb 2015
Time :15:11:20
ZEISS

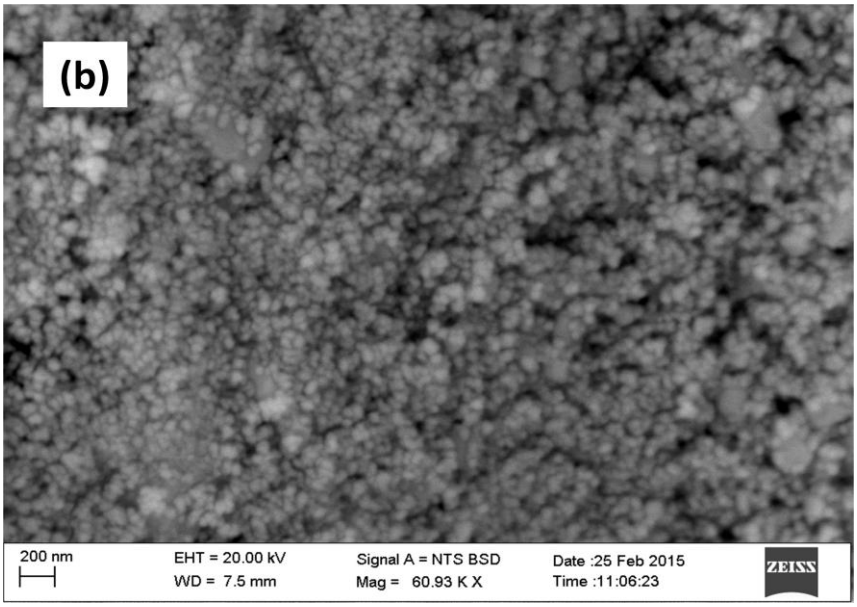
(b)
200 nm
EHT = 20.00 kV
WD = 7.5 mm
Signal A = NTS BSD
Mag = 60.93 K X
Date :25 Feb 2015
Time :11:06:23
ZEISS

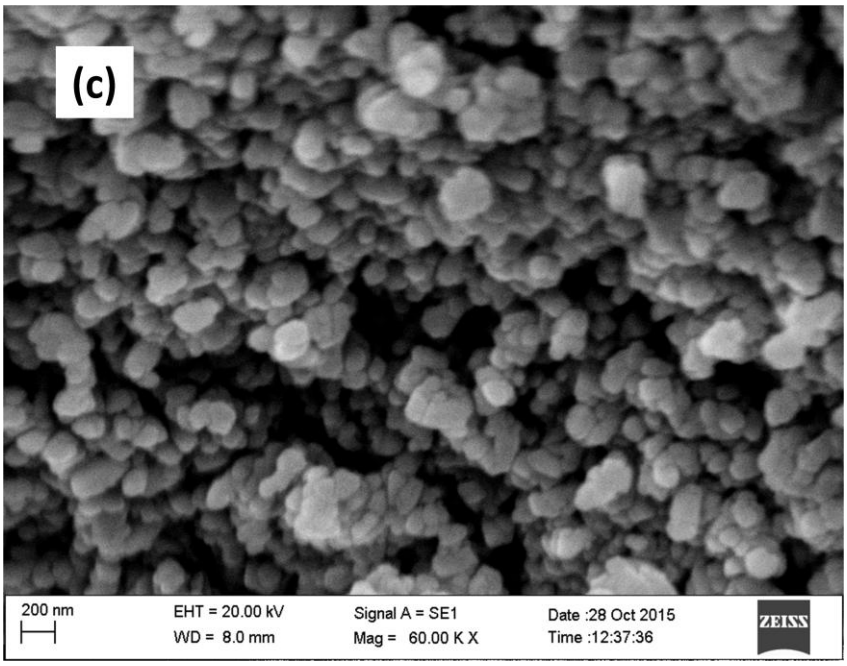
(c)
200 nm
EHT = 20.00 kV
WD = 8.0 mm
Signal A = SE1
Mag = 60.00 K X
Date :28 Oct 2015
Time :12:37:36
ZEISS

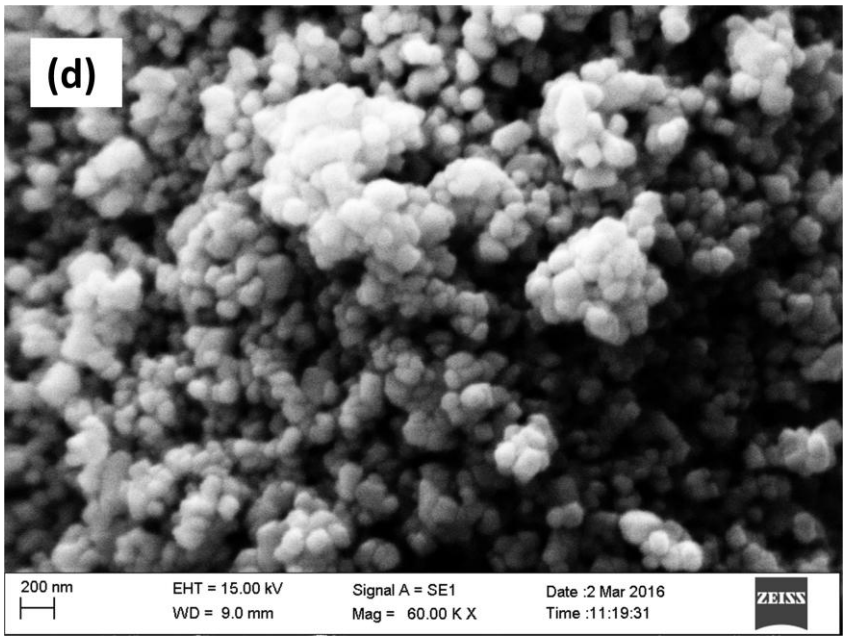
(d)
200 nm
EHT = 15.00 kV
WD = 9.0 mm
Signal A = SE1
Mag = 60.00 K X
Date :2 Mar 2016
Time :11:19:31
ZEISS

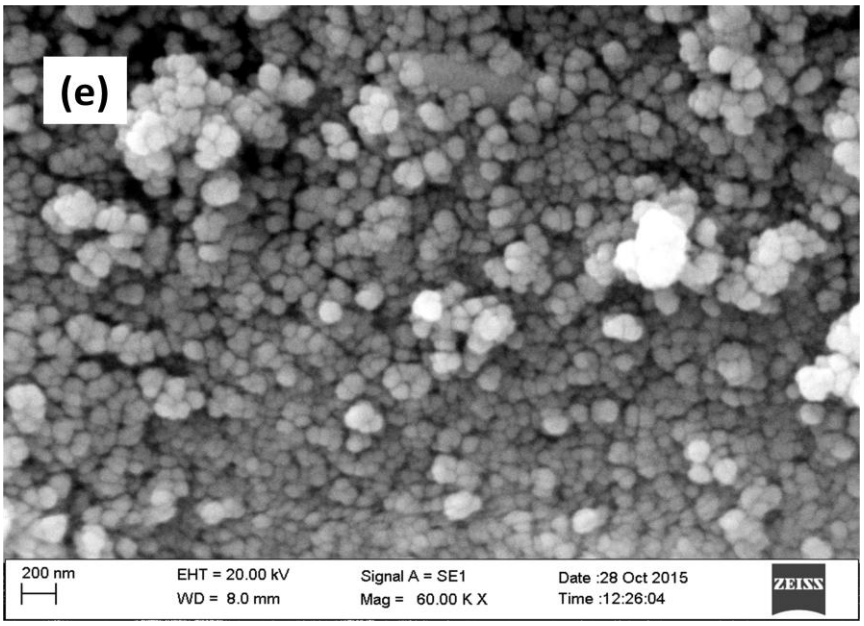

Fig. 3.7. SEM pictures of (a) S0 (b) S1 (c) S2 (d) S3 (e) S4 samples**.**

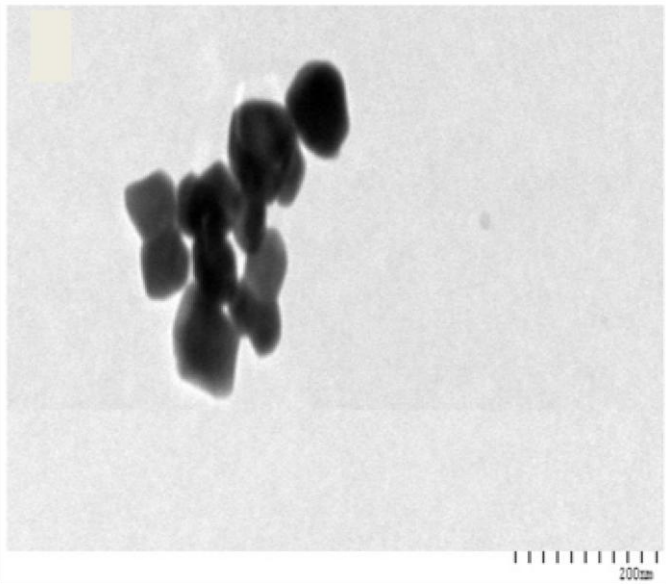

Fig. 3.8. TEM image of S0 sample

TEM micrograph was observed for the S0 sample as shown in Fig. 3.8. The average particle size of the material as observed from TEM micrograph is 50.8 nm with a standard deviation

of ±9.3 nm for an ensemble size of 21 particles and that calculated from XRD pattern using Scherrer formula is 24 nm.

To investigate and confirm the interface formation of the nanocomposite sample, high resolution transmission electron microscope (HRTEM) images of the S3 sample were recorded and are shown in Fig. 3.9(a-d). Randomly shaped nanoparticles are seen on the surface of the samples along with interface formation. This interface may be due to the intra ($PbWO_4$ with $CoWO_4$) or inter ($CoWO_4$-$CoWO_4$ and $PbWO_4$-$PbWO_4$) particle blending. However Fig. 3.9(c) and 3.9(d) illustrate intraparticle blending. Two different morphologies are seen in Fig.3.9 (d). The one where the lattice planes are visible is identified as the $CoWO_4$ phase from the values of interplanar distances 0.56nm and 0.47nm corresponding to (0 1 0) and (1 1 0) planes respectively. Hence HRTEM confirms the interface formation in the nanocomposite S3 sample.

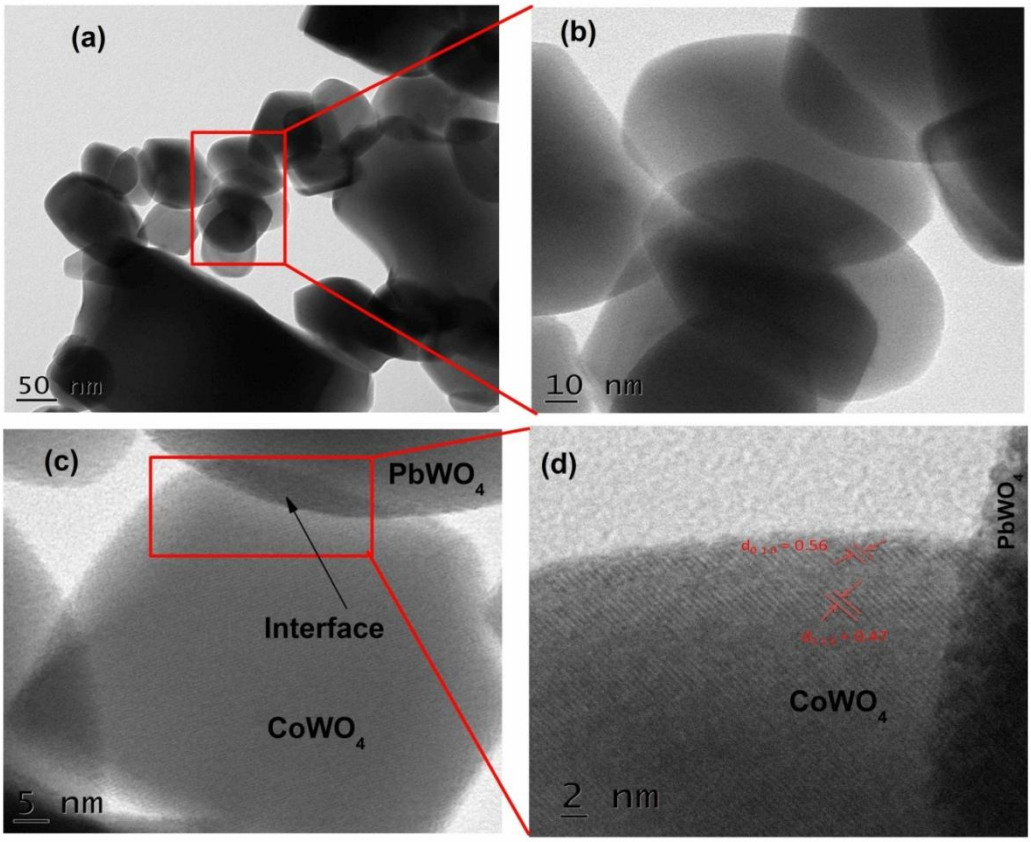

Fig. 3.9 (a-d) HRTEM images of S3 sample.

3.3.3. EDS analysis

The elemental composition presented in $CoWO_4$ and $CoWO_4/PbWO_4$ nanocomposites was carried out using EDS spectral analysis as shown in Fig.3.10 (a-e). These indicate that all the elements were present in the appropriate amount without any impurities. Concentration of the added Pb/Co atomic ratio was calculated from these spectra.

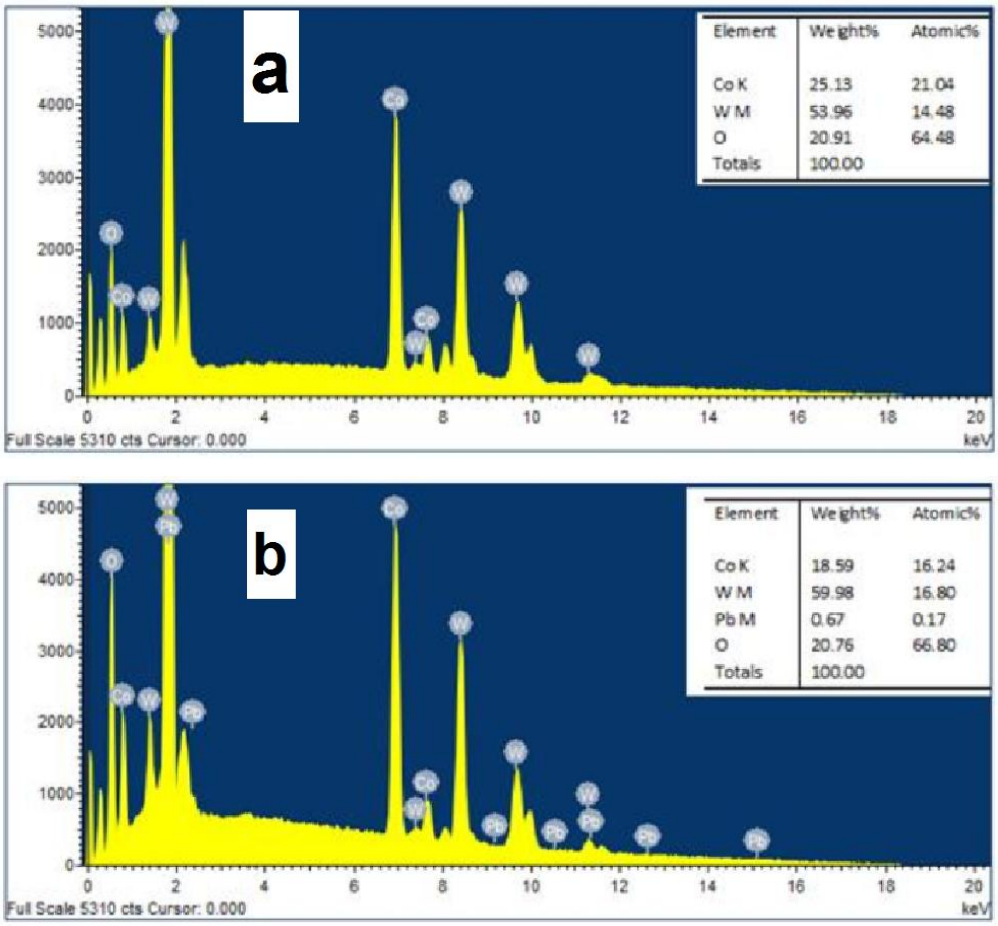

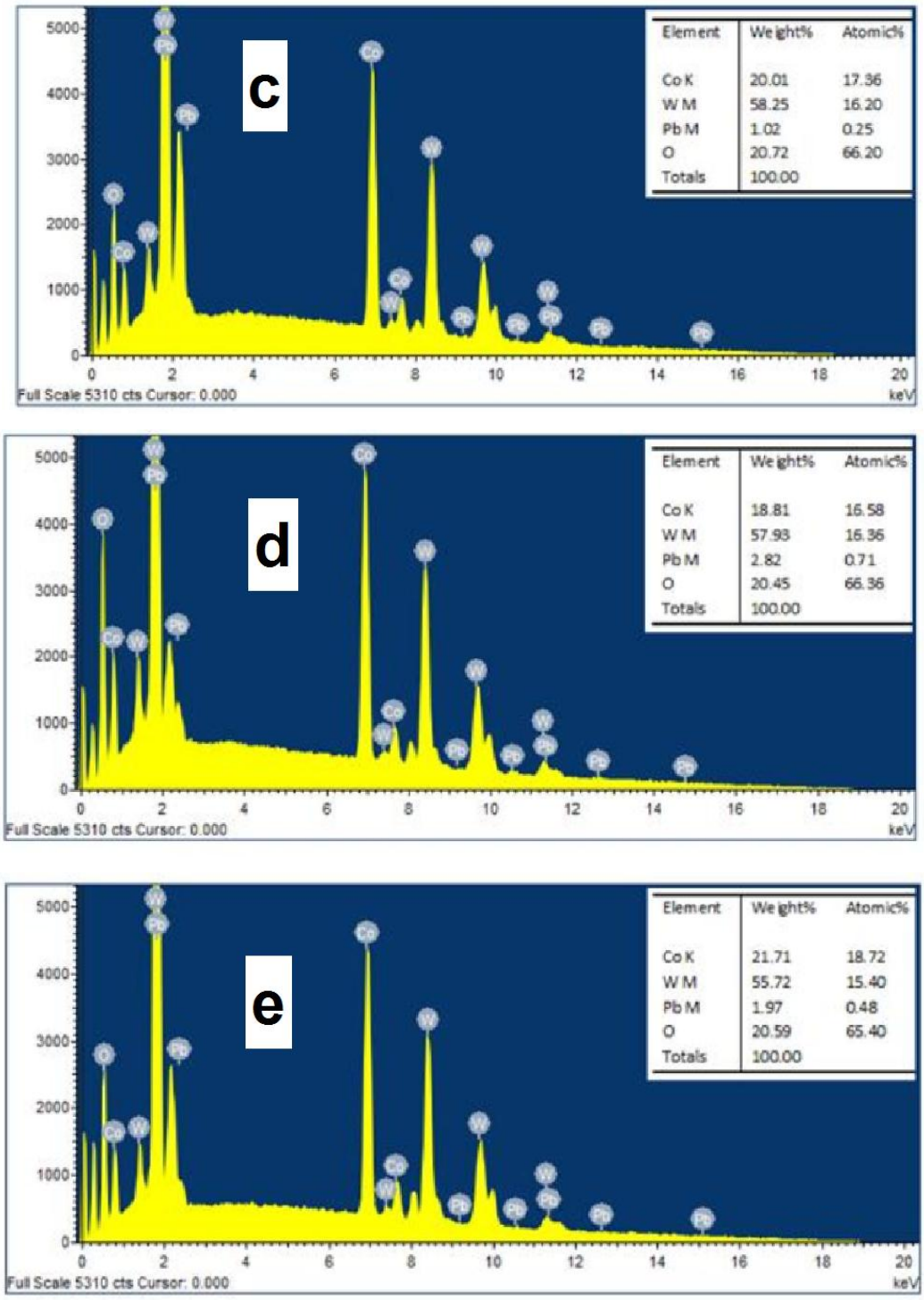

Fig. 3.10. EDS Spectra of (a) S0, (b) S1, (c) S2, (d) S3, (e) S4 samples.

3.3.4. Zeta potential analysis

Agglomeration and dispersion of nanocomposites were confirmed by Zeta potentials analysis. The apparent zeta potential distributions of $CoWO_4$ and $CoWO_4/PbWO_4$ nanocomposites are shown in Fig. 3.11(a-e). Zeta potential values measured for the samples are given in Table 3.3.

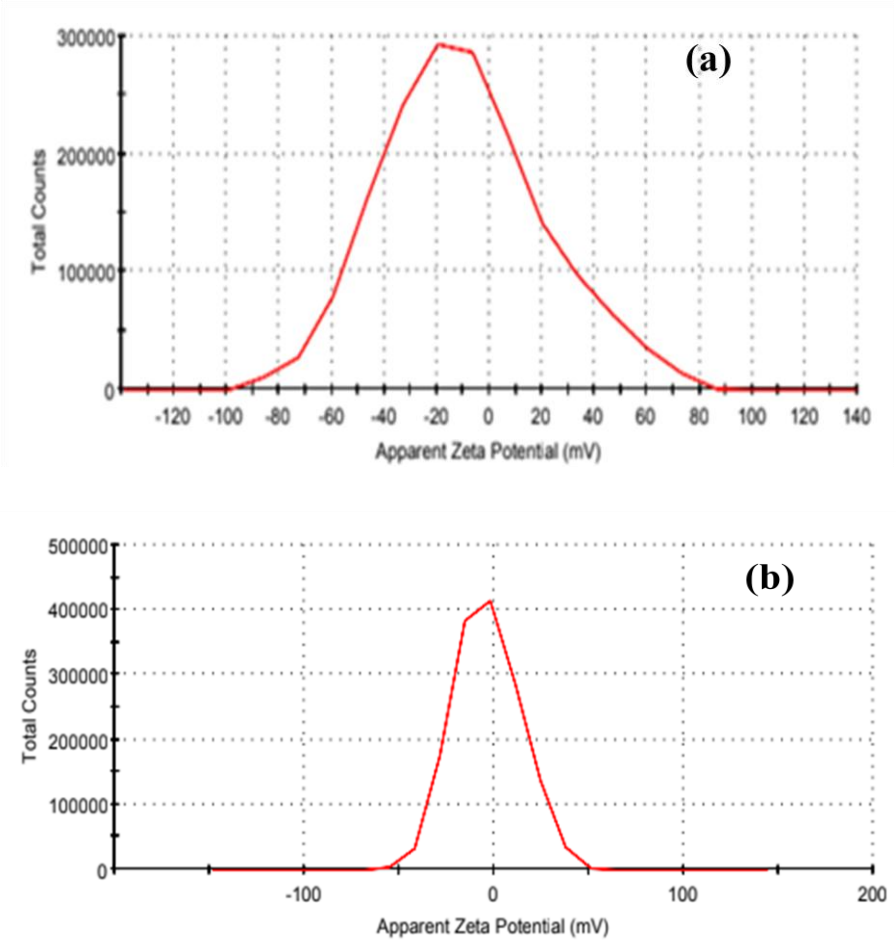

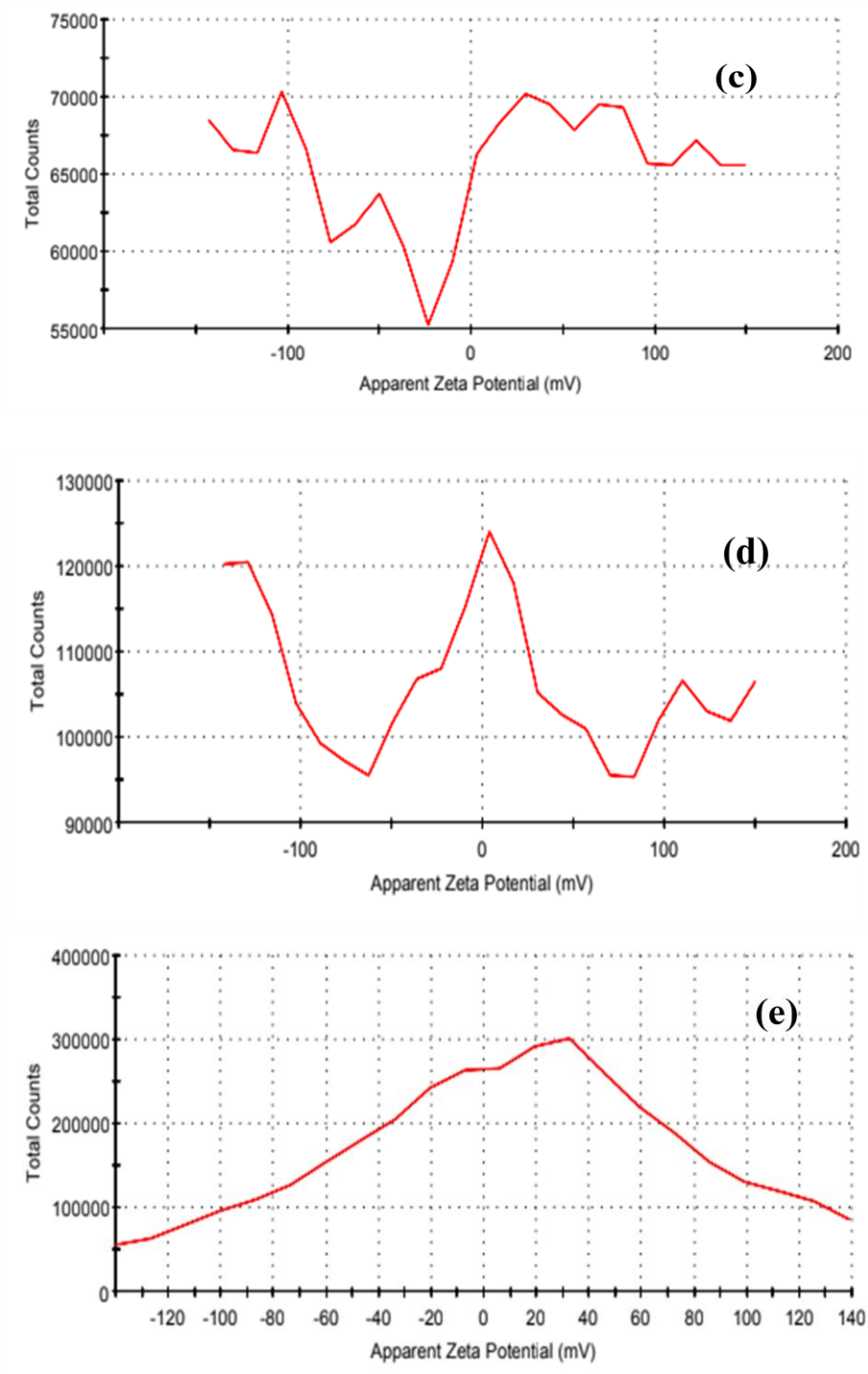

Fig. 3.11. The apparent zeta potential of (a) S0, (b) S1, (c)S2, (d) S3, (e) S4 samples.

Table. 3.3 Zeta potential values of $CoWO_4$ and $CoWO_4/PbWO_4$ samples.

Samples	Zeta potential (mV)
S0	-10.38
S1	-3.66
S2	-2.85
S3	-1.03
S4	+12.3

Lower zeta potential values for samples S2 and S3 confirm larger agglomerations[12]. Samples S0 and S4 gives a higher value of zeta potential so agglomeration of the particles in these samples is less compared than the S2, S3 and S1 samples.

3.3.5. FTIR analyses

The FTIR spectra of the synthesized samples are shown in Fig. 3.12. The stretching absorption bands appearing in the low-frequency region of 400-1000 cm^{-1} belong to the characteristic deformation modes W-O, and W-O-W bridges.

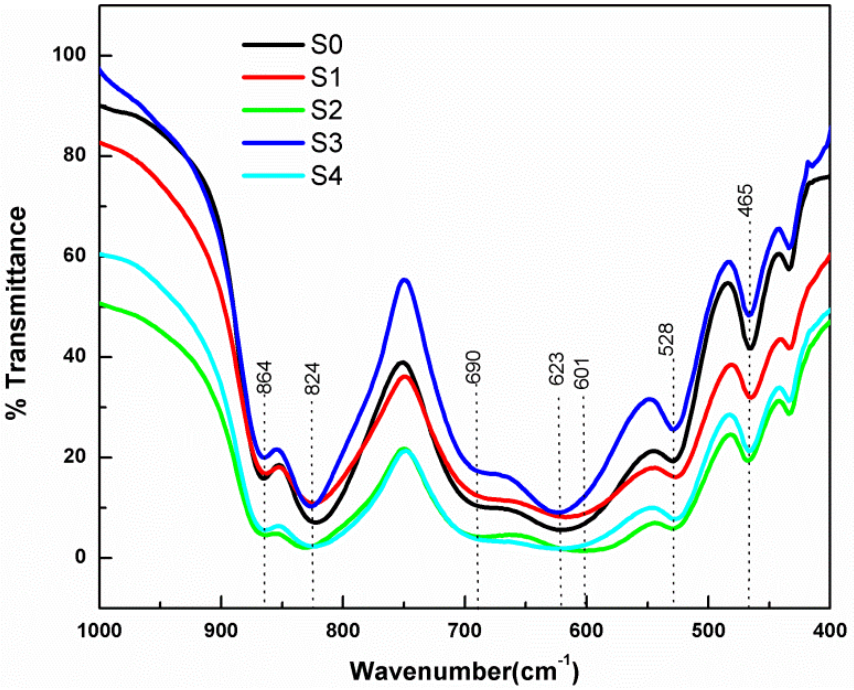

Fig. 3.12. FTIR spectra of S0, S1, S2, S3, S4 samples.

IR spectra below 500 cm^{-1} could be due to the deformation modes of W–O bonds in $[WO_6]^{6-}$ octahedra or the deformation of W–O–W bridges.The bands positioned at 623, 601 and 824 cm^{-1} are associated with the O–W–O vibration mode and the W–O bond stretching, respectively [13]. The bands at 864 and 690 cm^{-1} are attributed to the stretching vibration of W−O−W bridging bonds. The peak appearing at 528 cm^{-1} is due to the asymmetric stretching vibration of the $[WO_6]^{6-}$ group and the stretching mode for W−W bonds. The sharp peak at 465 cm^{-1} is attributed to the bending mode of $[WO_6]^{6-}$ groups.

3.3.6. XPS analysis

XPS spectra of $CoWO_4/PbWO_4$ nanocomposite sample (S3) were recorded and the elements Co, Pb, W and O can be detected in the survey spectrum as shown in Fig. 3.13(a). XPS region of Co 2p is shown in Fig.3.13 (b). The two peaks around BE=781 eV and 797 eV are due to Co^{3+} ions and the satellite peaks around BE=786 eV and 803 eV are due to Co^{2+} ions. The signals at BE=781 eV and 786 eV are the characteristic peaks of Co $2p_{3/2}$ state, whereas those at BE=797 eV and 803 eV belong to the characteristic peaks of Co $2p_{1/2}$ states [14,15]. Fig. 3.13 (c) shows the Pb 4f XPS region. The peaks are located at 137.86 eV (for Pb 4f7/2) and 142.75 eV (for Pb 4f5/2) [16]. Two XPS peaks observed at 34.72 and 36.88 eV correspond to W $4f_{5/2}$ and $4f_{7/2}$ which indicate that W has a valence of +6 in the compound [17]. The high resolution spectrum of W 4f is shown in Fig. 3.13(d). The O 1s peak is obtained at 529.99 eV as shown in Fig. 3.13(e).

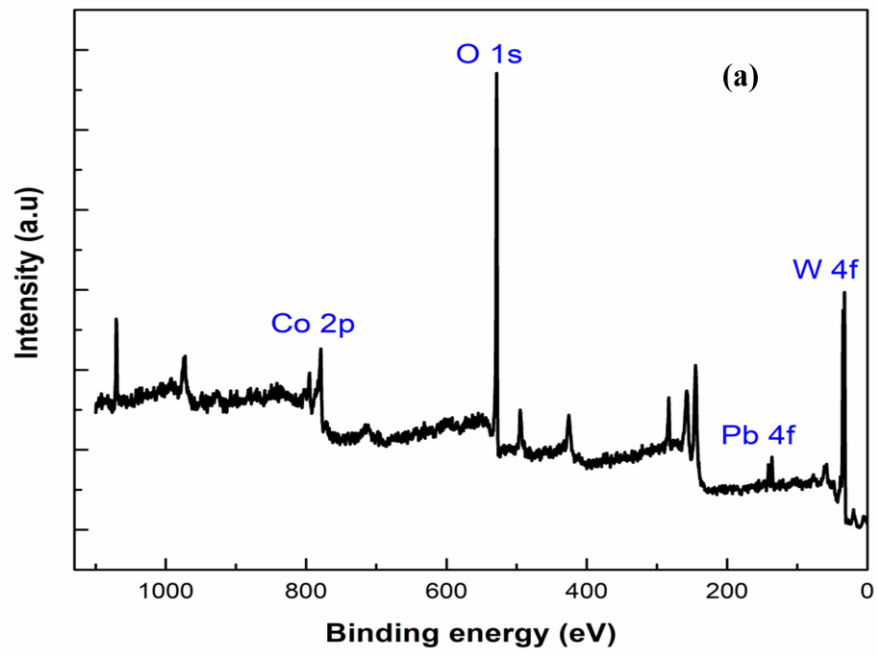
O 1s
(a)
W 4f
Co 2p
Pb 4f
Intensity (a.u)
1000
800
600
400
200
0
Binding energy (eV)

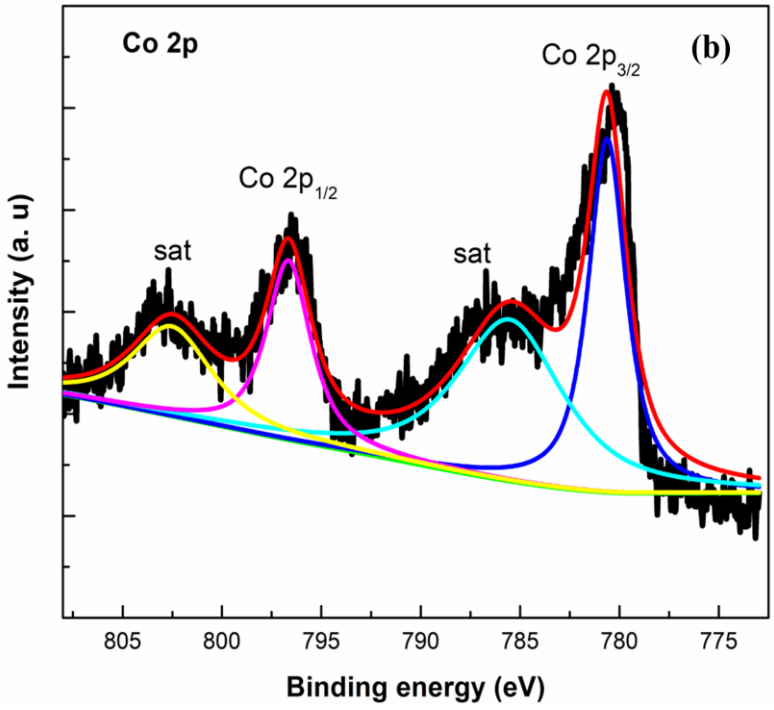
Co 2p
Co 2p3/2
(b)
Co 2p1/2
sat
sat
Intensity (a. u)
805
800
795
790
785
780
775
Binding energy (eV)

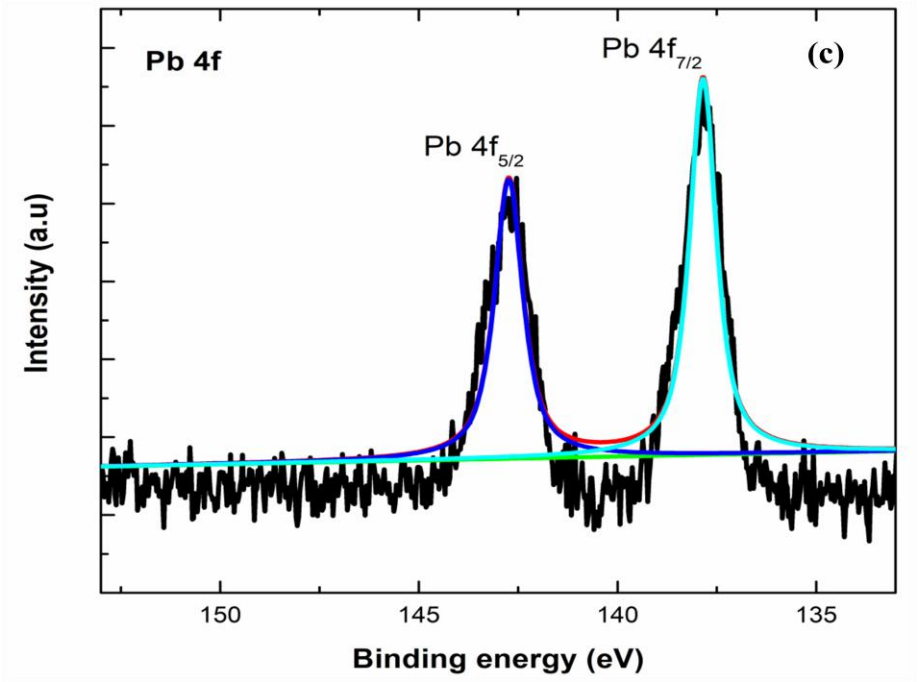
Pb 4f
Pb 4f7/2
(c)
Pb 4f5/2
Intensity (a.u)
150
145
140
135
Binding energy (eV)

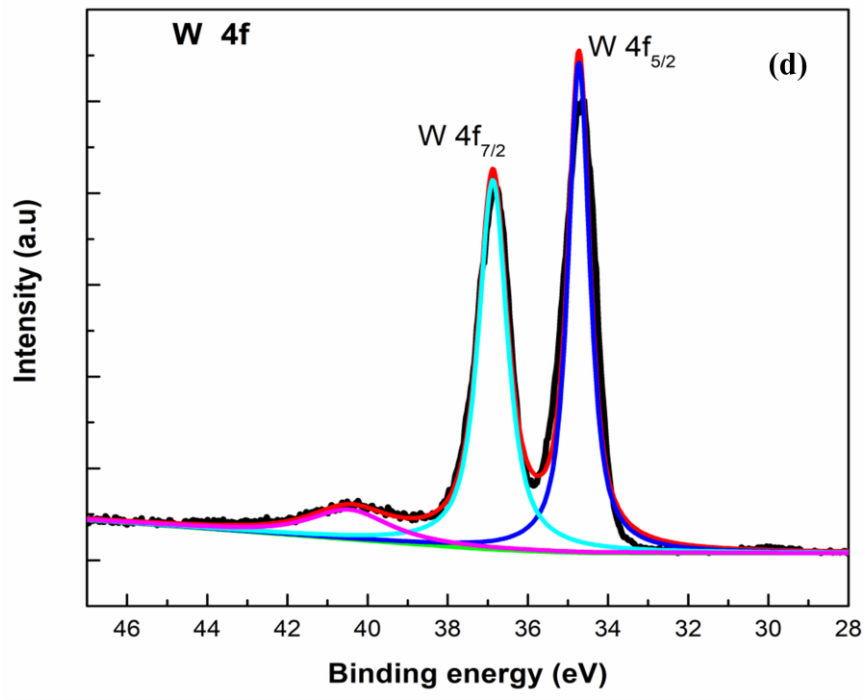
W 4f
W 4f5/2
(d)
W 4f7/2
Intensity (a.u)
46
44
42
40
38
36
34
32
30
28
Binding energy (eV)

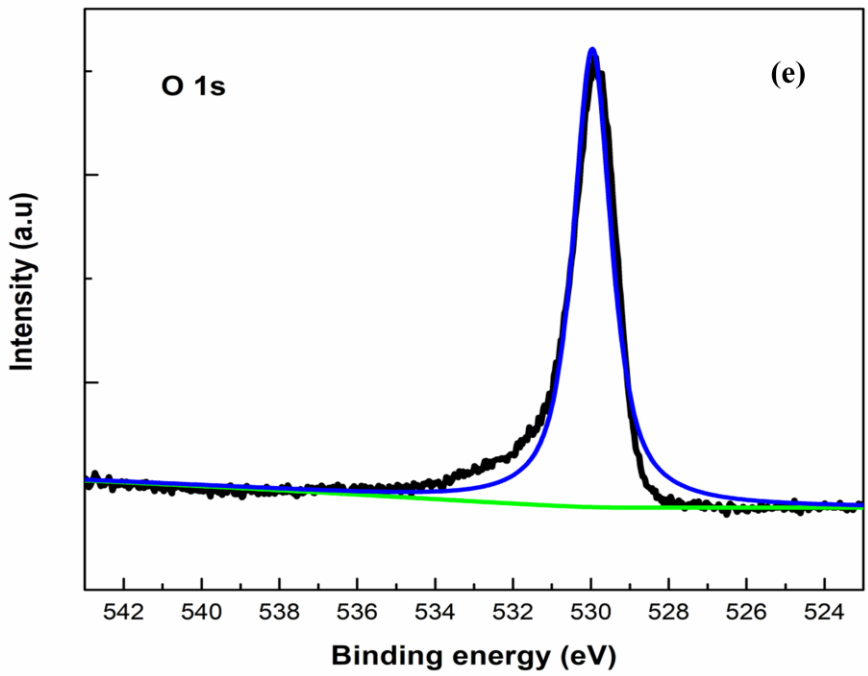

Fig. 3.13. XPS spectra of $CoWO_4/PbWO_4$ nanocomposite S3 sample: a typical survey spectrum (a), Co core level (b), Pb 4f core level (c), O 1s core level (d) and W 4f core level (e).

3.4. Conclusions

$CoWO_4$ and $CoWO_4/PbWO_4$ nanocomposites (crystallite size between 24 and 40 nm by Scherrer formula) were successfully prepared in an aqueous medium by simple co-precipitation method without using a surfactant. XRD analysis confirms the phase purity of the samples and show wolframite monoclinic and wolframite monoclinic along with scheelite tetragonal structure for $CoWO_4$ and $CoWO_4/PbWO_4$ nanocomposites respectively. Larger crystallite sizes are observed for samples S2 and S3 due to higher agglomeration. The agglomeration and dispersion of the surface particles are confirmed by zeta potential analysis. Highly agglomerated sample S3 gives the lowest value of zeta potential. EDS spectral analysis confirms the presence of expected chemical elements and their atomic concentration. Characteristic vibrational bands of $CoWO_4$ and $PbWO_4$ were observed in the FTIR spectra of the samples. XPS spectral analysis reveal the oxidation states of constituent elements present in $CoWO_4$ and $CoWO_4/PbWO_4$ nanocomposites. These initial characterizations show that the samples are prepared successfully.

References

1. F. Sun, X. Qiao, F. Tan, W. Wang, and X. Qiu, J. Mater. Sci. **47**, 7262 (2012).

2. M. Zamkov and C. S. S. R. Kumar, *UV-VIS and Photoluminescence Spectroscopy for Nanomaterials Characterization* (Springer Heidelberg New York Dordrecht London, 2013).

3. Q. Zhang, Q. Meng, and W. Sun, Opt. Mater. (Amst). **35**, 915 (2013).

4. M. Feng, D. An, H. Zhang, G. Ma, C. Zhang, and Z. Ma, Int. J. Chem. Stud. **5**, 1954 (2017).

5. V. B. Kumar and D. Mohanta, Bull. Mater. Sci. **34**, 435 (2011).

6. F. Ahmadi, M. Rahimi-Nasrabadi, A. Fosooni, and M. Daneshmand, J. Mater. Sci. Mater. Electron. **27**, 9514 (2016).

7. S. J. Naik, U. Subramanian, R. B. Tangsali, and A. V Salker, J. Phys. D. Appl. Phys. **44**, 115404 (2011).

8. L. S. Cavalcante, J. C. Sczancoski, V. C. Albarici, J. M. E. Matos, J. A. Varela, and E. Longo, Mater. Sci. Eng. B Solid-State Mater. Adv. Technol. **150**, 18 (2008).

9. P. Bindu and S. Thomas, J. Theor. Appl. Phys. **8**, 123 (2014).

10. Z. Fu-Liang and M. Yan-Shuang, Res. J. Appl. Sci. Eng. Technol. **6**, 2644 (2013).

11. D. Ková, A. Malá, J. M. I, M. Kalina, Z. Fohlerová, A. H. I, P. Skládal, Z. Star, I. Jr, R. Ji, and J. Hubálek, J. Nanomater. **2017**, 1 (2017).

12. R. Marsalek, APCBEE Procedia **9**, 13 (2014).

13. G. M. Clark and W. P. Doyle, Spectrochim. Acta **22**, (1966).

14. Y. Matsumoto, T. Sasaki, and J. Hombo, Inorg. Chem. **3**, 738 (1992).

15. N. I. U. Jianrong, L. I. U. Wei, D. A. I. Hongxing, H. E. Hong, Z. I. Xuehong, and L. I. Peiheng, Chinese Sci. Bull. **51**, 1673 (2019).

16. D. Yue, D. Chen, W. Lu, M. Wang, X. Zhang, Z. Wang, and G. Qian, RSC Adv. **6**, 81447 (2016).

17. C. Zhang, D. Guo, C. Hu, Y. Chen, H. Liu, H. Zhang, and X. Wang, Phys. Rev. B **84**, 035416 (2013).

CHAPTER 4

OPTICAL ABSORPTION AND ENHANCED PHOTOLUMINESCENCE OF $CoWO_4$ IN $CoWO_4/PbWO_4$ NANOCOMPOSITES

4.1. Introduction

Enhancing the photoluminescent (PL) intensity is a challenging task for researchers. There are many ways to improve the PL intensity. In last few decades nanocomposites have been studied extensively for enhancing the unique properties of metal oxide semiconductors. Fabricating nanocomposites with interface is one of the best methods to improve the PL intensity[1]. Metal tungstates are important inorganic ternary oxides. They are also one of the self activated luminescent materials. Metal tungstates nanocomposites are reported extensively for photocatalytic and electrochemical applications [2–5]. There are only few reports available for enhanced PL intensity of tungstates nanocomposites. For example, Yuri V. B. De Santana et al. reported the enhancement of the PL intensity in silver tungstate and silver molybtate nanocomposites[6]. Jian Ming Lin et al reported the enhanced PL emission of ZnO nanorods in SnO/ZnO nanocomposites [7]. The enhanced photocatalytic and photoluminesce of ZnO-$ZnWO_4$ nanocomposites has been reported by Xianvu Jiang et al [3] **.**

$CoWO_4$ is a wolframite structured p-type semiconductor. Little work has been done on the luminescence studies and enhancing the PL of $CoWO_4$ nanocrystals. Ce^{3+} doping in $CoWO_4$ nanomaterial doubled the PL emission intensity as compared to that of undoped $CoWO_4$ due to the formation of Ce_2WO_6 secondary phase [8] and also PL intensity of bulk material sintered at 1000^0C was found to be fourty times less than that of the nanomaterial sintered at 600^0C. Upconversion luminescence of Ce^{3+} doped $CoWO_4$ reported by Uma Subramanian et al [9]. Yb doping in $CoWO_4$ nanoparticles quenches the intrinsic emission[10]. $CoWO_4$ nanowire exhibits IR emission at the ambient temperature under UV excitation. Instead of using single phase material coupling with other semiconductor has also been found to be an effective means to enhance the luminescence properties of oxide nanomaterials[11,12]. $PbWO_4$ is a scheelite structured wide band semiconductor. PL properties of $PbWO_4$ have been widely studied [13–15].

In this chapter we have presented the results and discussion of optical absorption, PL and PL lifetime. Band gap energy, PL intensity and PL lifetime are controlled by the Pb/Co atomic concentration ratio. PL emission which is four times higher than that of the $CoWO_4$ is achieved by introducing and optimizing the additional absorbing $[WO_4]^{2-}$ complexes through $PbWO_4$. Maximum agglomeration due to optimised ratio of Pb/Co (0.028) is found to be advantageous in enhancing the intrinsic luminescence of $CoWO_4$ nanomaterials. We are also discussing the mechanism of enhancement of PL intensity in $CoWO_4$ due to $PbWO_4$ phase.

4.2. Results and discussion

4.2.1. Optical absorption study

Diffuse reflectance spectra of the samples were measured and converted to the absorption spectra by using Kubelka –Munk equation (K-M equation)[16]. Fig. 4.1 shows UV-Visible absorption spectra of the nanocomposites samples. They exhibit an absorption band in the range of 200-475 nm and a broad peak around 586 nm with a small shoulder around 525 nm. The absorption intensities of the band between 200 nm and 475 nm are almost double than that of the broad peak around 586 nm for all the samples. Absorption band in the range of 200-475nm are due to the excitation of electrons from oxygen O_{2p} orbital to tungsten W_{5d} orbital in the $[WO_4]^{2-}$ and $[WO_6]^{6-}$ groups due to ultraviolet energy absorption. In the excited state of $[WO_6]^{6-}$ and $[WO_4]^{2-}$ groups, the hole (on the oxygen) and the electron (on the tungsten) forms an exciton because of their strong interactions[17]. The peak absorption observed around 586 nm is due to the d–d transitions from $^4A_2 \rightarrow {}^4T_{1(P)}$ levels of the Co^{2+} ions [8].

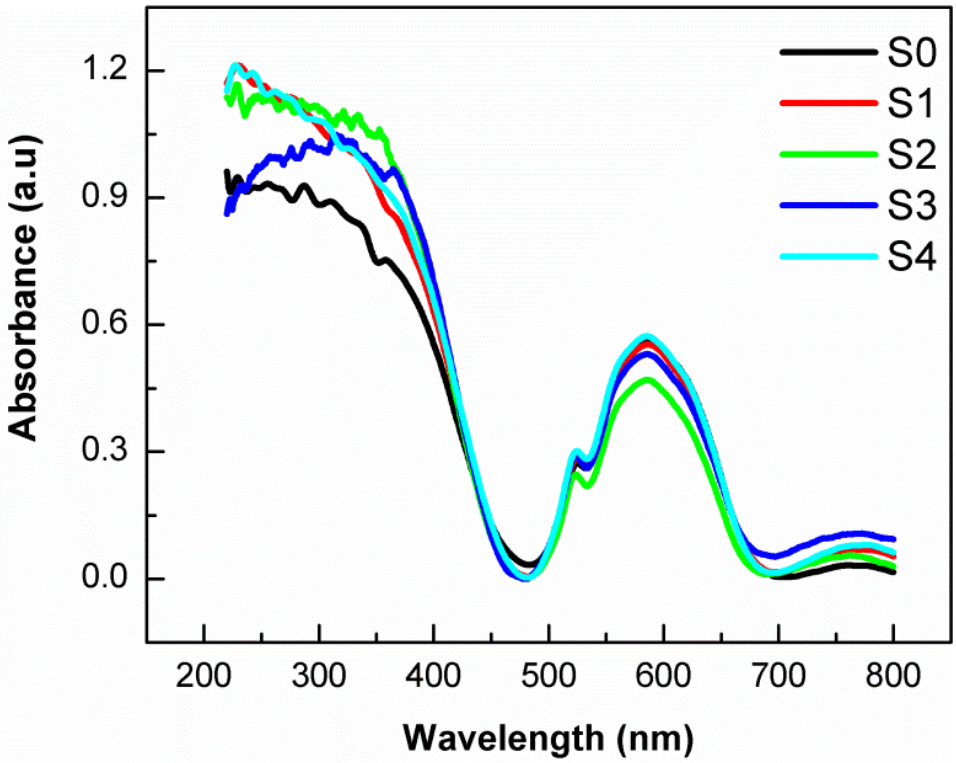

Fig. 4.1. UV-Visible spectra of $CoWO_4$ and $CoWO_4/PbWO_4$ nanocomposites.

From the UV-Vis absorption spectra, the bandgap energy of the $CoWO_4$ and $CoWO_4/PbWO_4$ nanocomposites was calculated by using the following Tauc plot equation

$$\alpha h\vartheta = A(h\vartheta - E_g)^n \qquad (4.1)$$

Where *h* is the Planck's constant, *A* is the constant, α is the absorption coefficient, E_g is the bandgap energy and ϑ is the frequency of the incidence photon. The coefficient *n* can be assigned the values 1/2 and 2 for allowed direct and indirect transitions respectively. Since optical absorption measurements have revealed that wolframite $CoWO_4$ nanomaterial has a direct bandgap with the gap energy in the range of 2.5 – 2.8 eV [8–10,18,19].

By Tauc plotting, the direct optical band gap of the samples are determined at the intercept of the linear part of the curve with$(\alpha h\vartheta)^2 = 0$, as shown in Fig. 4.2 and values are tabulated in Table 4.1.The plotof bandgap energies versus Pb/Co atomic ratio is given in Fig. 4.3. Variation of band gap energy is from 2.856±0.003eV to 2.900±0.003eV. Samples with higher particle size, i.e, S2 and S3 have slightly larger band gap energies as compared to other samples. Generally, the band gap energies shifted to higher energy due to particle size reduction which is explained by quantum confinement effect [20] which is valid only for

particle sizes less than 10 nm. The band gap energies of the present nanocomposites decreased for smaller particle size samples which are similar to that observed in many oxide nanocrystals [21].

Table. 4.1 Bandgap energy of the samples.

Samples	Band gap energy (eV)
S0	2.856±0.003
S1	2.869±0.003
S2	2.900±0.003
S3	2.894±0.003
S4	2.861±0.003

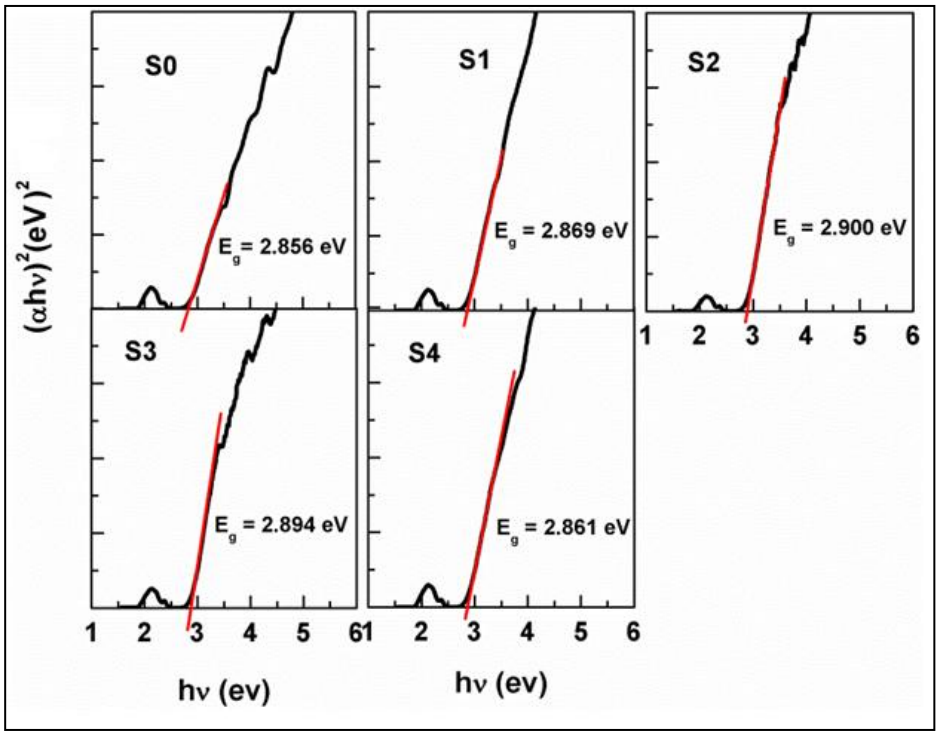

Fig. 4.2. Tauc plot of $CoWO_4$ and $CoWO_4/PbWO_4$ nanocomposites.

From the viewpoint of solid-state physics, energy bands are formed from overlapping orbital states. As the neighbouring atoms are apart from each other within a solid, the basic functions and orbits overlap more weakly, producing decreased dispersion of the electron bands in k space and consequently decreased bandwidths along the energy axis [22]. In other words, the

bandwidth will decrease with the reduction of overlap [23]. Therefore increase in the bandgap energies for more agglomerated samples are due to orbital overlapping of $CoWO_4$ and $PbWO_4$ complexes.

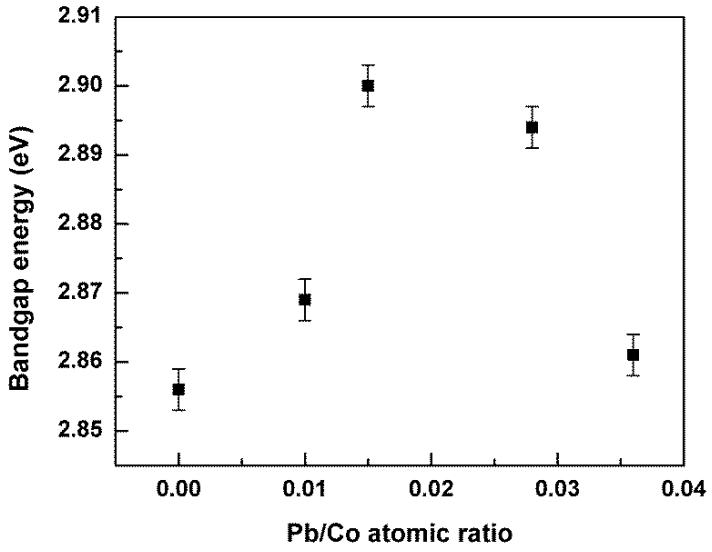

Fig. 4.3. Bandgap energy versus Pb/Co atomic ratio.

4.2.2. Photoluminescence (PL) study

4.2.2.1. PL spectral analysis

Room temperature PL spectra of the samples with 210 nm excitation wavelength are shown in Fig. 4.4. The spectra exhibiting broad bluish – green emissions centred at 467nm and shoulder around 536 nm are intrinsic luminescence of $CoWO_4$ caused by the annihilation of self-trapped excitons, which form excited $[WO_6]^{6-}$ complexes. The $CoWO_4/PbWO_4$ composite changed the PL emission intensities of $CoWO_4$ but did not alter the structure of the spectrum. The 467 nm PL intensity is maximum for S3 sample as shown in the inset of Fig. 4.4 and is four times higher than that of $CoWO_4$ sample PL intensity.

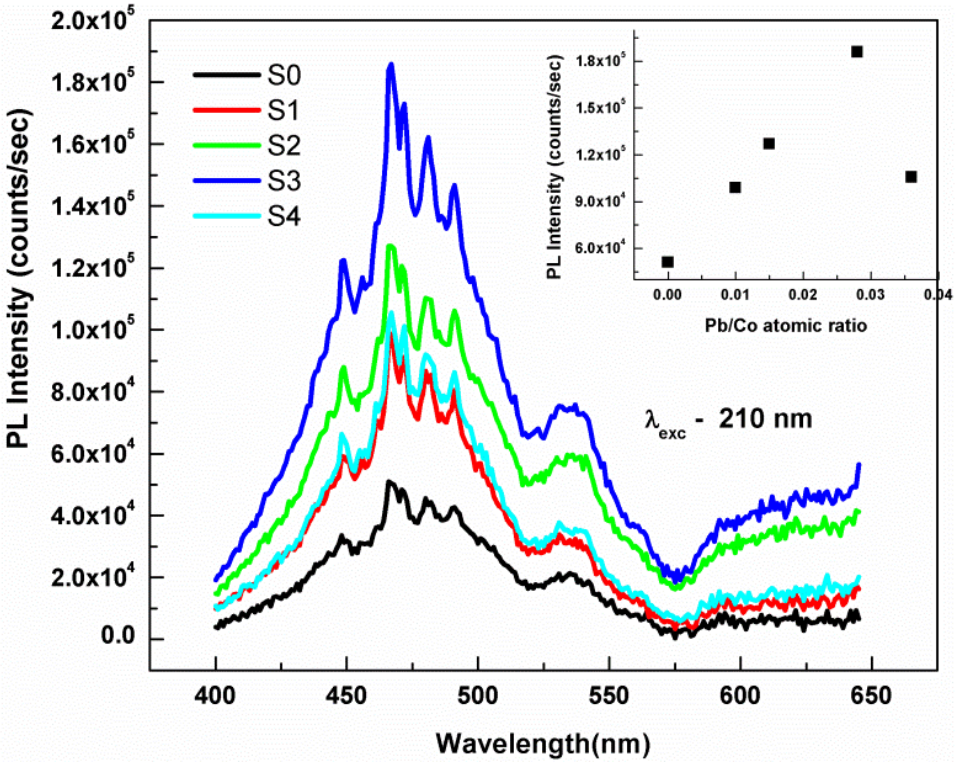

Fig. 4.4. PL spectra of $CoWO_4$ and $CoWO_4/PbWO_4$ nanocomposites excited with 210 nm. Inset shows the variation of PL peak intensity with Pb/Co atomic ratio.

In scheelite and wolframite structured tungstates, the intrinsic luminescence arises due to the annihilation of the self-trapped exciton (STE), which forms excited $[WO_4]^{2-}$ or $[WO_6]^{6-}$ complexes respectively [24,25]. Maximum agglomerations and merging of particles involving $CoWO_4$ (wolframite structured) and $PbWO_4$ (scheelite structured) are there for S3 sample.

4.2.2.2. Possible mechanism for enhancement of PL intensity

The cluster-to-cluster charge-transfer (CCCT) in a crystal, containing more than one kind of cluster, is characterized by excitations involving electronic transitions from one cluster to another. Longo et al. demonstrated that the CCCT mechanism in hierarchical assemblies of $CaMoO_4$ ($[MoO_4]^x$ –$[MoO_3.V^z_O]$ or $[CaO_8]^x$–$[CaO_7.V^z_O]$) and $[(MoO_4]'$–$[MoO_3.V_O]$ or $(CaO_8]^0$– $[CaO_7.V_O]$) can be considered a new class of electronic transitions involved during the PL emissions [26]. In this work we consider the excitonic charge transfer mechanism from the excited $[WO_4]^{2-}$ clusters of $PbWO_4$ to $[WO_6]^{6-}$ clusters of $CoWO_4$ to be

responsible for the enhanced PL intensity of the more agglomerated samples S2 and S3. Band structure diagram and charge transfer processes in $CoWO_4/PbWO_4$ nanocomposites are represented in Fig. 4.5.

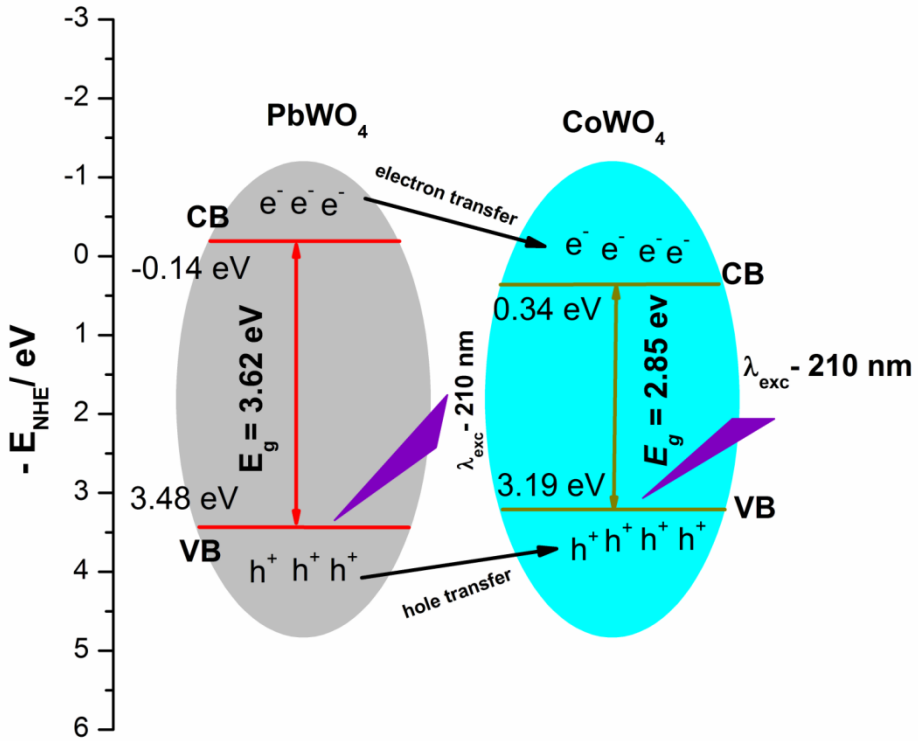

Fig. 4.5. Band structure diagram and charge transfer processes in $CoWO_4/PbWO_4$ nanocomposites.

The conduction band (CB) and valence band (VB) potentials of the samples at the point of zero charge are calculated by the following equation [27] by using the band gap values estimated by us.

$$E_{VB} = X - Ee + 0.5Eg \qquad (4.2)$$

$$E_g = E_{VB} - E_g \quad (4.3)$$

where X is the absolute electronegativity of the semiconductors, which is defined as the geometric average of the absolute electronegativity of the constituent atoms, Ee is the energy of free electrons on the hydrogen scale (4.5 eV), and Eg is the band gap.

For $CoWO_4$, the *X* is calculated to be 6.22 eV, consequently. The band gap values of the $CoWO_4$ and $PbWO_4$ is 2.85 and 3.62 eV respectively. The E_{CB} and E_{VB} values of $CoWO_4$ are estimated to be 0.29 eV and 3.14 eV, respectively. The *X* of $PbWO_4$ is calculated to be 6.13 eV, and the E_{CB} and E_{VB} are estimated to be -0.18 eV and 3.44 eV respectively. Under 210nm UV irradiation, $PbWO_4$ and $CoWO_4$ would be excited simultaneously and generate electron hole pairs. The CB-electrons from the excited $[WO_4]^{2-}$ clusters of $PbWO_4$ would easily flow into the CB edge of $[WO_6]^{6-}$ clusters of $CoWO_4$ through the interface because the CB edge of $PbWO_4$ is higher than that of $CoWO_4$. Also the VB edge level of $PbWO_4$ is lower than that of $CoWO_4$ and holes in the VB edge of $PbWO_4$ will transfer to that of $CoWO_4$ by the control of the interface due to agglomeration leading to more recombination and enhancement of emissions from the $[WO_6]^{6-}$ complexes of $CoWO_4$. Similar results were reported earlier for ZnO/SnO naocomposites[7]. Schematic energy level diagrams on the basis of previously reported literature[28]for the $[WO_6]^{6-}$ complex, excitation and emissions are shown in Fig. 4.6.

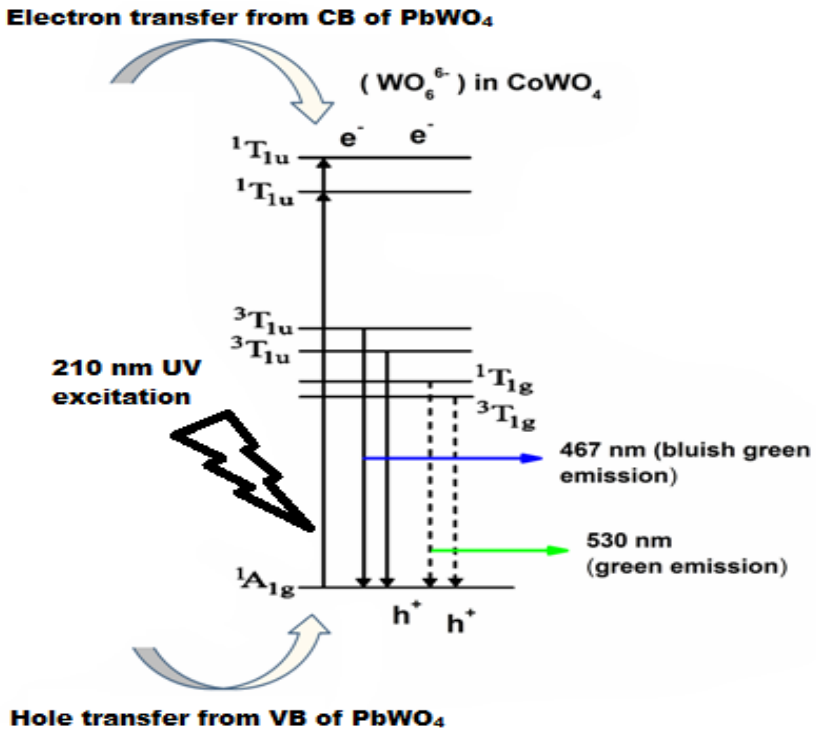

Fig. 4.6. Emissionprocesses from $[WO_6]^{6-}$ complexesof $CoWO_4$ in $CoWO_4/PbWO_4$ nanocomposites.

The transition in $[WO_6]^{6-}$ complexes from two close $_3T^{1u}$ levels to the $_1A^{1g}$ level are responsible for the 467 nm emission. The spin-forbidden transitions from T^{1g} to $_1A^{1g}$ are partly allowed by spin-orbit coupling, and this would contribute to the luminescence on the longer wavelength of 530 nm [28]. In agglomerated samples the orbitals of $CoWO_4$ and $PbWO_4$ complexes are overlapped which favours the transfer of charge from WO_4^{2-} to WO_6^{6-} complexes. Also when the particle size is large due to agglomeration, the surface grain boundaries are less and charge transfer between $[WO_4]^{2-}$ complexes $[WO_6]^{6-}$ complexes increase.

4.2.2.3. PL lifetime

Fig. 4.7 shows PL decay kinetics of 467 nm emission with 210 nm excitation measured at RT. The decay curves were well fitted with single exponential function:

$$I = A\exp(-t/\tau) + I_0 \qquad (4.4)$$

where I_0 and I are the initial and instantaneous luminescence intensities respectively, A is a constant and t is the measurement time. The τ represents the lifetime of the PL emission. The calculated values of τ are tabulated in Table 5.

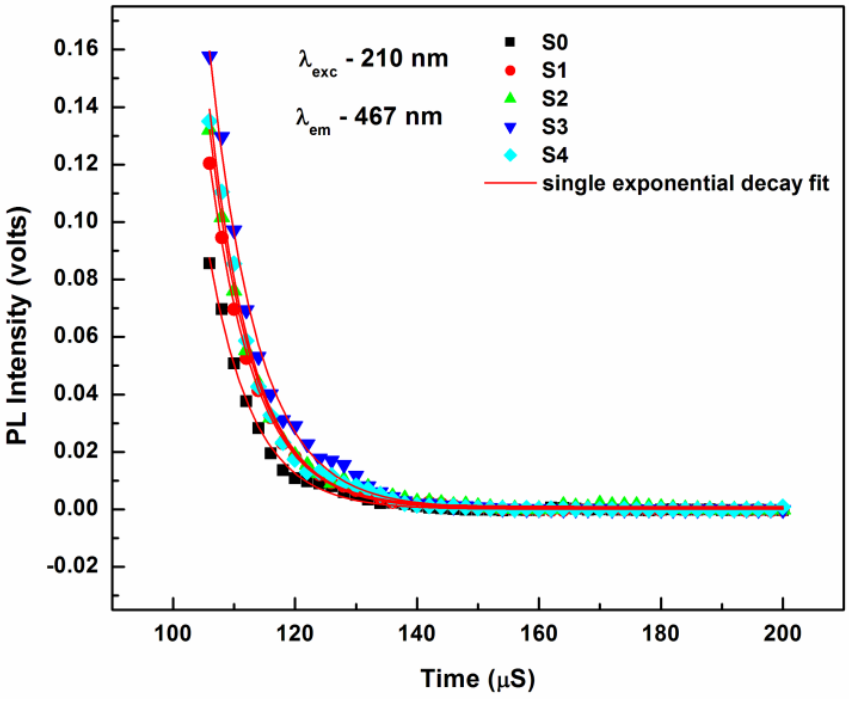

Fig. 4.7. PL decay curves of the samples.

It is observed that PL lifetime of highly agglomerated samples S2 and S3 are little longer (less than 10%) than that of the other samples S0, S1, S4. We believe that, in highly agglomerated samples S2 and S3 the cluster to cluster charge transfer (CCCT) process from WO_4^{2-} to WO_6^{6-} complexes enhances the PL emission lifetime as compared to less agglomerated samples.

Table 4.2 PL lifetime of the samples

Samples	Lifetime (μS)
S0	7.186±0.132
S1	7.174±0.099
S2	7.498±0.075
S3	7.795±0.150
S4	7.180±0.139

4.2.2.4. CIE color coordinates analysis

The CIE (Commission Internationale de I'Eclairage 1931) chromaticity coordinates of the samples S0, S1, S2, S3 and S4 measured to be (0.190, 0.240), (0.190, 0.230), (0.240, 0.270), (0.230, 0.260) and (0.200, 0.240) respectively are presented in Fig. 4.8. It indicates that all the CIE color coordinates are located in the blue region. Also due to higher PL intensities the positions of the coordinates for the highly agglomerated samples S2 and S3 are different than that of the other samples.

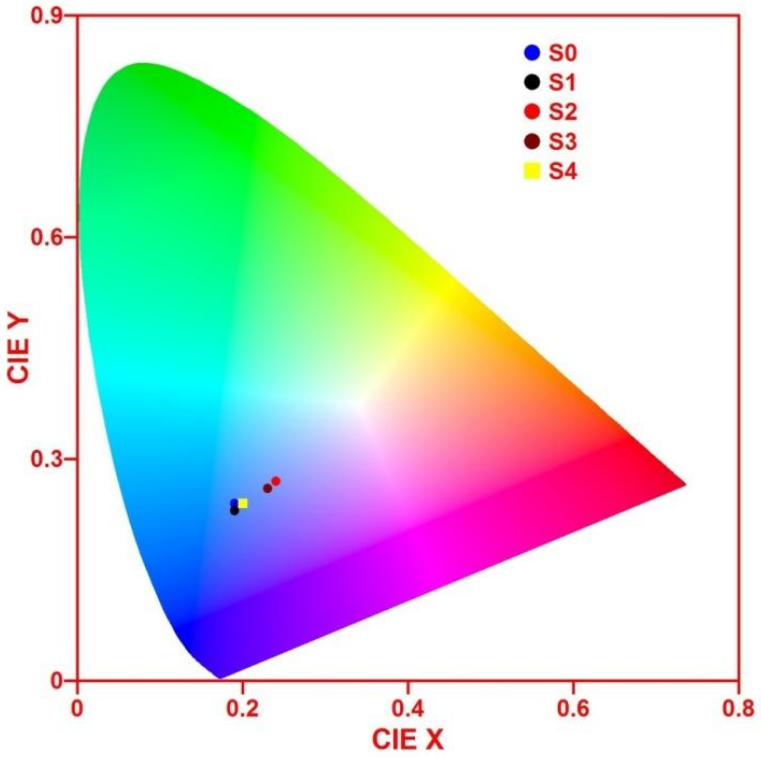

Fig. 4.8. CIE chromaticity coordinates of the $CoWO_4$ and $CoWO_4/PbWO_4$ nanocomposites.

4.3. Conclusion

Higher bandgap energies for more agglomerated samples S2 and S3 could be due to the orbitals overlapping of $CoWO_4$ and $PbWO_4$ compounds. All the samples showed characteristic PL emission of $CoWO_4$. The highly agglomerated sample S3 was giving maximum PL emission which is approximately four times greater than that of S0 ($CoWO_4$) sample. Also slightly longer PL lifetimes (<10% as compared to other samples) for S2 and S3 samples were observed. These are attributed to the cluster-to-cluster maximum excitonic charge-transfer (CCCT) process between $[WO_4]^{2-}$ in $PbWO_4$ and $[WO_6]^{6-}$ in $CoWO_4$ complexes on the surface due to intraparticle agglomeration leading to possible type I band alignment interfacing between $CoWO_4$ and $PbWO_4$ phases. This lead to more number of recombinations of electrons and holes in the $CoWO_4$ phase. Since luminescence is a surface property larger particle size may also contribute to the increase in the PL emission. This nanocomposite can be considered for producing blue component of emission for white light emitting diodes (WLEDs).

References

1. M. Zamkov and C. S. S. R. Kumar, *UV-VIS and Photoluminescence Spectroscopy for Nanomaterials Characterization* (Springer Heidelberg New York Dordrecht London, 2013).

2. Y. Keereeta, S. Thongtem, and T. Thongtem, Powder Technol. **284**, 85 (2015).

3. A. Hamrouni, N. Moussa, A. Di Paola, L. Palmisano, A. Houas, and F. Parrino, J. Photochem. Photobiol. A Chem. **309**, 47 (2015).

4. X. Xu, J. Gao, G. Huang, H. Qiu, Z. Wang, J. Wu, Z. Pan, and F. Xing, Electrochim. Acta **174**, 837 (2015).

5. Y. Wang, C. Shen, L. Niu, Z. Sun, F. Ruan, M. Xu, S. Shan, C. Li, X. Liu, and Y. Gong, Mater. Chem. Phys. **182**, 394 (2016).

6. Y. V. B. De Santana, J. E. C. Gomes, L. Matos, G. H. Cruvinel, A. Perrin, C. Perrin, J. Andrès, J. A. Varela, and E. Longo, Nanomater. Nanotechnol. **4**, 22 (2014).

7. J. M. Lin, C. L. Cheng, H. Y. Lin, and Y. F. Chen, Opt. Lett. **31**, 3173 (2006).

8. S. J. Naik, U. Subramanian, R. B. Tangsali, and A. V Salker, J. Phys. D. Appl. Phys. **44**, 115404 (2011).

9. U. Subramanian, S. J. Naik, R. B. Tangsali, and A. V Salker, J. Lumin. **134**, 464 (2013).

10. J. Juliet Josephine Joy and N. Victor Jaya, J. Mater. Sci. Mater. Electron. **24**, 1788 (2013).

11. H. Y. Lin, Y. Y. Chou, C. L. Cheng, and Y. F. Chen, **15**, 13832 (2007).

12. S. Patole, M. Islam, R. C. Aiyer, and S. Mahamuni, J. Mater. Sci. **41**, 5602 (2006).

13. J. Geng, J. J. Zhu, and H. Y. Chen, Cryst. Growth Des. **6**, 321 (2006).

14. W. Wang, S. Lee, H. Piao, D. Choi, and Y. Son, CrystEngComm **17**, 6548 (2015).

15. C. Zhang, J. Zhang, Y. Li, J. Zhao, W. Wei, R. Yao, and G. Jia, J. Alloys Compd. **698**, 33 (2017).

16. J. Shen, Y. Li, and J. He, Dye. Pigment. **127**, 187 (2016).

17. S. M. M. Zawawi, R. Yahya, A. Hassan, H. N. M. E. Mahmud, and M. N. Daud, Chem. Cent. J. **7**, 1 (2013).

18. S. M. El-Sheikh and M. M. Rashad, J. Clust. Sci. **26**, 743 (2015).

19. J. Timoshenko, A. Anspoks, A. Kalinko, and A. Kuzmin, Phys. Status Solidi Appl. Mater. Sci. **212**, 265 (2015).

20. D. Sun, H. Sue, and N. Miyatake, J. Phys. Chem. C **112**, 16002 (2008).

21. L. Li, J. Liu, Y. Su, G. Li, X. Chen, X. Qiu, and T. Yan, Nanotechnology **20**, (2009).

22. Ü. Özgür, Y. I. Alivov, C. Liu, A. Teke, M. A. Reshchikov, S. Doğan, V. Avrutin, S. J. Cho, and H. Morkoç, J. Appl. Phys. **98**, 1 (2005).

23. Y. Su, B. Zhu, K. Guan, S. Gao, L. Lv, C. Du, L. Peng, L. Hou, and V. V Atuchin, J. Phys. Chem. C **116**, 18508 (2012).

24. V. Pankratov, L. Grigorjeva, D. Millers, S. Chernov, and A. S. Voloshinovskii, J. Lumin. **95**, 427 (2001).

25. A. A. Blistanov, B. I. Zadneprovskii, M. A. Ivanov, V. V Kochurikhin, V. S. Petrakov, and I. O. Yakimova, Crystallogr. Reports **50**, 284 (2005).

26. L. S. Cavalcante, V. M. Longo, J. C. Sczancoski, M. A. P. Almeida, A. A. Batista, J. A. Varela, M. O. Orlandi, E. Longo, and M. S. Li, CrystEngComm **14**, 853 (2012).

27. H. Huang, S. Wang, N. Tian, and Y. Zhang, RSC Adv. **4**, 5561 (2014).

28. C. Zhang, D. Guo, C. Hu, Y. Chen, H. Liu, H. Zhang, and X. Wang, Phys. Rev. B **84**, 035416 (2013).

CHAPTER 5

ELECTRICAL, THERMOELECTRIC, MAGNETIC AND ELECTROCHEMICAL PROPERTIES OF $CoWO_4$ AND $CoWO_4/PbWO_4$ NANOCOMPOSITES

5. 1. Introduction

In the last two decades, researchers are working on nanocomposite materials for applications in electronic devices because of their multifunctional properties. Dielectric and ferroelectric materials have applications in devices such as dynamic access memory, microwave filters, and voltage controlled oscillators and telecommunication technologies. A lot of research has been done to improve the electrical properties of AWO_4 wolframite and scheelite type materials[1–3]. Researchers found that the fabrication of heterostructure nanocomposites is also one of the better methods to improve the electrical properties of materials[4–6].

Frequency and temperature dependent dielectric constant and AC conductivity, relaxor like nature, thermoelectric properties, ferroelectric nature, field and temperature dependent magnetization and electrochemical properties of $CoWO_4$ and $CoWO_4/PbWO_4$ nanocomposites are briefly discussed in this chapter. For AC and DC conductivity analysis, the S2 sample is not included because its properties are approximately equal to the S3 sample. Electrochemical studies, temperature dependent magnetization and ferroelectric studies were done for S0 and S3 samples only.

5. 2. Results and Discussion

5. 2.1. Frequency dependence of dielectric constant and dielectric loss

Dielectric constants of the samples were calculated using the following relation

$$\varepsilon' = Cd/A\varepsilon_0 \quad (5.1)$$

where ε', ε_0, C, d and A are the dielectric constant, permittivity at free space, thickness and area of the pellets respectively.

Fig. 5.1(a) shows the frequency dependence of dielectric constant ε' at room temperature (RT) for the $CoWO_4$ and $CoWO_4/PbWO_4$ nanocomposites. It reveals that ε'

decreases with increasing frequency. This frequency dispersion is attributed to the Maxell – Wagner polarization model [7]. According to this model dielectric materials are composed of grains and grain boundaries as shown in Fig. 5.1(b).

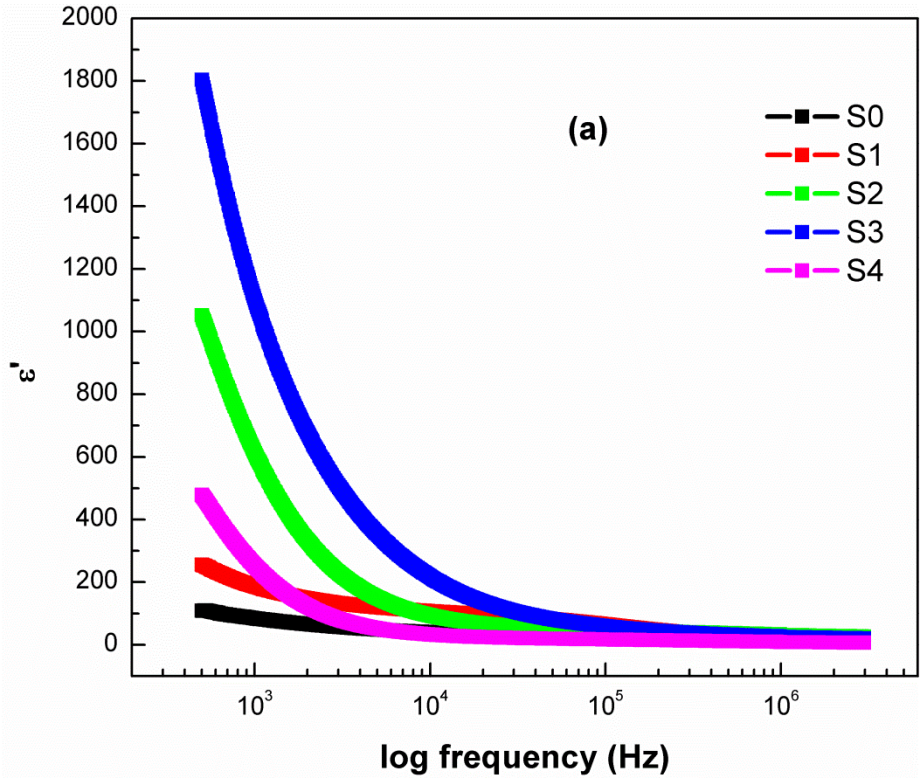

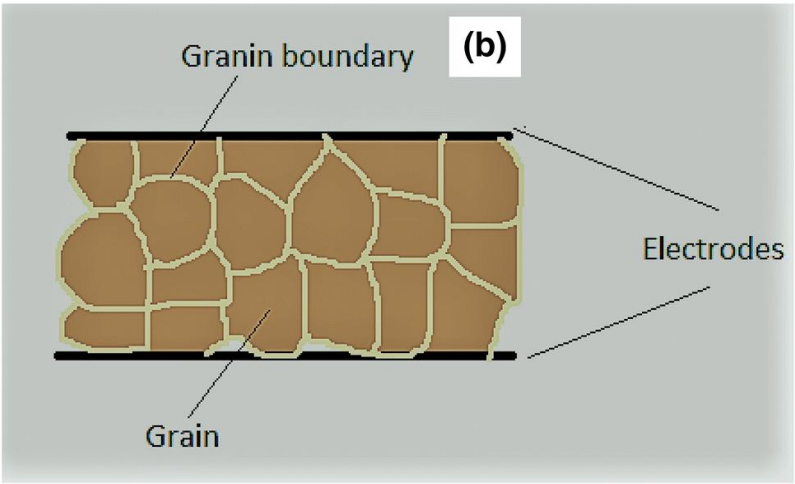

Fig. 5.1(a). Frequency dependence of dielectric constant ε′ for $CoWO_4$ and $CoWO_4/PbWO_4$ nanocomposites measured at room temperature (RT). **(b)** Schematic structure of the sample with electrodes.

The total polarization of dielectric materials is due to the combination of electronic, ionic, orientational and interfacial polarization components. At lower frequencies the charge carriers (holes) are easily migrated through the grains but get accumulated at grain boundaries. This process leads to higher interfacial polarization which results in high dielectric constant at lower frequencies. With increasing frequency the interfacial polarization reduces and becomes negligible while dipolar, ionic and electronic polarizations contribute to the dielectric constant. Thus dielectric constant decreases at higher frequency [8]. With further increase in frequency**,** the orientational polarization of the dipoles lags behind the applied field as compared to electronic and ionic polarization[9]. Therefore ε′ decreases further with increasing frequency and almost reaches a constant value at higher frequencies. The composite samples exhibit higher values of dielectric constant ε′ as compared to single-phase $CoWO_4$ sample and ε′ is maximum for the S3 sample. Agglomeration plays an important role in increasing dielectric constant in these composites samples. As we mentioned in chapter 3, the agglomeration in the composite samples is more than that of a single phase $CoWO_4$ sample. With increase in $PbWO_4$ phase, agglomeration started increasing and became maximum for S3 sample**;** then started decreasing for S4 sample as shown in Table 3.3(*Chapter 3*). The lowest magnitude value of zeta potential reveals the highest agglomeration. The highest value of the dielectric constant is observed for S3 sample due to maximum agglomeration. For the composite samples**,** interfaces between the two phases due to agglomeration may be increasing the accumulation of the dipoles on the interfaces which are also responsible for increased surface charge polarization[10]. When the particles are not interconnected, the contribution of the individual particles to the dielectric constant is limited. Values of **ε′** at 500Hz for the samples are given in Table. 5.1.

Table. 5.1 Values of ε′, ε″ and tanδ for 500Hz at room temperature.

Samples	ε′	Tanδ	ε″
S0	108.4	1.3	140.9
S1	255	4.9	1249.5
S2	1074	10.0	10740
S3	1803.8	2.8	5050.6
S4	478.21	1.1	524

Calculation of dielectric loss ε″ was done using the relation ε″ = ε′ tan δ. Dielectric loss is due to conduction loss, dipole loss and vibrational loss. Fig. 5.2 shows the frequency dependence of dielectric loss ε″ for the $CoWO_4$ and $CoWO_4/PbWO_4$ nanocomposites measured at RT. The dielectric loss decreases with increasing frequency for all the samples. The trend followed by dielectric loss is similar to the dielectric constant. The similar trend of dielectric loss and dielectric constant were observed for other ceramics also reported[11,12]. There are three main possible reasons for dielectric loss with applied frequency such as conduction loss, polarization loss and vibrational loss. At low frequency, the dielectric loss is due to the contribution of conduction losses due to ion migration or ion hopping between the two ion positions and also due to the ion polarization. At higher frequency, the conduction through hopping is less so ion vibration is the only source of dielectric loss [13]. Thus dielectric loss decreases with increasing frequency. The maximum dielectric loss is observed for S3 sample at low and moderate frequencies. This is due to the space charge polarization. The space charge polarization occurs between the sample and electrodes as well as between the two phases (interface). S3 sample has maximum dielectric loss because it has an additional interface, i.e between $CoWO_4$ and $PbWO_4$ phases.

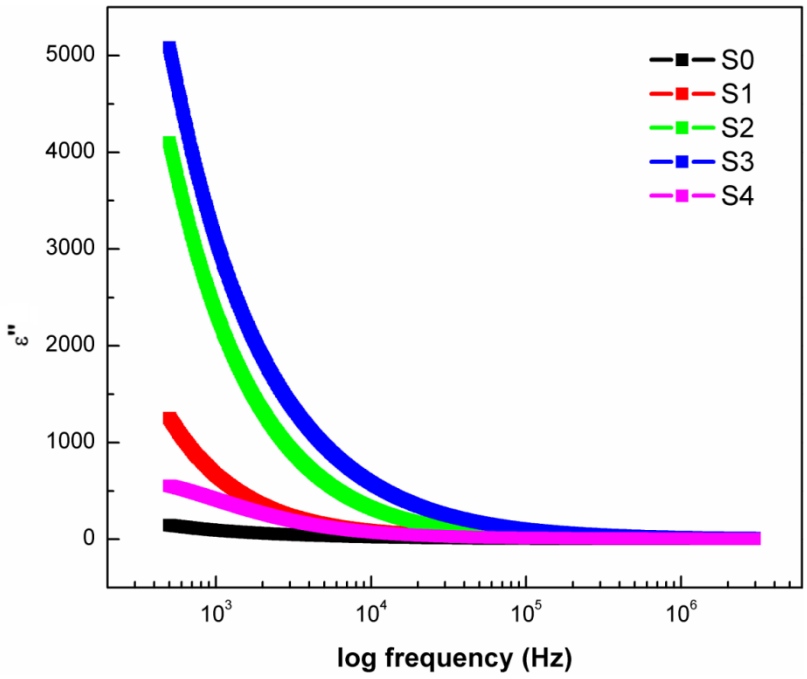

Fig. 5.2. Frequency dependence of dielectric loss ε″ for $CoWO_4$ and $CoWO_4/PbWO_4$ nanocomposites at RT.

5.2.2. Temperature dependence of the dielectric constant

Fig. 5.3 shows the temperature dependence of dielectric constant ε′ for S0, S1, S2, S3, and S4 samples at specific frequencies (1 kHz, 10 kHz, 100 kHz, and 500 kHz, 1 MHz). All the samples show a dielectric constant peak at temperature T_m which is lies between 58^0C to 84^0C. Furthermore, with increasing frequency T_m shifts towards the higher temperature. The composite samples exhibit larger values of maximum dielectric constant (ε_m') at T_m as compared to the single-phase $CoWO_4$ sample (S0) and it is maximum for S3 sample. The colossal dielectric constant ($\varepsilon' \geq 1000$) is observed for higher agglomerated composite samples S2 and S3. Interfaces between the two phases of the composite samples increase the accumulation of dipoles at grain boundaries**,** leading to increased interface charge polarization of the samples and increasing the dielectric constant values. Due to higher agglomeration the interfacing is better for S2 and S3 which leads to colossal dielectric constant.

At still higher temperatures**,** above 200^0C**,** the dielectric constant again increases with increasing temperature. This increase may be due to space charge polarization that arises as a result of ion mobility and ion imperfections. This increase in dielectric constant is larger at low frequencies than at higher frequencies. As we have explained in the previous section accumulation of charge carriers (holes) at the grain boundaries are responsible for the interfacial polarization at low frequencies. Another reason for increasing dielectric constant above 200^0C might be the charge carriers (holes) in the dielectric material are not completely free so they are strongly localized. An increase in temperature leads to thermal activation of charge carriers which could be responsible for increase in dielectric constant above 200^0C. The increase of dielectric constant ε′ with temperature can be attributed to the fact that the orientional polarization is connected with the thermal motion of molecules, so dipoles cannot orient themselves at low temperatures. When the temperature is increased the orientation of dipole is facilitated and this increases the value of orientational polarization, which leads to increase in dielectric constant ε′ with temperature [14].

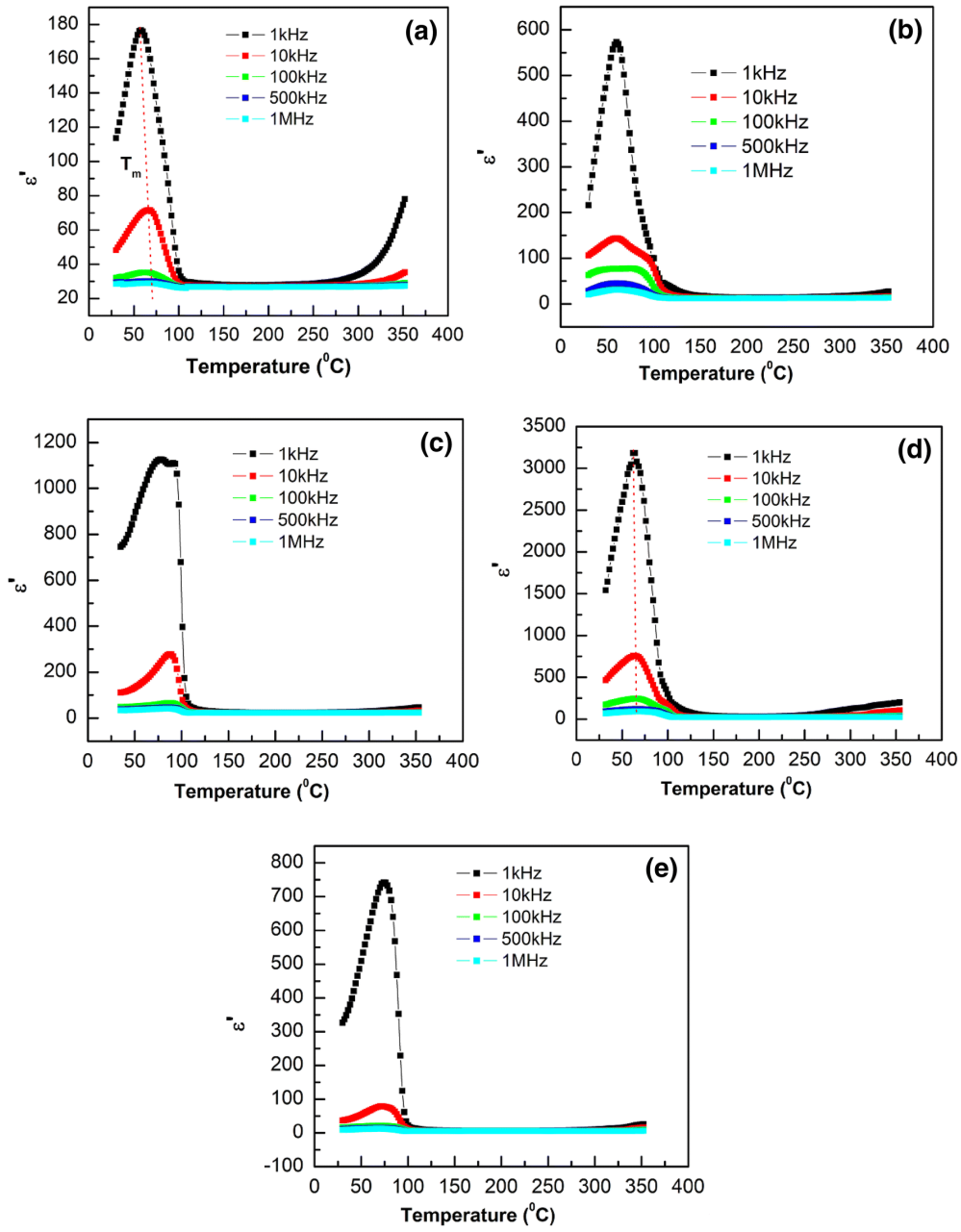

Fig. 5.3. Temperature dependence dielectric constant ε' at different frequencies (a) S0, (b) S1, (c) S2, (d) S3, (e) S4

The frequency dependent anomaly, frequency dependence of dielectric constant in the temperature range 58 to 84 C, is not related to any structural or phase transitions because the XRD pattern of S0 sample recorded at RT and at 170^{0}C, which is above T_m, as given in Fig. 5.4 does not show any structural change in the sample. Also the P-E curves of S0 sample measured at different temperatures 50^{0}C (below T_m), 170^{0}C and 200^{0}C (above T_m) show

ferroelectric hysteresis loops (Fig. 5.18). Therefore this anomaly is not related to phase transitions. This diffuse dielectric anomaly is a very common phenomenon for titanate perovskite materials in the temperature range of 400 – 900^{0}C [6]. This type of anomaly and colossal dielectric constant has been observed at low temperature as around 340K [15]. According to C.C.Wang et al., [16] the mechanism behind this dielectric anomaly and colossal dielectric constant can be divided into two types. One is dipole model associated with different defects especially due to oxygen vacancies. The second one is Maxwell- Wagner model associated with electrical inhomogeneity in the samples.

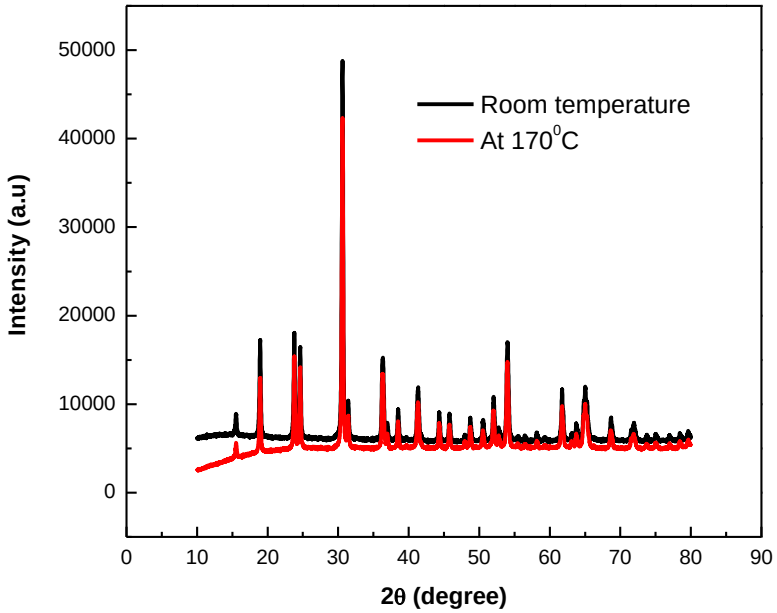

Fig. 5.4.XRD pattern of the $CoWO_4$ nanomaterials at RT and at 170^{0}C.

For relaxor behaviour, the T_m will shift towards the higher temperature with increasing frequency and it will obey the Vogel-Fulcher and modified Curie-Weiss laws [17,18]. The relaxor material will undergo structural or phase transition above T_m. But in relaxor like materials frequency dependent T_m will not obey the Vogel-Fulcher and modified Curie-Weiss laws. Instead of that, they will obey the modified Debye equation and Arrhenius law. But in $CoWO_4$ and $CoWO_4$/$PbWO_4$ nanocomposite samples the peak position can be fitted reasonably well by Vogel-Fulcher law and the fittings yield realistic T_f values (Table.5.4) and also T_m shifts towards higher temperature with increasing frequency. Samples also satisfied the modified Curie-Weiss law. However they do not show any structural or phase transition

above T_m so we can conclude that our samples show relaxor like behaviour. For single-phase $PbWO_4$ nanomaterial the temperature for maximum ε′, i.e T_m is at 60^{o}C and does not vary with frequency revealing non-relaxor nature which is shown in Fig. 5.5. The compositional disorder is the common feature of relaxors [19]. The difference (ΔT_m) of T_m at 1kHz and 500kHz are shown in Table 5.2. The highest value of ΔT_m is observed for S0 sample. Therefore the frequency dependent nature of T_m in our samples may be attributed to the compositional disorder in the $CoWO_4$ phase of the samples due to the commonly present Co^{3+} ions in this phase.

Table. 5.2. The peak temperature (T_m) and ΔT_m of the samples.

Samples	T_m (^{0}C)				ΔT_m (^{0}C) = $T_{m(500kHz)}$ - $T_{m(1kHz)}$
	1kHz	10kHz	100kHz	500kHz	
S0	58	62	64	66	8
S1	72	73	74	76	4
S2	77	79	82	84	7
S3	63	64	66	68	5
S4	74	75	77	79	5

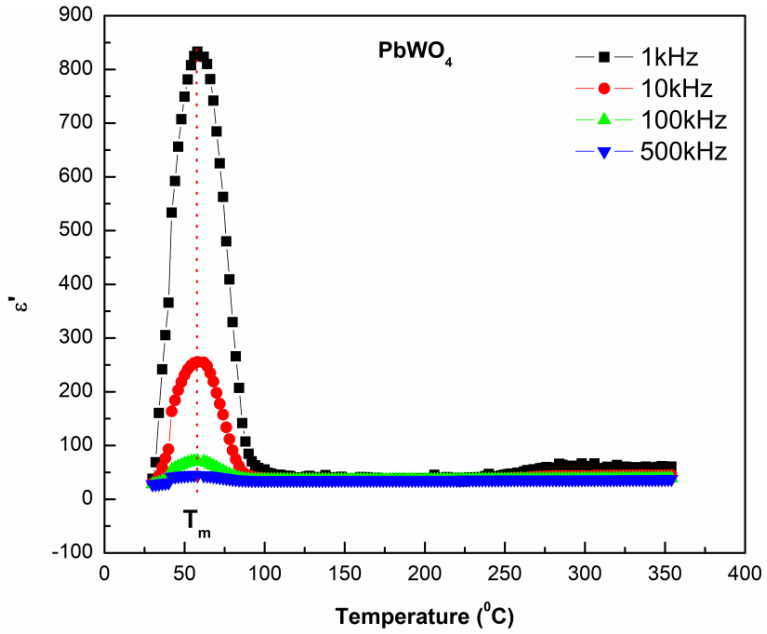

Fig. 5.5. Temperature dependence of dielectric constant ε' at different frequencies (1kHz, 10kHz, 100kHz, 500kHz) for $PbWO_4$ sample sintered at 600^{0}C.

To further clarify the relaxor like nature of the $CoWO_4/PbWO_4$ nanocomposite samples, we have sintered the samples (S0 and S3) at 1000^0C for 1hour and labelled them as S0H and S3H respectively. The XRD patterns of S0H sample shows single-phase Wolframite monoclinic structure and S3H shows two phases which is Wolframite monoclinic ($CoWO_4$) and Scheelite tetragonal ($PbWO_4$) structure. The crystallite size (by Scherrer formula) of the samples has increased from 24nm for S0 sample to 74nm for S0H sample and 39nm for S3 sample to 63 nm for S3H sample. Frequency dependent dielectric constants of the samples sintered at 600^oC (S0 and S3) and 1000^0C (S0H and S3H) as shown in Fig.5.6. The dielectric constant decreased for samples sintered at 1000^oC as compared to samples sintered at 600^oC. Dielectric constant ε' measured at RT and 500Hz are 39and 169 for S0H and S3H samples respectively.

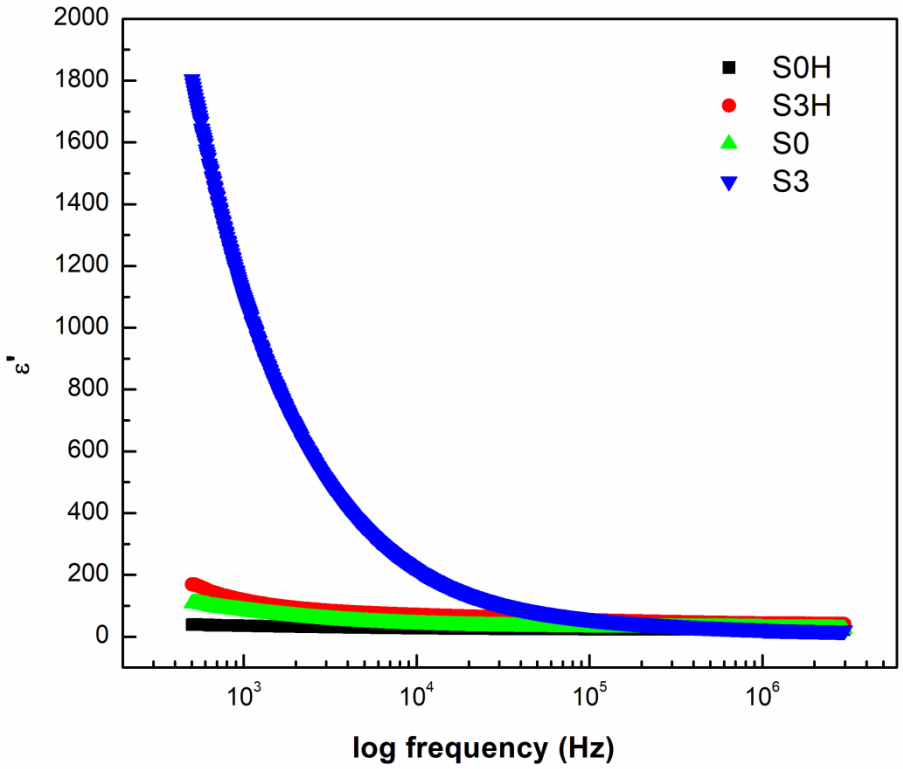

Fig. 5.6. Frequency dependence of dielectric constant ε′ measured at room temperature for samples sintered at 600^oC and 1000^oC.

ε′ versus temperature plots for different frequencies for S0H and S3H samples given in Fig. 5.7(a) and 5.7(b) respectively do not depict relaxor like behaviour in these samples. Also the

maximum dielectric constant (ε_m') at T_m measured at 1kHz for S0H and S3H samples are 42.1 and 890.2 respectively and that of S0 and S3 are 176.7 and 3183.2 (Fig. 5.3(d) and Fig. 5.7(b)). There is a considerable decrease in the values of dielectric constants (ε_m') at T_m after the samples are sintered at 1000^0C.

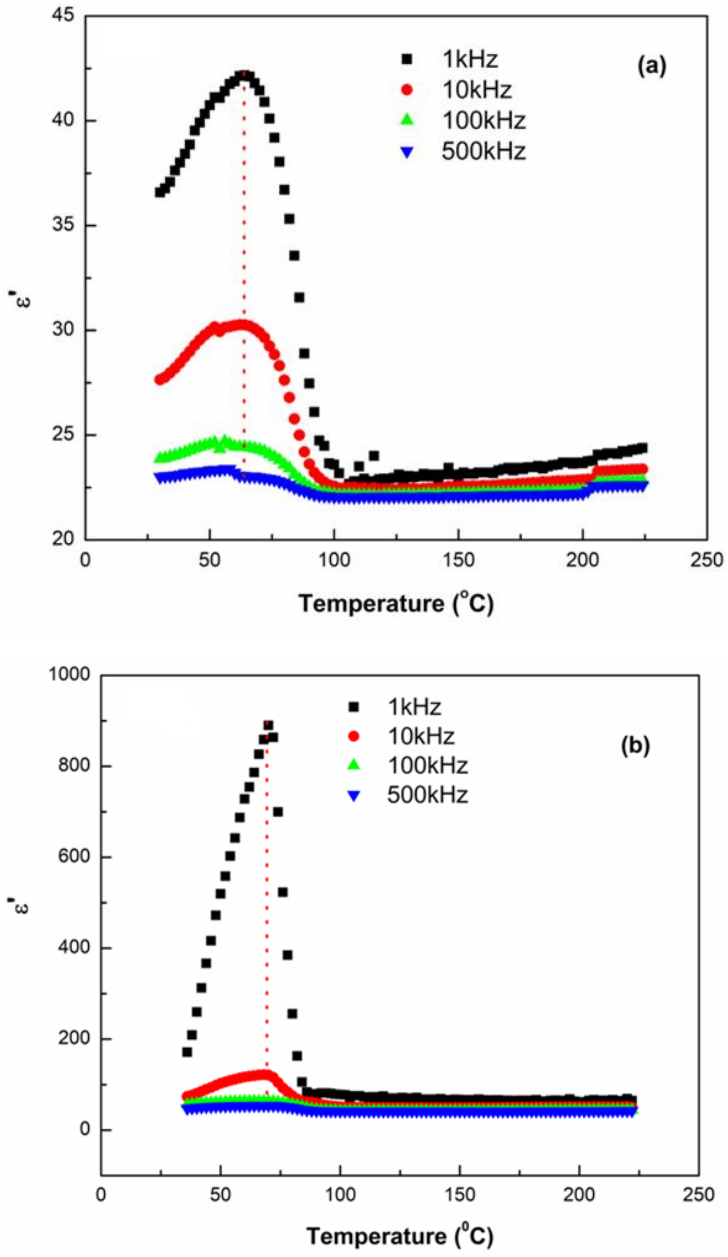

Fig. 5.7. Temperature dependence of dielectric constant ε' at different frequencies (1kHz, 10kHz, 100kHz, 500kHz) for 1000^oC sintered samples (a) S0H and (b) S3H

Electrical properties of wolframite ABO_4 type materials are closely related to crystal structure and oxygen vacancies[20], which can be controlled by the sintering process. The dielectric constant value along with relaxor behaviour might have diminished due to the reduction in the concentration of oxygen vacancies by sintering the sample at higher (1000^0C) temperature. Similar behaviour was reported earlier for Er_2O_3 nanoparticles embedded in SiO_2 glass matrix [21]. So all these experimental results suggest that the reduction of oxygen vacancies are also one of the reasons for reduction in dielectric constant and relaxor like nature of the samples sintered at 1000^0C as compared to 600^0C sintered samples.

In normal ferroelectrics, Curie-Weis law is applicable after the transition temperature but in the relaxor ferroelectrics this is not the case the Curie –Weiss law is not applicable around T_m [18]. The supportive information's for relaxor like nature of the samples are done through Vogel-Fulcher law analysis and ferroelectric nature by P-E (polarization –electric field) loop measurements.

The temperature variation of $1/\ \varepsilon'$ at different frequencies is also important for materials showing relaxor behaviour. Fig. 5.8(a) and 5.8(b) show this kind of behaviour for the S0 and S3 samples. Three regions are observed. The first region is related to the ferroelectric phase up to the transition temperature T_m; the second one is $T_m < T < T_C$ and the third one above T_C (the temperature where it begins to obey the Curie–Weiss law) shows the Curie – Weiss law behaviour. By extrapolating the linear portion of the third region on the temperature axis, T_C can be obtained[22]. Relaxor like behaviour is also described as a combination of randomly interacting polar nanoregions (PNR's) contained in the polarizable medium. The formation of polar nanoregions at a temperature so-called a Burns temperature (T_B), similar behaviour was observed for other samples and their T_m, T_C and T_B values are given in Table. 5.3.

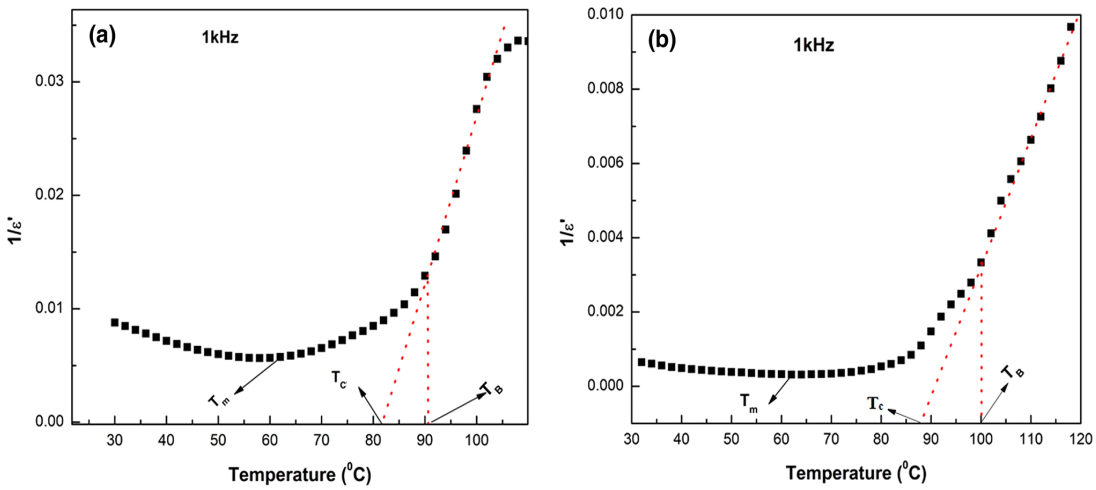

Fig. 5.8. Inverse dielectric constant vs temperature curve at 1kHz for (a) S0 and (b) S3 samples

Table. 5.3 Dielectric constant ε' and relaxor parameters of $CoWO_4$ and $CoWO_4/PbWO_4$ nanocomposites

Samples	T_m at 1kHz(^{0}C)	T_C (^{0}C)	T_B (^{0}C)
S0	58	88	90
S1	72	87	100.5
S2	77	97	103
S3	63	88	100
S4	74	89	94

Modified Curie –Weiss law can be used to check the temperature dependence of ε' near the diffuse phase transition in relaxor ferroelectrics[23]. The following is the modified curie – Weiss law equation

$$1/\varepsilon' - 1/\varepsilon'_m = (T-T_m)^{\gamma}/C \qquad (5.2)$$

where ε' and ε'_m dielectric constants at temperatures T and T_m respectively, C is the modified Curie like constant and γ is a measure of diffusion factor which indicates the diffusion level. The value of γ can be between 1 and 2. For normal ferroelectrics γ =1, for a diffuse phase transition is close to 2 and for a relaxor ferroelectrics equal to 2 [24].

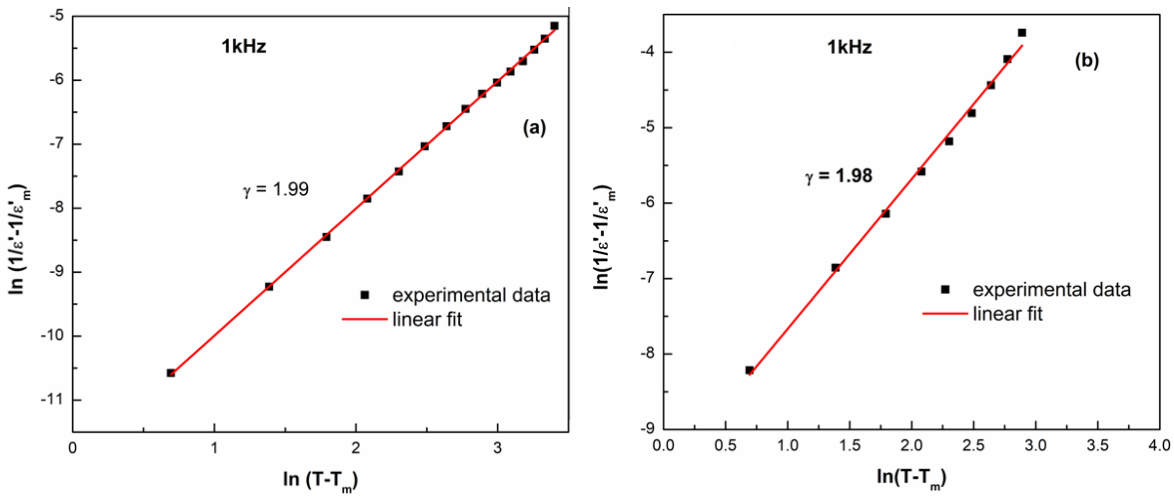

Fig. 5.9. Modified Curie Weiss law: plot of ln ($1/\varepsilon' - 1/\varepsilon'_m$) vs ln ($T-T_m$) of (a) S0 and (b) S3 samples for 1 kHz.

The modified Curie - Wies plot of $\boldsymbol{ln(1/\varepsilon' - 1/\varepsilon'_m)}$ as a function of $\boldsymbol{\gamma\ ln(T-T_m)}$ at 1kHz frequency for S0 and S3 samples is shown in Fig. 5.9(a) and 5.9(b) respectively. From the slope of the linear fit of the curve, we estimated the diffuseness factor value γ to be 1.99and 1.98 for S0 and S3 samples respectively, which follow the diffuse phase transition behaviour.

In relaxor ferroelectrics, the frequency dependence of T_m is found to obey Vogel- Fulcher law

$$f = f_0 exp[-E_a /K_B (T_m - T_f)] \qquad (5.3)$$

where E_a and f_o are the activation energy and the attempt frequency of the dipole reorientation respectively, and T_f is the freezing temperature of the polarization fluctuations [25].

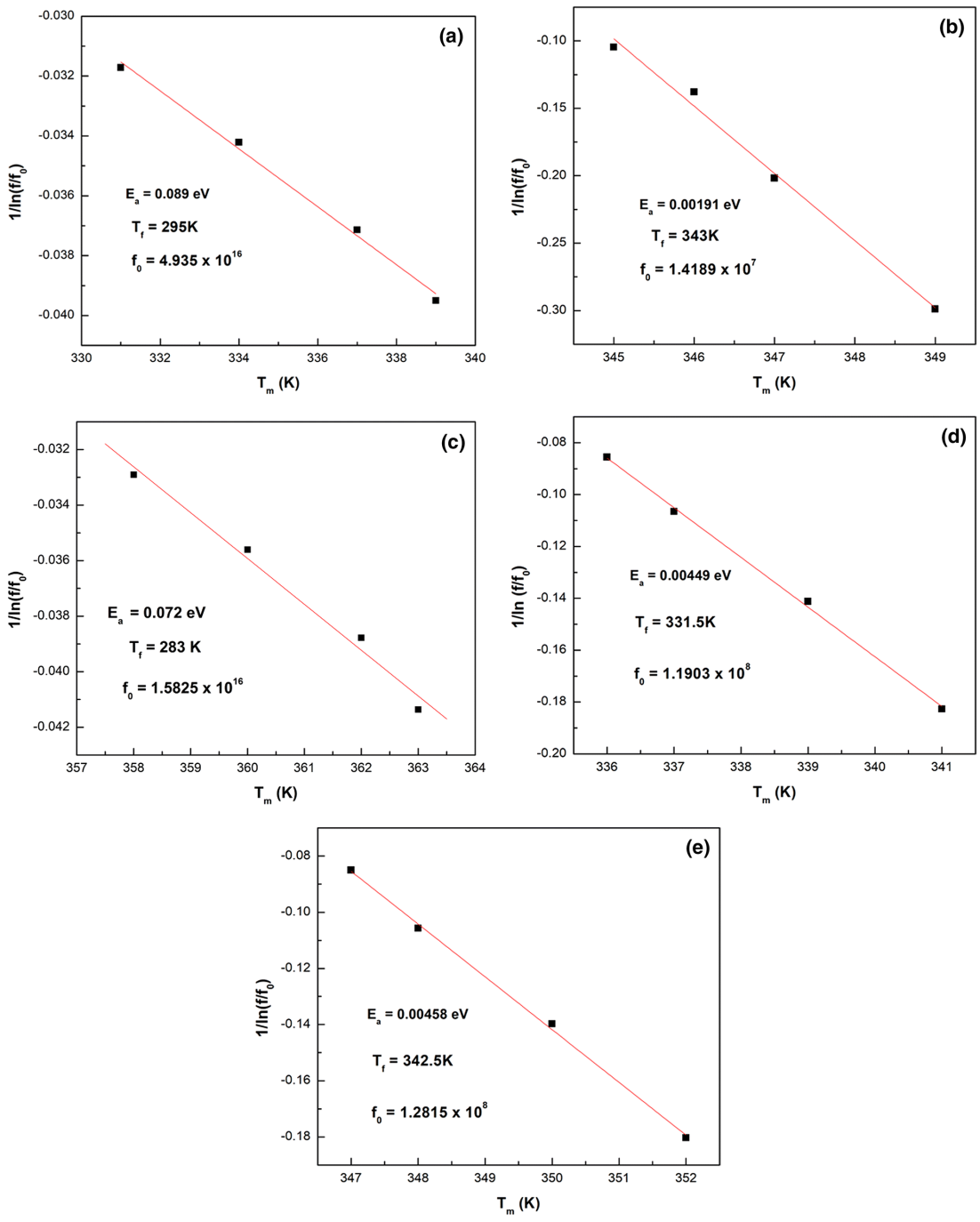

Fig. 5.10. Vogel–Fulcher fitting of $1/\ln(f/f_0)$ as a function of T_m for all the samples: (a)S0, (b)S1, (c)S2, (d) S3, (e) S4.

Fig 5.10(a-d) show the variation of $1/ln(f/f_0)$ as a function of T_m for all the samples, the experimental data represented by a dark square symbol and Vogel Fulcher fit by the solid line (red). It is seen that the T_m shows a good fit to the Vogel–Fulcher law, showing relaxor behaviour of all the samples.

A Vogel-Fulcher equation fit of dielectric constant data measured for frequencies ranging between 1kHz and 500 kHz correlates with the predicted linear relation between the reduced frequency $[\ln(f/f_o)]^{-1}$ and T_m. Inserting a reasonable value for the attempt frequency (f_o) yields the static freezing temperature (T_f) and activation energy (E_a) respectively. The evaluated parameters are tabulated in Table. 5.4.

Table. 5. 4 Vogel-Fulcher law fitting parameters

Samples	T_f (K)	f_0 (Hz)	E_a (eV)
S0	298.2	4.935×10^{16}	0.089
S1	343	1.4189×10^{7}	0.0019
S2	283	1.5825×10^{16}	0.072
S3	331.4	1.1903×10^{8}	0.0045
S4	342.4	1.2815×10^{8}	0.0045

5.2.3. AC Conductivity analysis

In order to understand the transport mechanism of $CoWO_4$ and $CoWO_4/PbWO_4$ nanocomposite samples, we investigated the temperature and frequency dependent AC conductivity $\sigma_{ac}(\omega, T)$. AC conductivity $\sigma_{ac}(\omega, T)$ of the samples were calculated using the equation [26]

$$\sigma(\omega, T) = \varepsilon_0 \varepsilon' \omega \tan\delta \qquad (5.4)$$

where σ is the AC conductivity, ε_0 is the vacuum dielectric permittivity and its value is $8.854\,187\,817 \times 10^{-12}\ F \cdot m^{-1}$, ε' is the real part of the dielectric permittivity, $\tan\delta$ is the dielectric loss, ω is the angular frequency and T is absolute temperature.

5.2.3.1. Frequency dependent AC conductivity

Fig. 5.11 shows the frequency dependence AC conductivity of $CoWO_4$ and $CoWO_4/PbWO_4$ nanocomposites at RT. It is found that there is a frequency independent plateau at lower frequencies due to the polarization effect of electrodes and a dispersive region at higher frequencies [27]. The frequency independent AC conductivity at low frequency region corresponds to DC conductivity. The frequency-dependent conductivity obeys the Jonscher power law [28] which is described below

$$\sigma_{ac} = \sigma_{dc}(T) + A\omega^n \qquad (5.5)$$

Where σ_{ac} represents the AC conductivity, $\sigma_{dc}$is the DC conductivity (frequency independent plateau in the low-frequency region), **A** is the pre-exponential factor and '**n**' is the frequency exponent. The first term is temperature dependent and independent of frequency variation due to the drift mobility of charge carriers. The second term is related to dielectric relaxation due to the localized charge carriers. The obtained results are plotted as $\sigma_{ac}(\omega)$ versus radial frequencies at room temperature (Fig.5.11.). Frequency dependence σ_{ac} follows a power law ω^n, where the exponent n depends on the nature of the polarization process. The frequency at which relaxation effects begin to appear is called hopping frequency [29,30]. The DC conductivity (σ_{dc}), frequency exponent (n) and pre-exponent factor (A) are determined from the Jonscher power law fitting as shown in Fig. 5.11 as a solid line. Using these parameters, the hopping frequency (ω_p) was calculated from the following formula [29] and are tabulated in Table 5.5.

$$\omega_p = \left[\frac{\sigma_{dc}}{A}\right]^{\frac{1}{n}} \qquad (5.6)$$

$$N = \frac{\sigma_{dc} k_B T}{e^2 a^2 \gamma \omega_p} \qquad (5.7)$$

$$\mu = \frac{\sigma_{dc}}{Ne} \qquad (5.8)$$

where, k_B is the Boltzmann constant, e is the charge of an electron, a is the hopping distance (taken as 3 Å) and the geometrical factor, γ is set equal to 1/6 for isotropic materials [29,31].

DC conductivity at RT is higher for nanocomposites as compared to the bare $CoWO_4$ and it is maximum for S3 sample with 6.7 times higher than that of S0 sample. This may be due to the space charge layer (SCL) formation at the interface for the nanocomposites. When two oxides with different structures form an interface (with structural discontinuity), charge redistribution of ionic and electronic defects takes place [32–34]. In tungstates, oxygen vacancies are the major defects[35]. In our composite samples, oxygen vacancies and Co^{3+}ions defects get accumulated at the interface, creating a positive charge core. This is compensated electrostatically by the creation of electron polarons around the positive ions adjacent to the interface forming the space charge layer [SCL] and screening the oxygen vacancies. This SCL formation results in an additional electronic conductivity which increases the total conductivity and decreases the activation energy.

Frequency dependent AC conductivity can be described using the jump relaxation model. According to jump relaxation model [36] at low frequencies, the charge carriersjump from their lattice site to the adjacent site through pairwise hopping. Associated with the hopping of ions is also rearrangement of ions at lattice sites. At high frequencies there is dispersion in conductivity due to forward-backwards hopping along with the rearrangement of ions, termed site relaxation. The physical meaning of the frequency exponent (n) is related to the backward hopping time and the site relaxation time **as** given by

$$n = \frac{backward\ hopping\ time}{siterelaxationtime} \qquad (5.9)$$

In most cases, n is found to be between 0.6 and 1 for ionic conduction[14]. The value of n = 1 is regarded theoretically as the limiting value. The case of n > 1 has been reported in a few compositions of crystalline, semiconductors and glasses[3,29]. If $n \leq 1$, the hopping motion is translational meanwhile if n> 1, the hopping motion would be localized. For our nanocomposite samples S1, S3, S4 have the value of n < 1 and among them, the S3 sample has the lowest n value. The S0 sample ($CoWO_4$) has the value of n> 1 may be due to the backward hopping rate of charge carriers being faster than the site relaxation time.

The pre exponential factor (A) is also called as a dispersion factor which represents the strength of polarizability of the samples[37]. Hopping frequency of the nanocomposites is

lower than that of the bare $CoWO_4$ sample. This may be due to the presence of more grain boundaries in nanocomposites. Generally, agglomeration of the nanoparticles can create more grain boundaries and increase the charge carriers' relaxation time at low frequency [38–40] and thus the nanocomposites have lower hopping frequency. Agglomeration of these nanocomposites was briefly discussed in our chapter 3. Another reason for nanocomposites having lower hopping frequency is that particles agglomeration is the reason for SCL formation in the nanocomposites samples which increases conductivity of composites even at lower frequency [41]. Hence hopping frequency of the nanocomposites is lower than that of the bare $CoWO_4$.

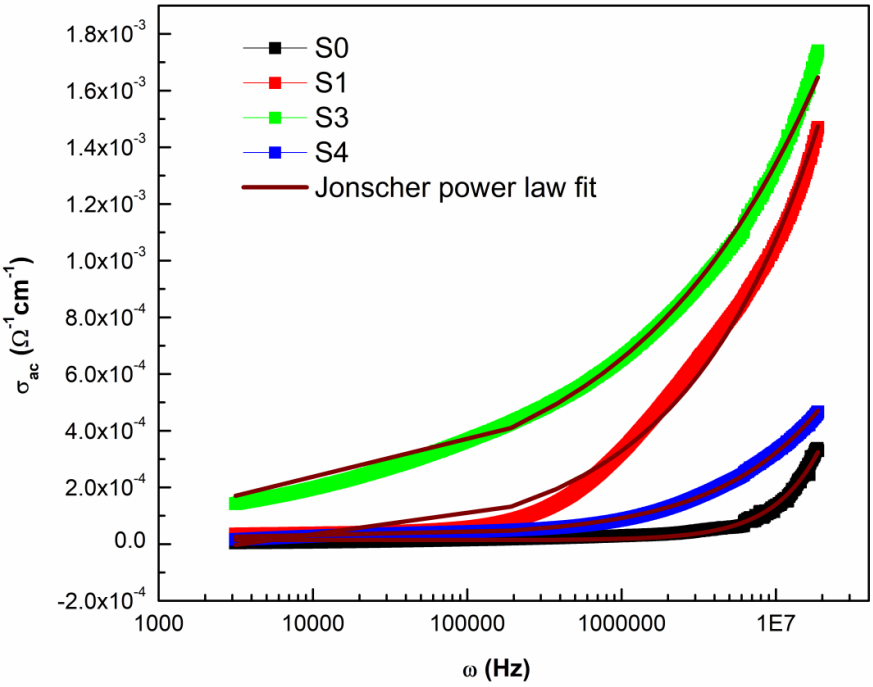

Fig. 5.11. Variation of AC conductivity with angular frequency at RT. The solid line in the figure represents Jonscher power law fit

Table .5.5 The parameters obtained from the Jonscher power law fitting.

Samples	σ_{dc} ($\Omega^{-1}cm^{-1}$)	(n)	A	(ω_p) Hz
S0	1.42×10^{-5}	1.4	1.06×10^{-14}	3.29×10^{6}
S1	2.40×10^{-5}	0.49	3.84×10^{-7}	4.63×10^{3}
S3	9.50×10^{-5}	0.34	4.55×10^{-6}	7.62×10^{3}
S4	2.38×10^{-5}	0.64	9.66×10^{-9}	1.99×10^{5}

5.2.3.2. Conduction mechanism analysis

There are many models approached for conduction mechanism of ternary oxides like ferrites, tungstates, titanates, perovskites. From the previous studies, if n decreases with increasing temperature, the correlated barrier hopping (CBH) model is applicable for the conduction mechanism. In this model, conduction is due to hopping of charge carriers [42]. According to the overlapping-large polaron tunneling (OLPT) model, n is both frequency and temperature dependent and n decreases with increasing temperature to a minimum value and then continues to increase with increasing temperature. In quantum mechanical tunneling (QMT) model, the value of n ~ 0.8 and is temperature independent [43]. In the case of nonoverlapping small polaron tunneling (NSPT) model, the frequency exponent n increases with increasing temperature. In this model, small polarons are formed when charge carriers interact with the surrounding lattice and a tunneling process is responsible for conductivity [44]. To find the conduction mechanism model for $CoWO_4$ and $CoWO_4/PbWO_4$ nanocomposites, the frequency dependence of conductivity at different temperatures have been plotted shown in Fig. 5.12 and frequency exponent ‘n’ for different temperatures has been calculated by power law fitting.

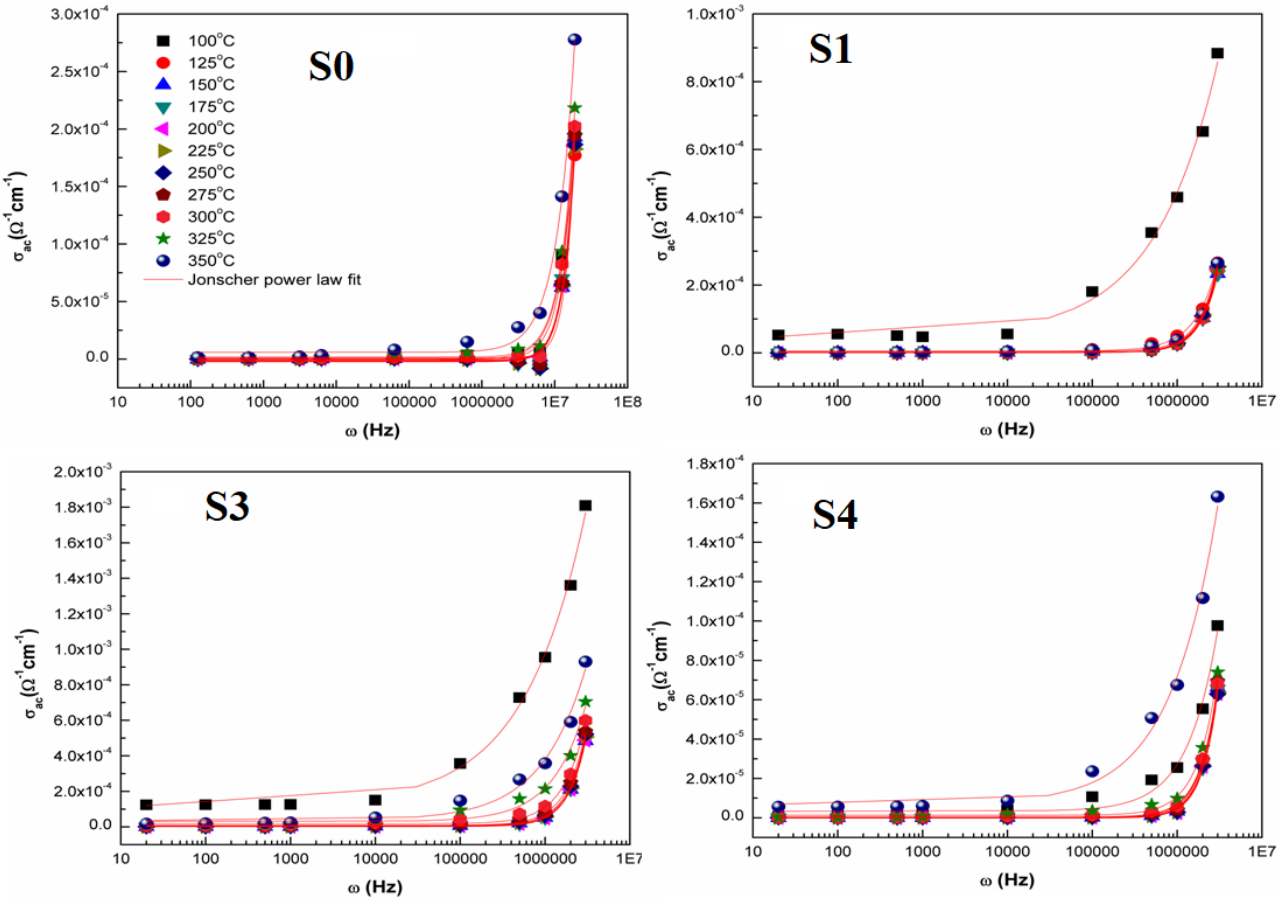

Fig. 5.12.Frequency dependent AC conductivity at different temperatures. The solid red line in the figures represents Jonscher power law fit

Fig. 5.13 shows the variation of n with increasing temperature for $CoWO_4$ and $CoWO_4/PbWO_4$ nanocomposites. These three regions of observation demonstrate that small polaron tunneling (NSPT) is an appropriate model for electrical conduction in the first region, whereas the correlated barrier hopping (CBH) model along with NSPT model is most suitable for the second region. Pure NSPT model is the suitable conduction mechanism in region 3.

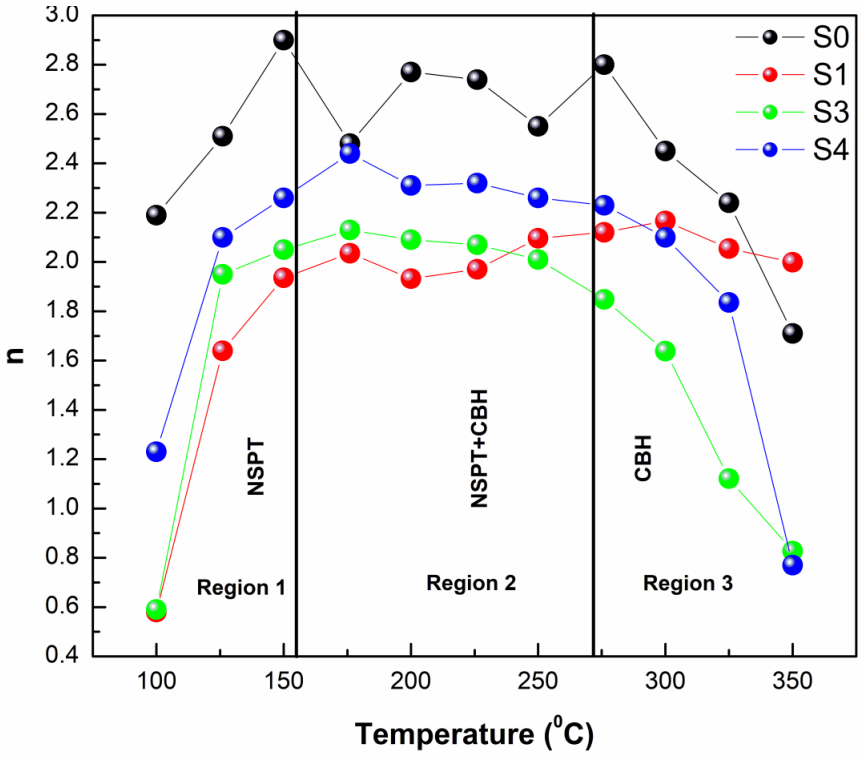

Fig. 5.13. Variations in n (obtained through Jonscher "power law fitting") with temperature for $CoWO_4$ and $CoWO_4/PbWO_4$ nanocomposites.

According to CBH and NSPT model the frequency exponent n can be calculated by the following equations (5.10) and (5.11) respectively[42]

$$n = 1 - \frac{6k_BT}{W_H - k_BTln(1/\omega\tau_0)} \qquad (5.10)$$

$$n = 1 - \frac{4}{ln(1/\omega\tau_0) - \frac{W_H}{k_BT}} \qquad (5.11)$$

where k_B is the Boltzmann constant, T is the absolute temperature, $W_H$is the hopping energy, ω is the angular frequency and τ_0 is the characteristic relaxation time, which is in the order of atom vibrational period $\tau_0 = 10^{-13}$s. For large values of W_H/k_BT, the exponent n becomes expressed by

$$n = 1 - \frac{6k_BT}{W_H} \qquad (5.12)$$

$$n = 1 + \frac{4k_BT}{W_H} \qquad (5.13)$$

W_H is the hopping energy is defined as the energy required to hopping an electron completely from one site to another site. Values of W_H are calculated using equation (5.12) and equation (5.13) for the pure NSPT and pure CBH model in the region 1 and region 3 respectively. Variation of 1-n with increasing temperature is shown in Fig. 5.14. From the slopes of the region 1 and region 3 (Fig. 5.14), the value of W_H has been calculated and is given in Table 5.6.

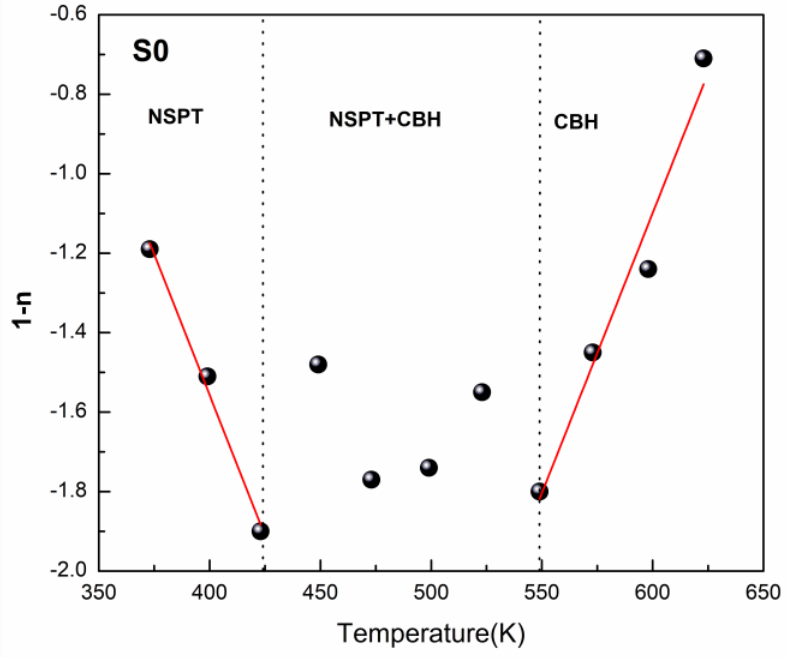

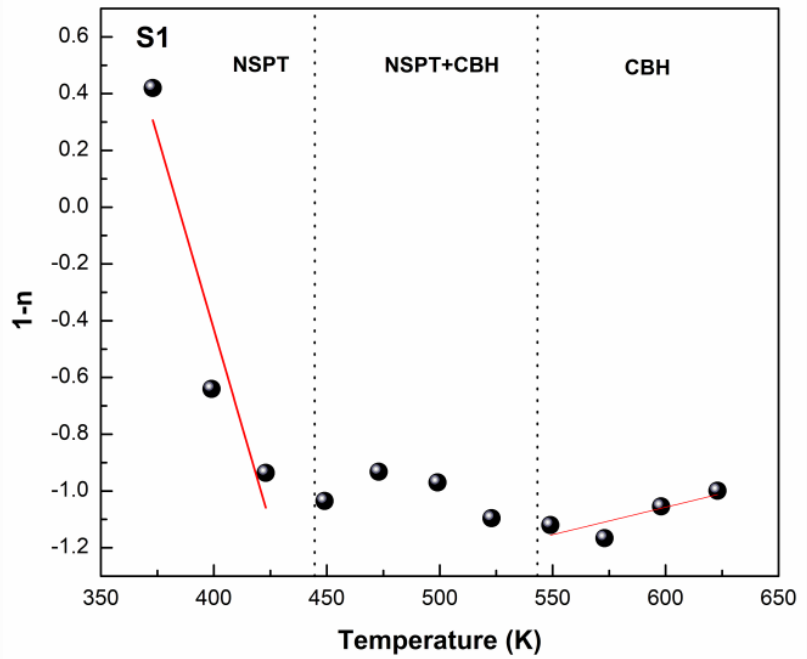
S1
NSPT
NSPT+CBH
CBH
1-n
Temperature (K)
0.6
0.4
0.2
0.0
-0.2
-0.4
-0.6
-0.8
-1.0
-1.2
350
400
450
500
550
600
650

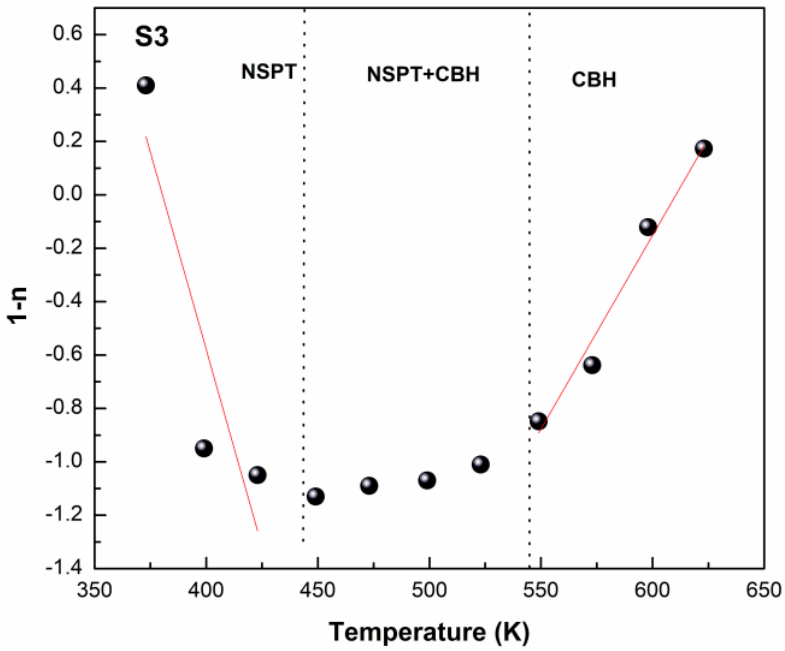
S3
NSPT
NSPT+CBH
CBH
1-n
Temperature (K)
0.6
0.4
0.2
0.0
-0.2
-0.4
-0.6
-0.8
-1.0
-1.2
-1.4
350
400
450
500
550
600
650

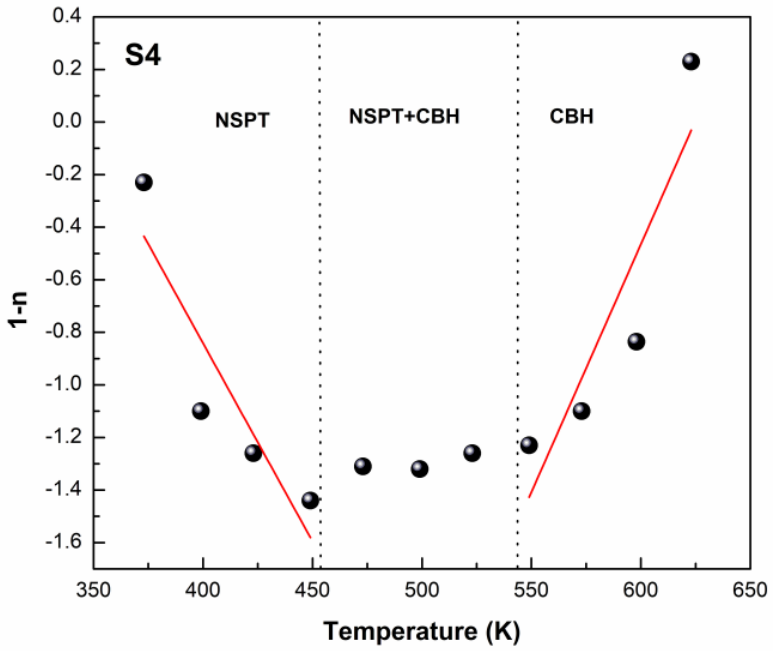

Fig. 5.14. Variation of 1-n with increasing temperature for $CoWO_4$ and $CoWO_4/PbWO_4$ samples

Table. 5.6 Values of hopping energy for pure NSPT and CBH region in $CoWO_4$ and $CoWO_4/PbWO_4$ nanocomposites

Samples	Hopping energy W_H (eV)	
	Region 1 (pure NSPT model)	Region 3 (pure CBH model)
S0	0.024	0.036
S1	0.012	0.154
S3	0.011	0.035
S4	0.023	0.027

Hopping energy values for the S1 and S3 samples from the NSPT model are lower than that of the values for the bare $CoWO_4$ (S0) sample and S4 sample. This is because when the space charge layer (SCL) is formed, the polaron tunneling is easier and the required energy to tunnel from one site to another site is less.

5.2.3.3. Temperature dependent AC conductivity

Fig. 5.15(a-d) shows the variation of AC conductivity with temperature for all the samples at different frequencies. AC conductivity increases with increasing temperature according to the Arrhenius equation which is given below

$$\sigma = \sigma_{a1} exp(-E_{a1}/k_B T) + \sigma_{a2} exp(-E_{a2}/k_B T) \qquad (5.14)$$

The two terms arise from two different conduction mechanisms. The first and second term of equation (5.14) describes the first and second intrinsic region at high temperature. E_{a1} and E_{a2} are the activation energies for first (570K-623K) and second (520K–570K) intrinsic conductivity respectively, k_B is the Boltzmann constant and T is the absolute temperature. The different slopes in these conductivity regions correspond to different activation energies. Activation energies were determined from the linear fitting of the intrinsic conductivity regions on the basis of Arrhenius law. The activation energies (E_{a1} *and* E_{a2}) of nanocomposites samples at 1 kHz, 10 kHz, 100 kHz, and 500 kHz are given in Table 5.7. Calculated activation energies for different frequencies do not follow any linear tendency. But only at 1kHz, the S3 sample has the lowest values of E_{a1} and E_{a2} as compared to other samples. This may be due to the formation of SCL with charge accumulation at the interface for 1kHz. This leads to higher conduction and lower activation energy [32].

The temperature dependent AC conductivity obeys Mott's theory of conduction, according to which the distance between the adjacent correspondent sites is much smaller than the hopping range [45]. D. Atler et al. reported that electrical transport of transition metal tungstates is typically characterized by a d-band near the Fermi level [46]. There are two conduction processes involved in $CoWO_4$ nanomaterials. One is due to the hopping of charge carriers (holes) in the narrow $3d^9$ band which will dominate at a lower temperature and another is a normal band like conduction in the 2p band at a higher temperature. At low temperature, the charge carrier (hole) mobility of the $CoWO_4$ is very low due to the narrowness of the d band leading to the formation of hole polarons. The transfer of an electron from one Co^{2+} ion to the adjacent Co^{2+} ion will lead to the formation of Co^{3+} ion [47].

$$Co^{2+} - e^- \leftrightarrow Co^{3+}$$

When the temperature is increased to high value the hopping conduction in narrow $3d^9$ bands is suppressed by the oxygen 2p band. [29]. Enhanced AC conductivity was observed for S3

sample as compared to other samples at all the frequencies. This may be due to the space charge layer (SCL) formation at the interface.

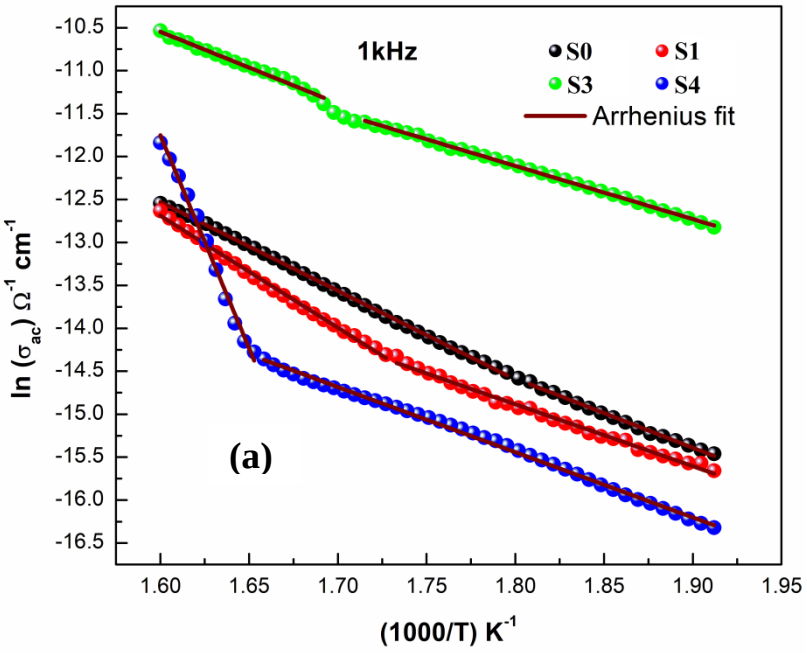

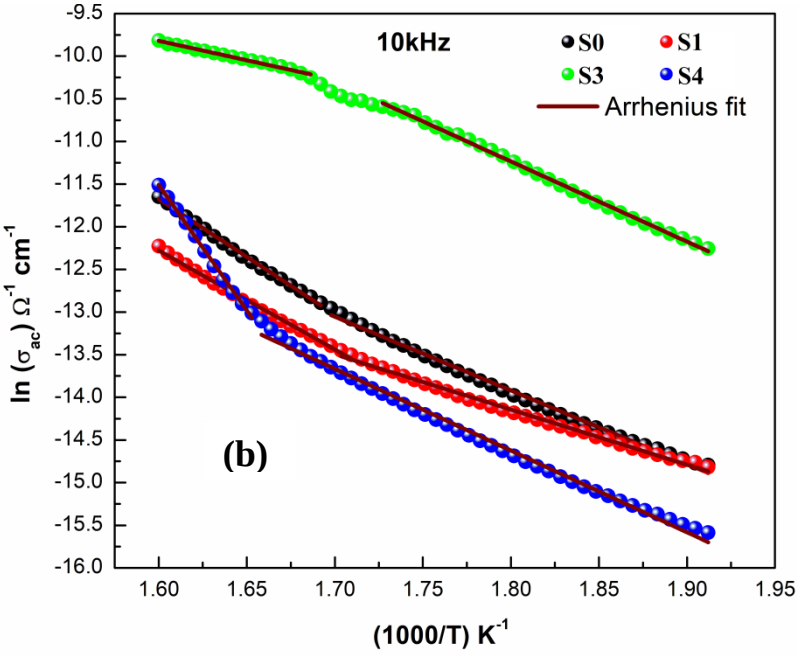

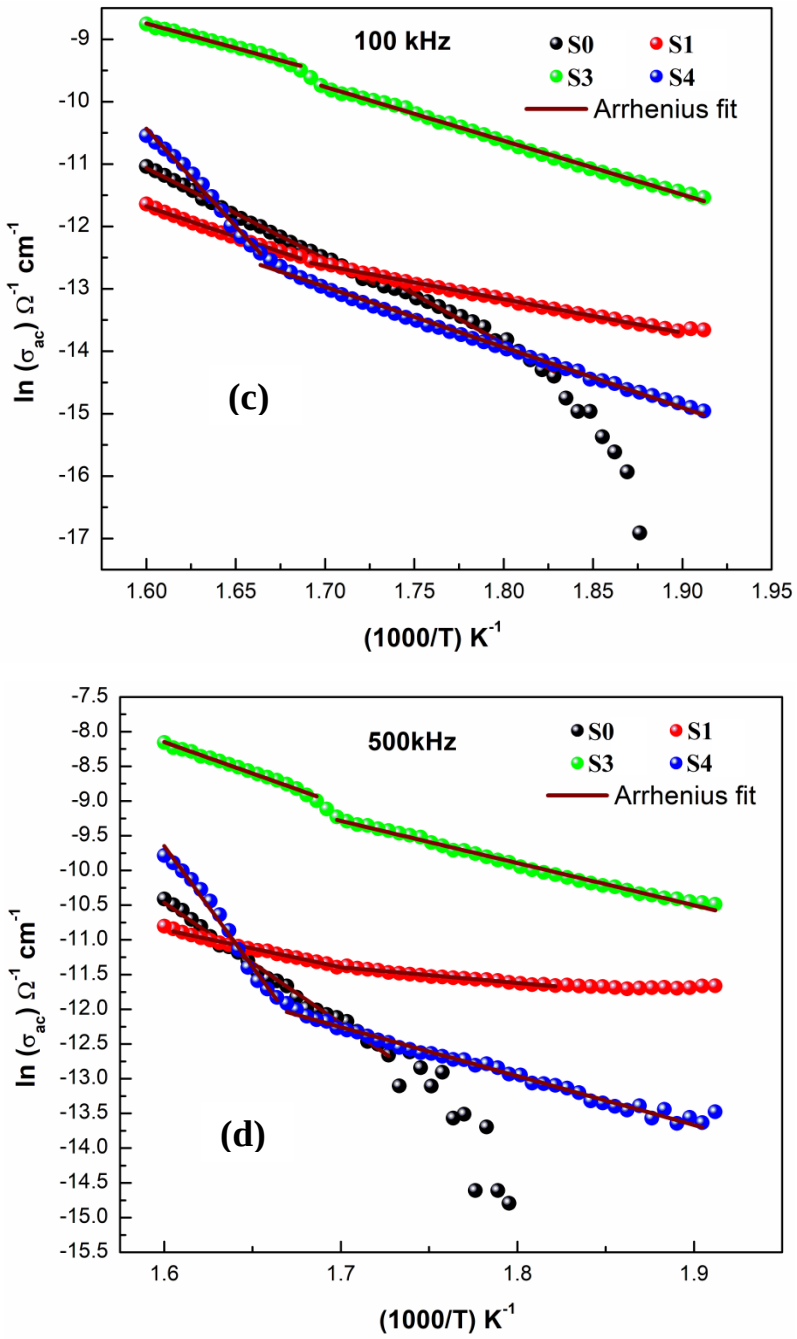

Fig. 5.15. Variation of AC conductivity with temperature for all the samples at different frequencies: (a) 1kHz (b) 10kHz (c) 100kHz (d) 500kHz. The solid line represents the Arrhenius fit.

Table.5.7 The activation energy for the AC conductivity of the samples at 1 kHz, 10 kHz, 100 kHz, 500 kHz. E_{a1} and E_{a2} represent the activation energies of the samples calculated for the temperature region of 570K-623K and 520K – 570K respectively.

Samples	Activation energy (eV)							
	1kHz		10kHz		100kHz		500kHz	
	E_{a1}	E_{a2}	E_{a1}	E_{a2}	E_{a1}	E_{a2}	E_{a1}	E_{a2}
S0	0.89±0.01	0.69±0.01	1.16±0.01	0.74±0.01	1.25±0.01	1.36±0.01	1.49±0.01	
S1	1.12±0.01	0.62±0.01	0.99±0.01	0.55±0.01	0.83±0.01	0.46±0.01	0.46±0.01	0.19±0.01
S3	0.71±0.02	0.53±0.01	0.39±0.01	0.81±0.01	0.67±0.02	0.74±0.01	0.78±0.02	0.52±0.01
S4	2.27±0.12	0.65±0.01	2.53±0.10	0.82±0.01	2.69±0.10	0.83±0.01	2.99±0.12	0.60±0.01

5. 2.4. DC conductivity analysis

Fig. 5.17 shows the variation of the DC conductivity with the reciprocal of absolute temperature (measured while cooling) in the range of 350K – 770K for $CoWO_4$ and $CoWO_4/PbWO_4$ nanocomposites samples. Three regimes of conductivity behaviour have existed; the extrinsic regime has occurred in the temperature range of 350K to 398K and above the 398K all the samples show the intrinsic region with different activation energies. DC conductivity behaviour is the same for all the samples similar to that of bulk oxides semiconductors reported by others [48,49]. Conductivity (σ_{dc}) in the extrinsic region (350K-398K) of samples was found to increase slowly with increase in temperature revealing the semiconducting nature of the samples. This may be due to the variable range hopping of the charge carriers in the localized states which are estimated by Mott's variable range hopping model [47,48]. In this temperature region, the number of charge carriers (holes) due to intrinsic defects was not sufficient and the charge carriers in the conduction band are very few to give rise to considerable conduction. The sharper increase in the intrinsic region with different slopes may be due to thermally assisted tunnelling of charge carriers and thermal excitation of charge carriers from grain boundaries.

The conductivity of the S3 sample is higher than that of other samples. This can be explained by the space charge layer model (SCL) for interfaces. This SCL formation results in

an additional electronic conductivity which increases the total conductivity and decreases the activation energy.

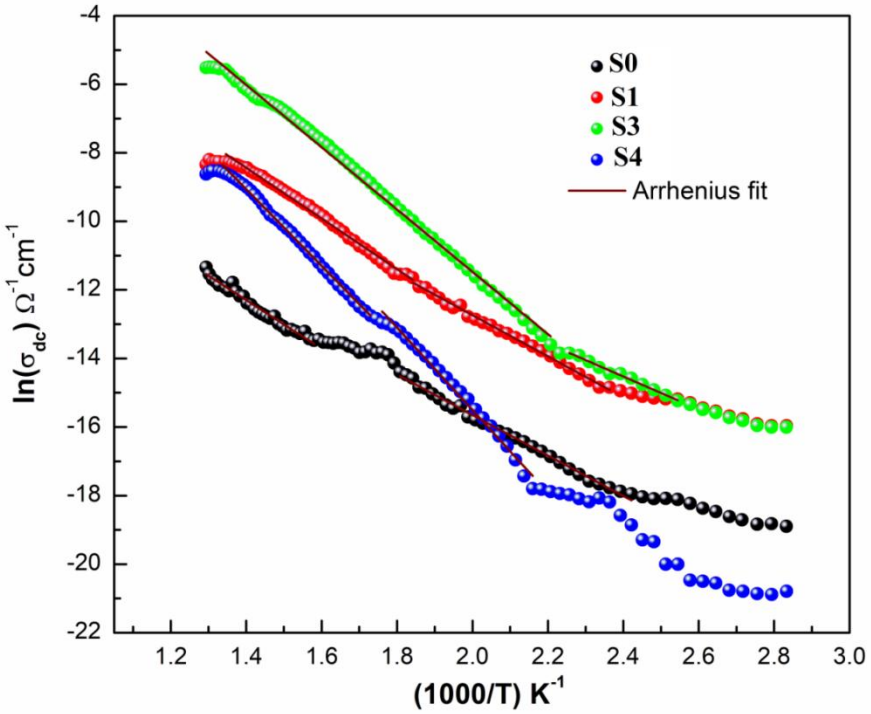

Fig. 5.17. Temperature dependent DC conductivity of the samples. The red solid line represents the Arrhenius fit.

In metal oxides, different conduction mechanisms are responsible for temperature dependent DC conductivity [52,53]. DC conductivity for the intrinsic regions is given by the Arrhenius equation (equation 5.14). Activation energies are calculated from the slopes of the straight lines for the two intrinsic conduction regions and are tabulated in Table 5.8. Activation energy E_{a2} is minimum in the intrinsic region 2 (393-443K) for the S3 sample as compared to other samples. This may be due to the space charge layer (SCL) formation at the interface of the S3 sample.

Table. 5.8. Activation energy for the DC conductivity

Samples	Temperature range of intrinsic regions		Activation energy (eV)	
	Intrinsic region 1 (K)	Intrinsic region 2 (K)	E_{a1} (region1)	E_{a2} (region2)
S0	633-770	413-553	0.61±0.02	0.50±0.01
S1	543-770	422-537	0.63±0.01	0.51±0.01
S3	448-770	393-443	0.78±0.01	0.41±0.01
S4	572-770	468-563	0.96±0.02	1.03±0.01

5.2.5. P-E Hysteresis

The ferroelectric nature of the $CoWO_4$ and $CoWO_4/PbWO_4$ nanocomposites is analyzed by P-E hysteresis loop measurement. Fig. 5.18 shows ferroelectric hysteresis loops (P-E loops) recorded at RT for S0 and S3 samples. Non-ideal hysteresis P-E loop is observed due to relatively high leakage caused by the existence of oxygen vacancies. The remanent polarization of S0 and S3 samples were found to be 0.314 μC .cm^{-2} and 0.492 μC .cm^{-2} respectively. The observed value of remanent polarization for S0 is lower than that of S3. The coercivity of S0 and S3 were found to be 10.76 Kv/cm and 13.56 Kv/cm respectively. The saturation polarization is not observed for the samples due to the combined effect of capacitor and resistor joint in parallel (lossy capacitor) in the materials. This measurement was done to prove that the prepared samples $CoWO_4$ and composites $CoWO_4/PbWO_4$ exhibit ferroelectric nature at room temperature.

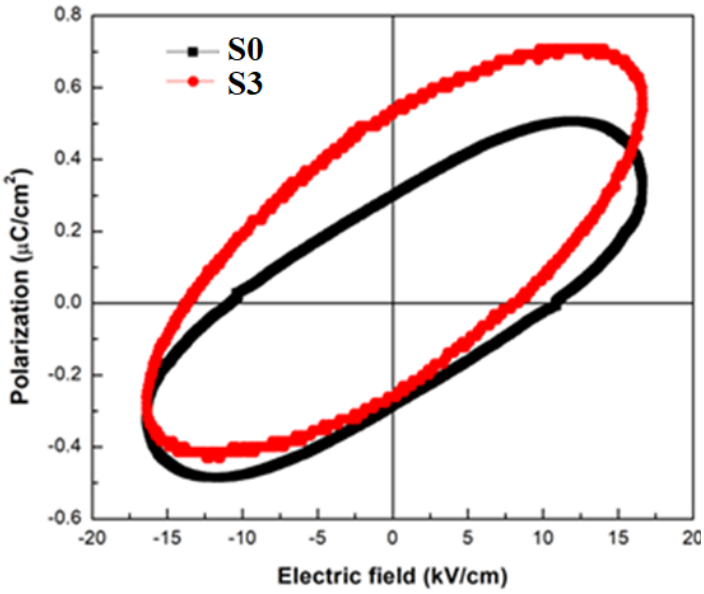

Fig. 5.18. Polarization versus electric field (P-E) hysteresis loop recorded at RT for S0 and S3 samples.

The P-E curve of the S0 sample recorded at different temperature 50^0C (below T_m), 170^0C and 200^0C (above T_m) are shown in Fig. 5.19. Ferroelectric hysteresis observed for all the measured temperature reveals that there is no structural or phase transition above T_m.

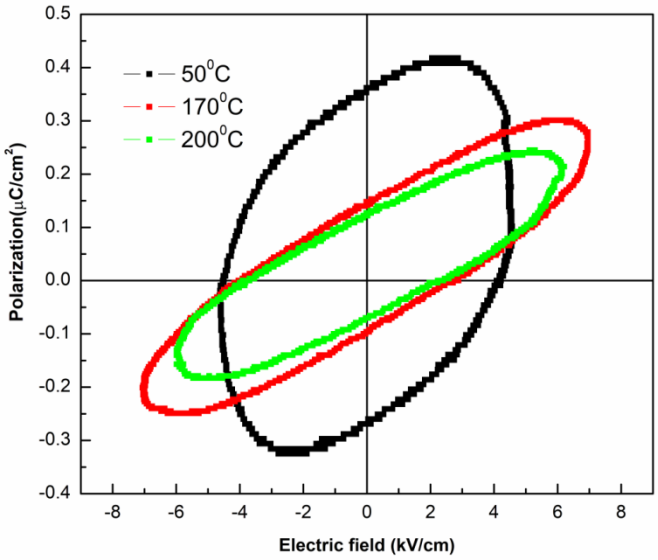

Fig. 5.19. Polarization versus electric field (P-E) hysteresis loop recorded at different temperature for S0 sample

5.2.6. Thermoelectric properties analysis

Seebeck coefficient (S) of the samples at a given temperature is determined by the relation

$$S = - (\Delta V/\Delta T) \qquad (5.15)$$

where ΔV is the measured Seebeck voltage and ΔT is the temperature difference across the junctions (Hot and Cold). Variation of Seebeck coefficient with temperature for all the samples is shown in Fig. 5.20. Seebeck coefficient is positive over the measured temperature range of 400K to 770K, suggesting p-type conduction behaviour [49]. The absolute value of the Seebeck coefficient decreases with increasing temperature. As the temperature increases the charge carriers (holes) gain more energy and scattering of charge carriers will be less consequently Seebeck coefficient decreases. Also, the Seebeck coefficient of S3 sample is higher than that of all other samples. In general, interface acts as a potential barrier in nanocomposites and energy-selective carrier scattering process would filter (scatter back) the electrical carriers whose energy are lower than the barrier height while the carriers whose energy are higher than barrier height can easily pass through an interface [54,55]. This energy-dependent charge scattering leads to an increase in the Seebeck coefficient for composite samples. The optimum barrier height plays an important role in the charge carrier filtering. So S3 sample with optimal interfacing between $CoWO_4$ and $PbWO_4$ phases gives higher Seebeck coefficient than the other samples.

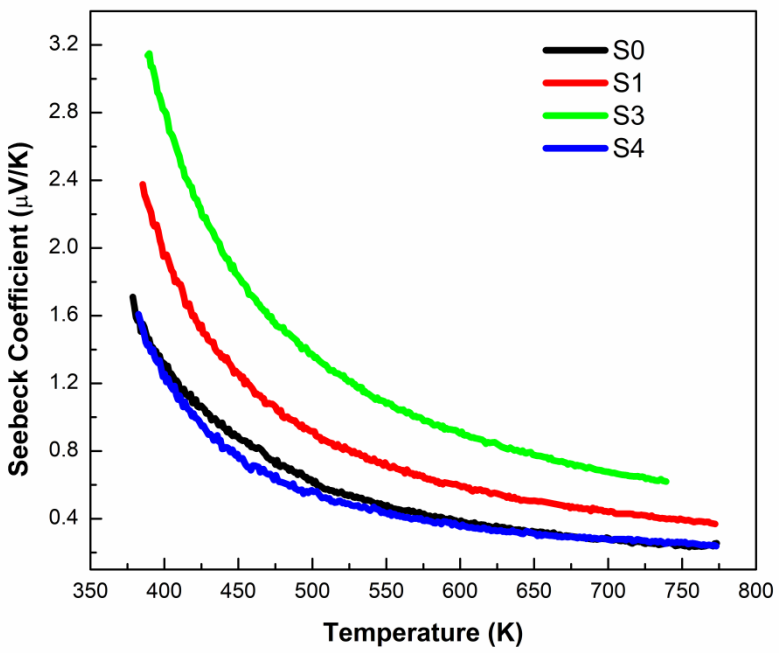

Fig. 5.20. Temperature dependent Seebeck coefficient (S) of the samples.

The carrier concentration of the samples is calculated using the following relations [56].

$$S = \frac{8\pi^2 {k_B}^2}{3eh^2 S} m^* T \left[\frac{\pi}{3n}\right]^{2/3} \qquad (5.16)$$

$$n = \frac{\pi}{3}\left[\frac{8\pi^2 {k_B}^2}{3eh^2 S} m^* T\right]^{3/2} \qquad (5.17)$$

wherem^* and n are the effective mass of the carrier and the carrier concentration respectively. k_B is the Boltzman constant, e is the electronic charge, h is the plank constant, T is the measurement temperature. Variation of carrier concentration with temperature is shown in Fig. 5.21. Carrier concentration increases with increasing temperature. With an increase in temperature more electrons gain enough energy to break the bonds and jump to the conduction band leaving behind holes in the valence band. This leads to an increase in carrier concentration. The order of carrier concentration observed for the samples is between 10^{19} to 10^{21} per cm^3 in the temperature range of 400K to 770K. Carrier concentration is maximum for single-phase $CoWO_4$ (S0) sample and least for interfaced S3 sample. This is because the Seebeck coefficient of S0 sample is lower than that of S3 sample.

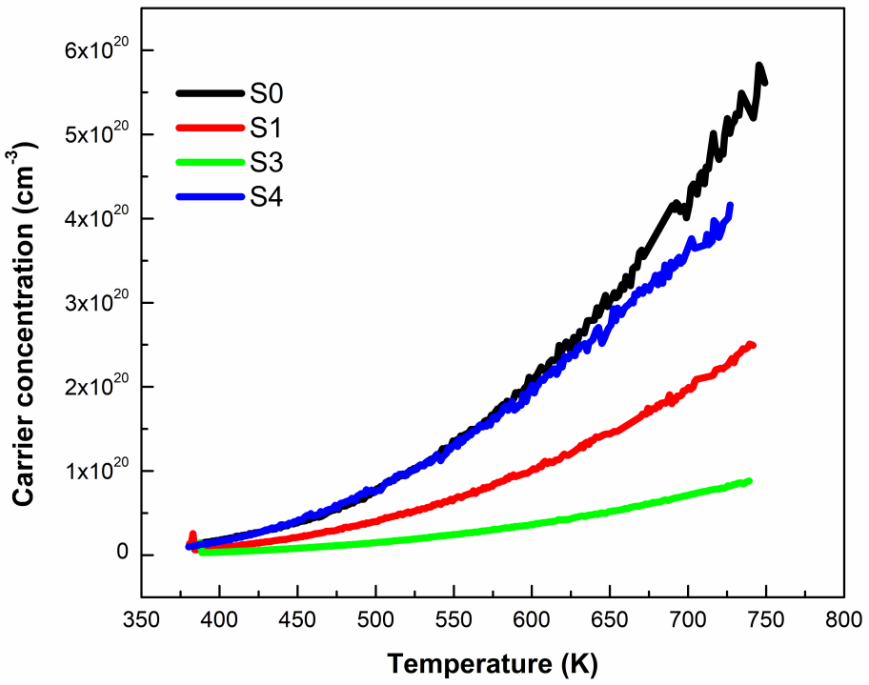

Fig. 5.21. Temperature dependent carrier concentration of the samples.

Thermoelectric (TE) efficiency of a material is described by the dimensionless TE figure-of-merit $ZT = S^2\sigma T/\kappa$, where S is the Seebeck coefficient, σ is the electrical conductivity, T is the absolute temperature and κ is the total thermal conductivity. High TE figure-of-merit may be achieved by reducing κ and/or by enhancing the thermoelectric power factor $P = S^2\sigma$. The power factor of the TE materials plays an important role in TE devices. The temperature dependence of power factor of the samples is shown in Fig.5.22. An enhanced power factor of the nanocomposite samples is due to the interfacial energy barrier scattering. Conductivity, as well as Seebeck coefficient, is maximum for S3 sample. So power factor of the S3 sample is higher than the other samples.

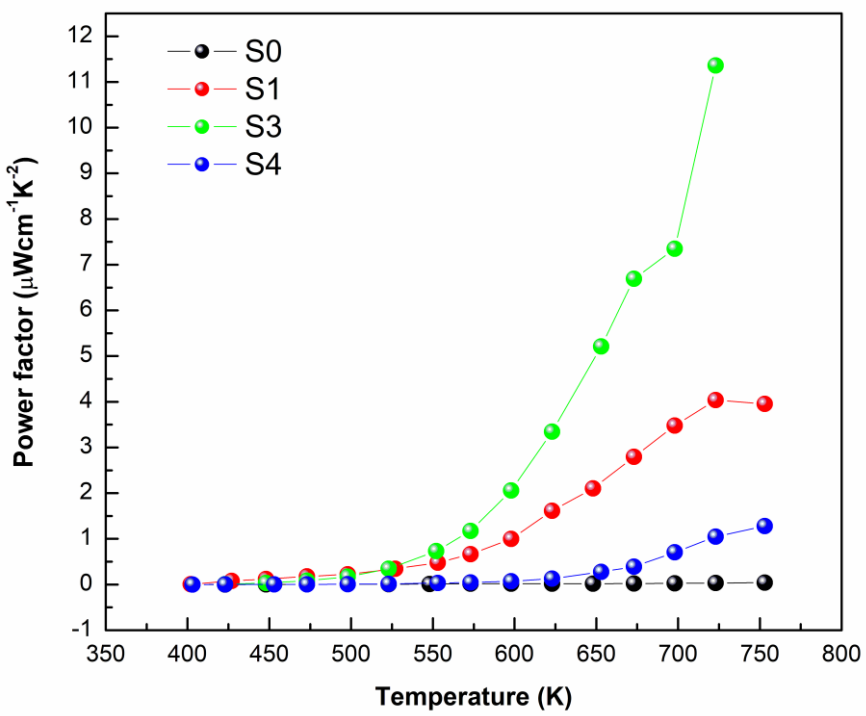

Fig. 5.22. Temperature dependence of power factor of the samples

5.2.7. Magnetic properties of $CoWO_4$ and $CoWO_4/PbWO_4$ nanocomposites

Magnetic properties of $CoWO_4$ and $CoWO_4/PbWO_4$ nanocomposites were studied using vibrating sample magnetometer (VSM). The magnetization of the samples with respect to the applied field measured at RT is shown in Fig. 5.23. In this figure, we could observe the linear response of magnetization with respect to the applied field which shows paramagnetic behaviour of the samples and these results match with earlier reports [29,57–59]. No ferromagnetic ordering was observed at room temperature which confirms the absence of transition metal (Co) based clusters [60]. The $PbWO_4$ embedded in $CoWO_4$ has not altered the magnetic properties of $CoWO_4$ other than the fractional reduction of magnetization in nanocomposites samples.

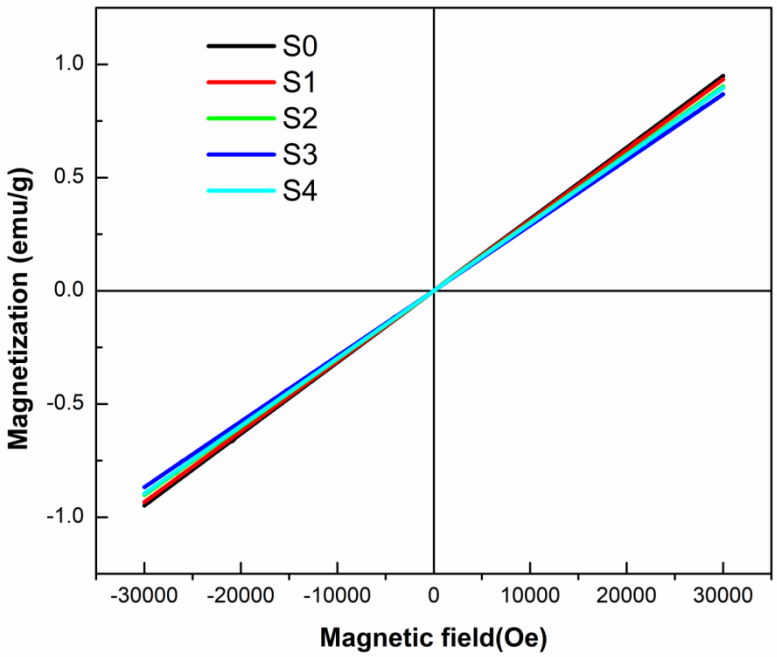

Fig. 5.23. Field dependent magnetization of the $CoWO_4$ and $CoWO_4/PbWO_4$ nanocomposites

Zero-field-cooled (ZFC) and field-cooled (FC) magnetization curves at three different applied fields: 250, 500 and 1000 Oe in the temperature range of 50–400 K for the S0 and S3 samples are shown in Fig. 5.24. There is not much difference between the ZFC and FC curves of DC magnetization. No hysteresis behaviour was detected at any temperature between 50 and 400 K which reveals that no ferromagnetic ordering in this temperature range. These curves do not have any transition peak in this temperature range representing the paramagnetic nature of the samples.

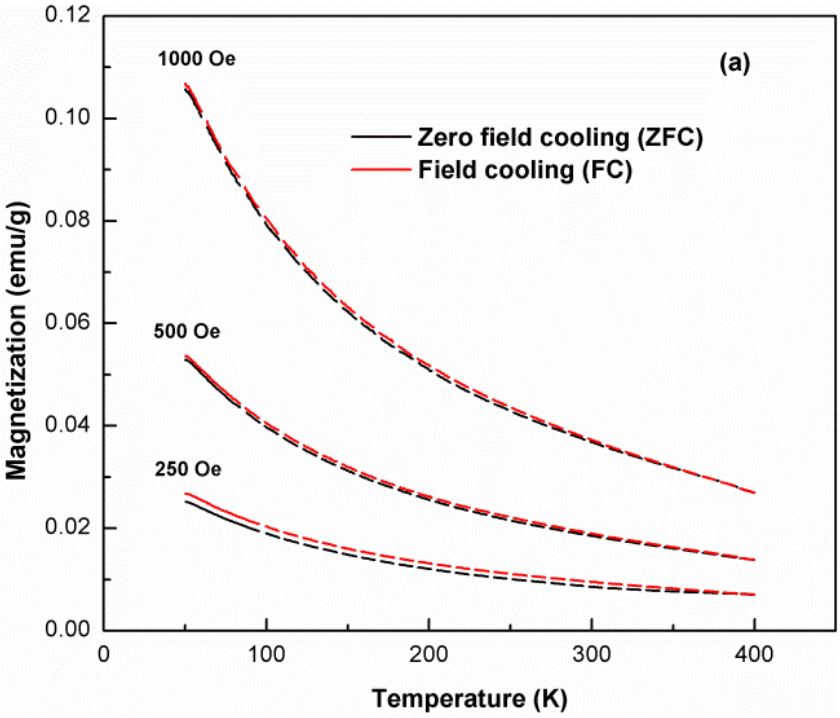

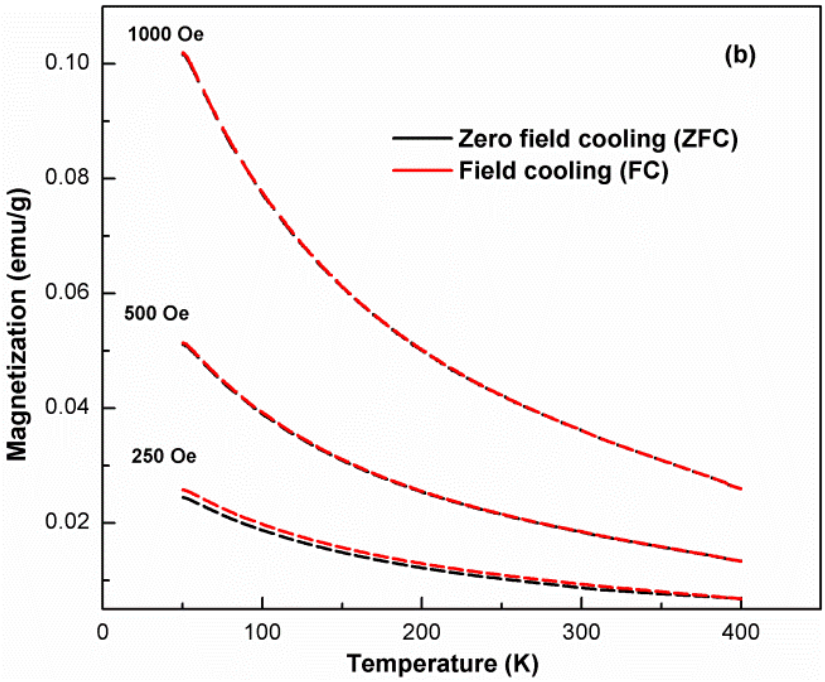

Fig. 5.24. Temperature dependent zero field cooled (ZFC) and field cooled (FC) magnetization of (a) S0 and (b) S3 samples at a different applied field

In order to find out the transition temperature (T_N), the measurement was also done below 50K with an applied field of 1000 Oe as shown in Fig. 5.25. These curves show peaks

at 47K and 45K for S0 and S3 samples respectively representing the Neel temperature (T_N) of antiferromagnetic transition. These results indicate a collinear antiferromagnetic structure without any significant spin canting for our $CoWO_4$ nanocrystals. The lower T_N for S3 sample may be due to the contribution of non-magnetic ion Pb^{2+} in the exchange interaction. Above Neel temperature, the samples show paramagnetic nature. The observed T_N for S0 sample is inconsistent with the earlier reported values as given in Table 5.9. This may be due to the crystallite size effect of the sample. The crystallite size has direct consequences on the magnetic behaviour. The smaller crystallite size in terms of nanoscale decreases the antiferromagnetic transition temperature [61]. The reduction of T_N in $CoWO_4$ nanocrystals was attributed to the effect of the small particle size probably affecting the exchange coupling in the$CoWO_4$ structure [57].

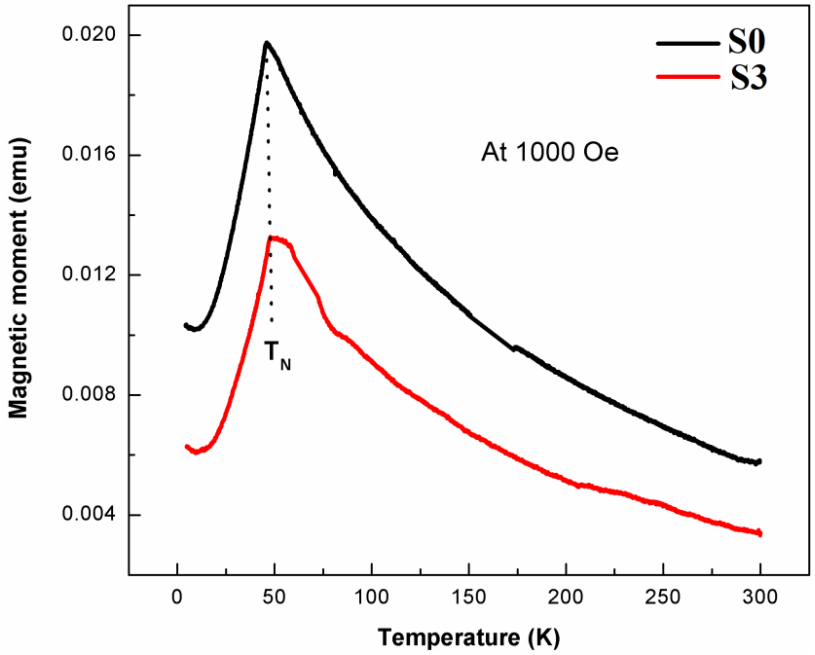

Fig. 5.25. Temperature dependent magnetization measured in the range of 4K -300K at 1000 Oe

Table.5.9 Reported work on magnetic properties of $CoWO_4$ nanomaterial.

Synthesis method	Particle size (nm)	Neel temperature (T_N) K	Nature of magnetism at RT	Ref.
Hydrothermal	30	40	Paramagnetism	[57]
Sonochemical	20	20	Paramagnetism	[29]
Coprecipitation	40-60	-	Ferromagnetism	[62]
Coprecipitation	24-40	47	Paramagnetism	This work

Magnetic susceptibility χ of the materials were calculated by the simple equation

$$\chi = \frac{M}{H} \qquad (5.18)$$

M is the magnetic dipole moment per unit volume (magnetization) and H is the magnetic field. Above the antiferromagnetic ordering temperature, the susceptibility χ follows the Curie-Weiss law [63]

$$\frac{1}{\chi} = \frac{(T-\theta_p)}{C} \qquad (5.19)$$

where θ_p and C are the Curie - Weiss temperature and Curie constant respectively. The Curie - Weiss temperature (Weiss constant) θp, typically accounts for the magnetic ordering of the electronic moments below the T_N. The plots of inverse magnetic susceptibility versus temperature of S0 and S3 samples in the range of 50-300 K are shown in Fig. 5.26(a) and 5.26(b) respectively.

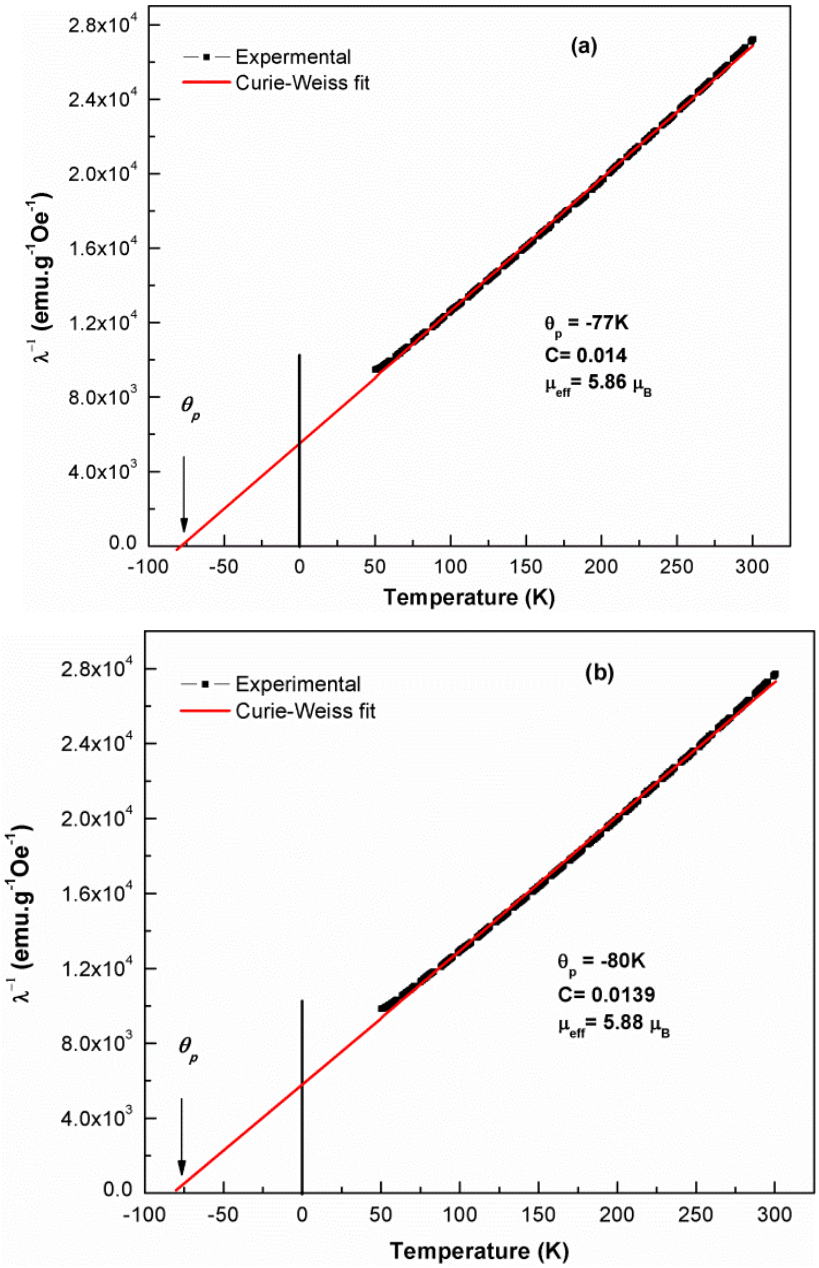

Fig. 5.26. Measured magnetic susceptibility for (a) S0 and (b) S3 samples in a magnetic field of 1000 Oe. Red line shows the inverse susceptibility fitted to Curie-Weiss law in the temperature range of 50-300 K.

A linear fit of the temperature dependence of inverse susceptibility shows a negative intercept of temperature which confirms the negative exchange interaction of the antiferromagnetic phase. The fitted reciprocal magnetic susceptibility $1/\chi$ is marked in red.

The slope of this red line is equal to 1/C and its intercept with the temperature axis is θ_P. The experimental effective magnetic moments of the samples are estimated from the equation[59]

$$\mu_{eff} = 2.83\sqrt{MC} \qquad (5.20)$$

where M is the molar mass and C is the Curie constant taken from the Curie Weiss fit shown in Fig. 5.26. The parameters obtained from the Curie-Weiss fit are μ_{eff} = 5.88 μ_B, θ p = -80 K and μ_{eff} = 5.86μ_B, θp = -77K for S0 and S3 samples respectively. The negative sign of the θp indicates the negative exchange interaction which further confirms the antiferromagnetic nature of the samples. Fractional reduction in the effective magnetic moment was observed for S3 sample as compared to S0 sample. This may be due to the reduction in concentration of Co^{2+} ions in S3 sample.

5.2.8. Electrochemical performances of samples

Fig. 5.27(a) and 5.27 (b) show the cyclic voltammetry (CV) curves measured at different scan rates for S0 and S3 samples respectively. All the curves for both the samples exhibit a pair of redox peaks indicating pseudocapacitive behaviour. This nature in these samples is due to the reversible reaction between Co^{2+} and Co^{3+} charge states[64]. With increasing scan rates from 5 to 100 mV/s, the redox peaks become wider and the anodic peak potential shifts positively and the cathodic peak potential shifts negatively. Similar effects have been observed by M. Feng et al for $CoWO_4$ and $CoWO_4$/$NiWO_4$ nanocomposites [65].

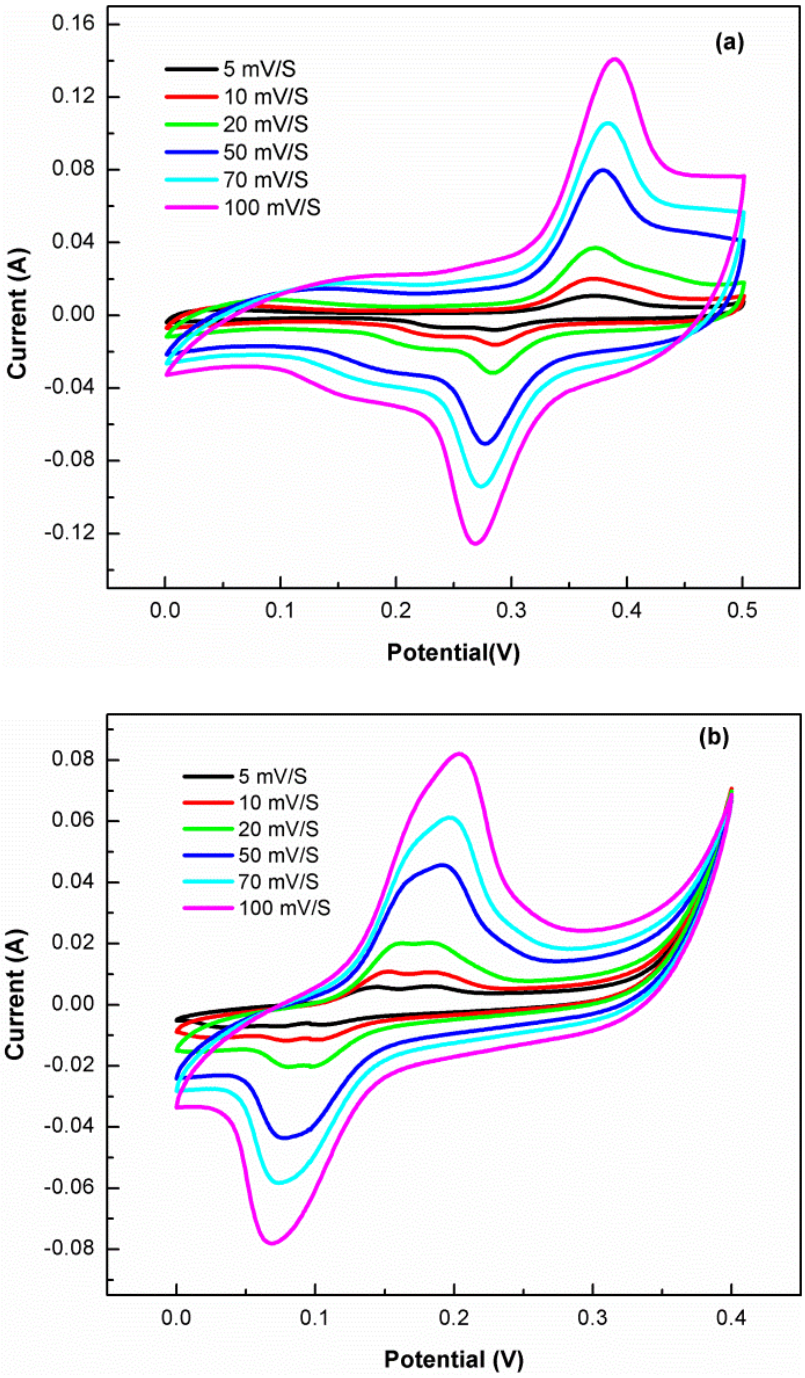

Fig. 5.27.CV curves of (a) S0 and (b) S3 samples at different scan rates.

The CV curves showing redox peaks even at a high scan rate of 100 mV/s suggest that these samples are beneficial for fast redox reactions[66]. The peak positions of the redox potential of $CoWO_4$/$PbWO_4$ (S3 sample) nanocomposites shifted towards the lower potential

as compared to $CoWO_4$ sample. This may due to the lower redox potential (0.13V) of Pb^{2+} ions of $PbWO_4$ phase as compared to that of Co^{2+} ions (0.29V) of $CoWO_4$ phase [67]. Specific capacitances (SCs) of S0 and S3 samples were calculated from the CV using following equation (5.21) and the calculated values are tabulated in Table 5.10.

$$SC = \frac{\int idv}{R \times m \times \Delta v} \qquad (5.21)$$

$$SC = \frac{i \times \Delta t}{\Delta v \times m} \qquad (5.22)$$

Where SC, i, Δt, Δv, R, and m is the specific capacitance, discharge current, discharge time, potential windows, scan rate, and mass of the active material respectively. The variation of SC vs scan rate is shown in Fig. 5.28. SC decreases with increasing scan rate. This may be due to the fact that the electrolyte ions are unable to fully access the interior surfaces of the active materials because of reduced diffusion time at high scan rate. In addition, the SCs for S0 are higher than the S3 sample for the same scan rate.

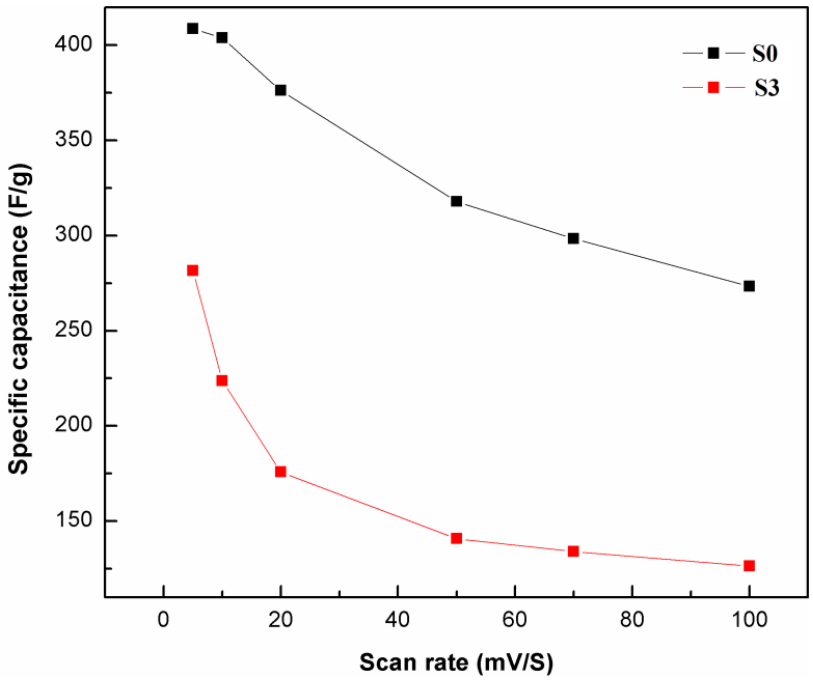

Fig. 5.28. Variation of specific capacitances of S0 and S3 samples from respective CV curves

Table.5.10 The specific capacitance of the S0 and S3 sample calculated from the CV and GCD curve.

Samples	Specific capacitance (F/g)											
	CV curve (mV/s)						Charge-Discharge curve (A/g)					
	5	10	20	50	70	100	0.5	1	2	3	4	5
S0	408	403	376	317	298	273	724	700	555	500	448	444
S3	281	223	175	140	133	126	377	333	300	300	266	250

Fig. 5.29 shows the galvanostatic charge-discharge curves for S0 and S3 samples with the potential range from 0 to 0.50 V at different current densities.

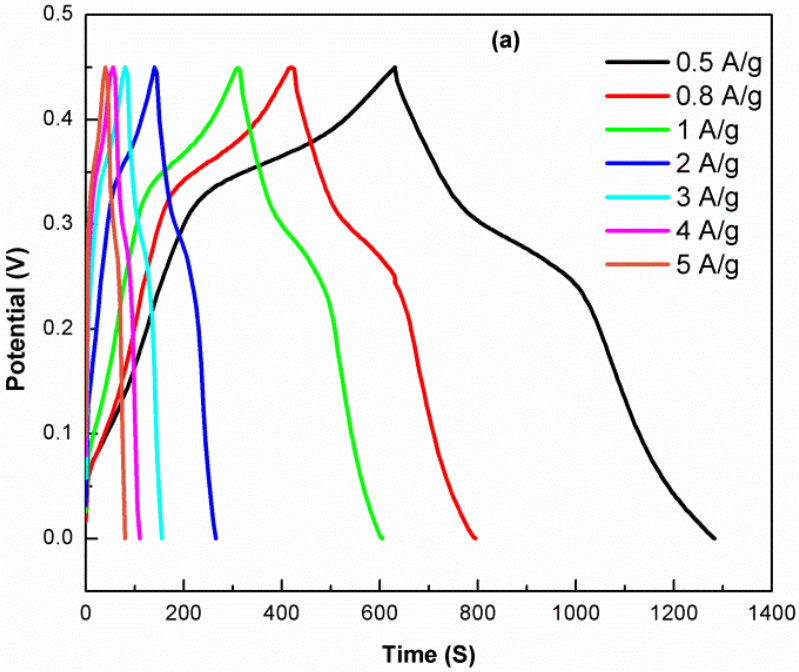

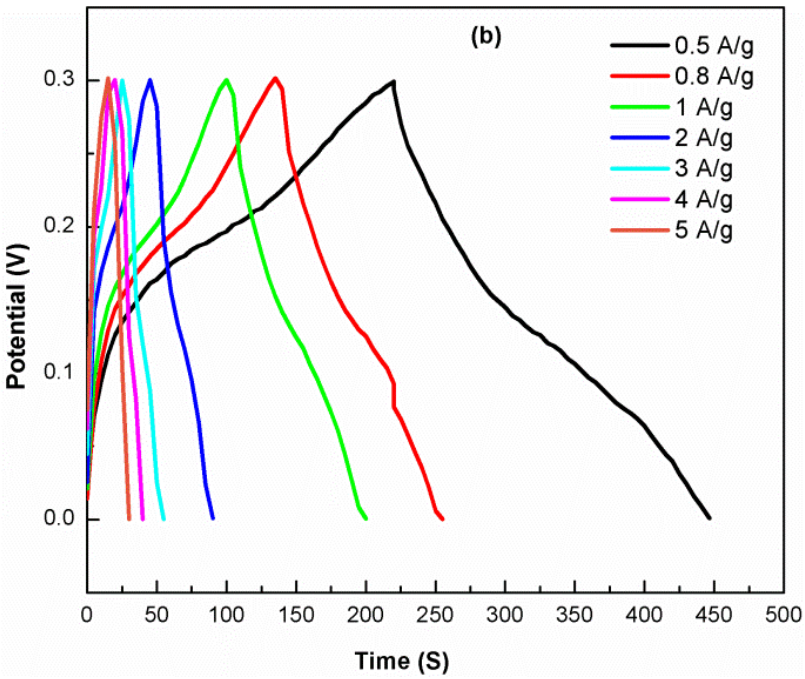

Fig. 5.29. Charge-discharge curves of the (a) S0 and (b) S3 sample at the different current densities

The specific capacitance (SC) of the sample calculated from galvanostatic charge-discharge curves using equation (5.22) and are tabulated in Table 5.8 and as a plot as shown in Fig. 5.30. SC decreased with increasing current density. This might be due to the circuitous diffusion of OH^- ions into the pores of the electrode materials [65]. SC's of the S0 sample is approximately matched with the previous report [68].

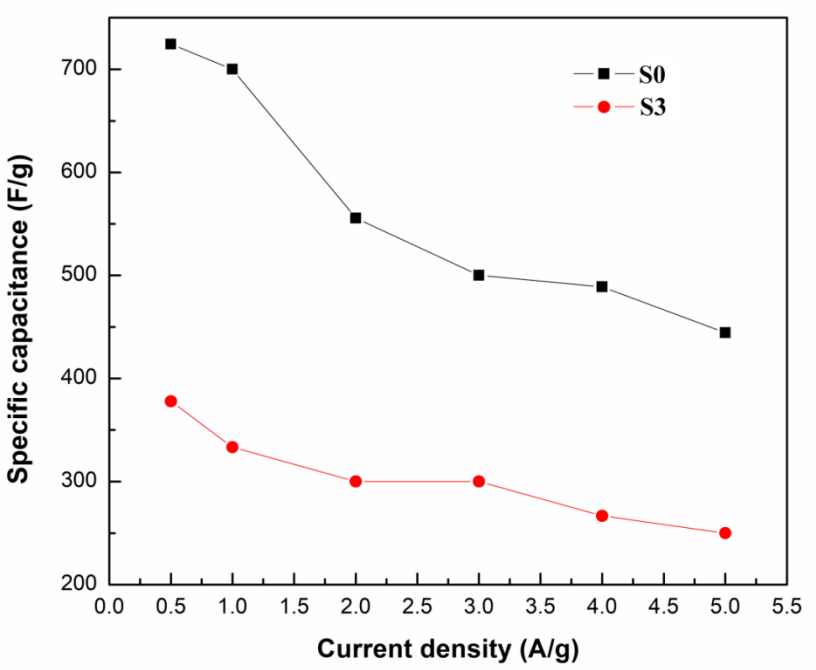

Fig. 5.30. The specific capacitance of the samples calculated from charge-discharge curves at different current densities.

Electrochemical impedance spectra are analyzed by using the Nyquist plots as shown in Fig. 5.31. The inset of the figure corresponds to the equivalent circuit. The semi-circle at the high-frequency region indicates that the capacitance is in parallel with the ionic charge transfer resistance (R_{ct}). The internal resistance (R_s) corresponds to the impedance of the electrolyte, intrinsic impedance of the electrode materials and the contact resistance between the active material and current collectors. This internal resistance can be calculated from the intercept on the real axis impedance (Z'). In the low-frequency region, the almost straight line is referred to as the Warburg resistance (W), which corresponds to the ion diffusion in the host material and diffusive resistance of the electrolyte in the electrode surface. The constant phase angle elements Q1 and Q2 represent non-ideal capacitive behaviour [66]. The fitted values are listed in Table 5.11 and the R_{ct} value of S3 sample is lower than the S0 sample.

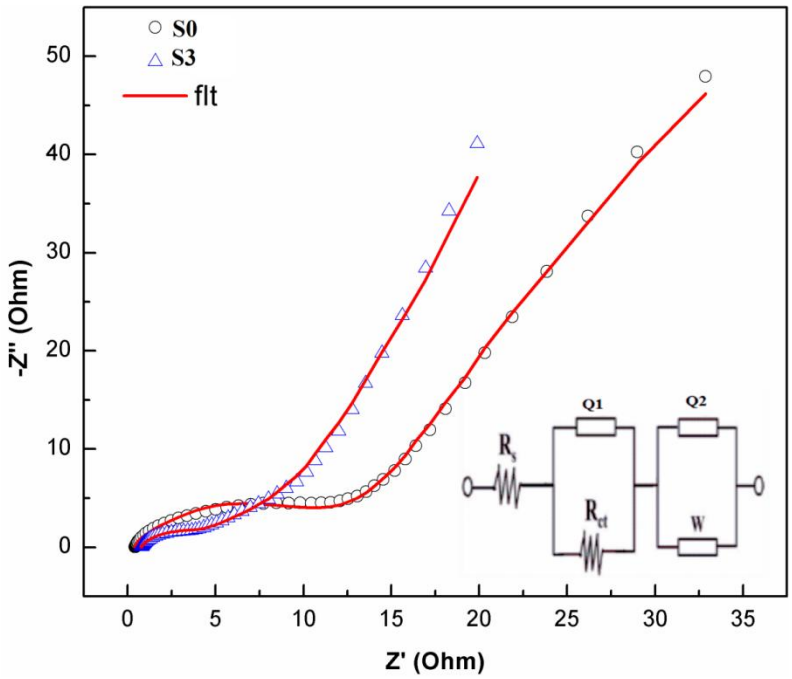

Fig. 5.31. Nyquist plots for the S0 and S3 samples. The inset shows the electrical equivalent circuit used for fitting impedance spectra.

Table 5.11 The fitted values of R_s and R_{ct} of the samples based on the equivalent circuit

Samples	R_{ct} (Ω)	R_s(Ω)	Q1(F.s)	Q2(F.s)
S0	10.58	0.403	1.753×10^{-3}	0.0564
S3	2.564	0.737	2.256×10^{-3}	0.0145

5.3. Conclusions

Dielectric properties of $CoWO_4/PbWO_4$ nanocomposites are reported for the first time. Dielectric constant ε′ at RT for all the measured frequencies are found to be maximum for S3 sample and at 500 Hz it is approximately 17 times (ε′=1803) greater than that of $CoWO_4$ (S0) sample (ε′=108). The tanδ of S3 sample (tanδ=2.8) for 500 Hz at RT is 2 times more than that of $CoWO_4$ sample (tanδ=1.3).

All the samples show dielectric constant peak at temperature T_m which is lies between 58 and 84 °C. In all our samples the T_m depends on the measurement frequency following an empirical Vogel–Fulcher and modifed Curie–Weiss laws. But XRD pattern of S0 ($CoWO_4$)

sample measured at 170°C and P–E hysteresis curves at different temperatures confirm no structural or phase transition above T_m and we conclude that our samples show relaxor like behavior. This behaviour could be explained by dipole model associated with different defects especially due to oxygen vacancies and Maxwell–Wagner model associated with electrical inhomogenity in the samples. The difference (ΔT_m) of T_m at 1 kHz and 500 kHz is highest for S0 sample and relaxor like bevaviour was not observed for the pure $PbWO_4$ phase. So frequency dependence of T_m may be attributed to the compositional disorder in the $CoWO_4$ phase of the samples due to the commonly present Co^{3+} ions in this phase. Samples sintered at high temperature (1000°C) do not show relaxor like behaviour and have less dielectric constant ε_m at T_m as compared to those sintered at 600°C. Reduction of oxygen vacancies is also one of the reasons for reduction of dielectric constant ε' and relaxor like nature of the samples sintered at 1000°C as compared to lower temperature 600°C sintered samples.

DC conductivity (intrinsic region) and ac conductivity (temperature and frequency dependent) are maximum for S3 sample. These could be because of the space charge layer (SCL) formation due to the defects at the heterostructured interface. Nonoverlapping small polaran tunneling (NSPT) and correlated barrier hopping (CBH) are suitable conduction (ac) models for all the samples.

Enhanced Seebeck coefficient and power factor were also observed for composite samples due to interfacial energy barrier scattering. The most agglomerated sample S3 (Pb/Co =0.028) has the highest values of Seebeck coefficient and power factor than the other samples. The power factor of the sample S3 is much larger than that of other samples at high temperature (above 550K) and this sample could be considered for high temperature thermoelectric applications even though it is not a typical thermoelectric material.

The S0 ($CoWO_4$) sample shows good electrochemical activity with high specific capacitance of 700 F/g and therefore it could be a prominent electrode for pseudo capacitor applications. All the samples showed paramagnetic behavior at RT and antiferromagnetic behavior below the T_N. Presence of $PbWO_4$ phase in $CoWO_4$ has not altered the magnetic properties of $CoWO_4$ except for a small reduction in magnetization and T_N.

Sample S3 (Pb/Co =0.028) may be considered as an efficient multifunctional material because of its enhanced optical properties (PL emission), electrical properties (dielectric constant, AC conductivity, DC conductivity) and thermoelectric properties (Seebeck coefficient, power factor).

References

1. Z. Kukua, E. Tomaszewicz, S. Mazur, T. Gro, H. Duda, S. Pawlus, S. M. Kaczmarek, H. Fuks, and T. Mydlarz, Philos. Mag. **92**, 4167 (2012).

2. Y. Huang, H. J. Seo, and S.-H. Doh, J. Korean Phys. Soc. **46**, 5421 (2007).

3. S. Takai, K. Sugiura, and T. Esaka, Mater. Res. Bull. **34**, 193 (1999).

4. R. Wongmaneerung, S. Choopan, R. Yimnirun, and S. Ananta, J. Alloys Compd. **509**, 3547 (2011).

5. F. Gul, M. Athar, and M. A. Farid, J. Electroceramics **40**, 300 (2018).

6. N. Ortega, A. Kumar, P. Bhattacharya, S. B. Majumder, and R. S. Katiyar, Phys. Rev. B - Condens. Matter Mater. Phys. **77**, 1 (2008).

7. R. B. Hilborn, J. Appl. Phys. **36**, 1553 (1965).

8. W. R. Agami, Phys. B Condens. Matter **534**, 17 (2018).

9. E. Birks, M. Dunce, R. Ignatans, A. Kuzmin, A. Plaude, M. Antonova, K. Kundzins, and A. Sternberg, J. Appl. Phys. **119**, 074102 (2016).

10. T. Ahmed and I. H. Lone, New J. Chem. **40**, 3216 (2016).

11. M. Tufiq Jamil, J. Ahmad, M. Saleem, and S. M. Ramay, J. Ovonic Res. **12**, 113 (2016).

12. P. Nayak, T. Badapanda, A. K. Singh, and S. Panigrahi, RSC Adv. **7**, 16319 (2017).

13. S. A. Rahman, W. R. Agami, and M. M. Eltabey, Life Sci. J. **9**, 1630 (2012).

14. H. M. EL-MALLAH, Acta Phys. Pol. A **122**, 174 (2012).

15. C. C. Wang and L. W. Zhang, Phys. Rev. B - Condens. Matter Mater. Phys. **74**, 1 (2006).

16. C. C. Wang and S. X. Dou, Solid State Commun. **149**, 2017 (2009).

17. C. J. Huang, K. Li, S. Y. Wu, X. L. Zhu, and X. M. Chen, J. Mater. **1**, 146 (2015).

18. D. I. Woodward and R. Beanland, Inorg. Chem. **53**, 8941 (2014).

19. B. P. Mandal, P. Anithakumari, S. Nigam, C. Majumder, M. Mohapatra, and A. K. Tyagi, New J. Chem. **40**, 9526 (2016).

20. E. S. Kim, C. J. Jeon, and P. G. Clem, J. Am. Ceram. Soc. **95**, 2934 (2012).

21. S. Mukherjee, C. H. Chen, C. C. Chou, K. F. Tseng, B. K. Chaudhuri, and H. D. Yang, Phys. Rev. B **82**, 104107 (2010).

22. A. V. Kalgin and S. A. Gridnev, Ferroelectrics **501**, 100 (2016).

23. I. W. Chen, J. Phys. Chem. Solids **61**, 197 (2000).

24. M. Ivanov, J. Macutkevic, R. Grigalaitis, and J. Banys, in *Magn. Ferroelectr. Multiferroic Met. Oxides* (2018), pp. 5–33.

25. R. Wördenweber, J. Schwarzkopf, E. Hollmann, A. Duk, B. Cai, and M. Schmidbauer, Appl. Phys. Lett. **103**, 1 (2013).

26. T. Wang, J. Hu, H. Yang, L. Jin, X. Wei, C. Li, F. Yan, and Y. Lin, J. Appl. Phys. **121**, 084103 (2017).

27. S. R. Alharbi, M. Alhassan, O. Jalled, S. Wageh, and A. Saeed, J. Mater. Sci. **53**, 11584 (2018).

28. A. K. Jonscher, Nature **267**, 673 (1977).

29. S. Shanmugapriya, S. Surendran, V. D. Nithya, P. Saravanan, and R. Kalai Selvan, Mater. Sci. Eng. B **214**, 57 (2016).

30. A. Singh, S. Suri, P. Kumar, B. Kaur, A. K. Thakur, and V. Singh, J. Alloys Compd. **764**,

599 (2018).

31. S. Shanmugapriya, S. Surendran, V. . Nithya, P. Saravanan, and R. Kalai Selvan, Mater. Sci. Eng. 1 (2020).

32. S. Sanna, V. Esposito, M. Christensen, and N. Pryds, APL Mater. **4**, (2016).

33. N. Pryds and V. Esposito, J. Electroceramics **38**, 1 (2017).

34. E. Fabbri, D. Pergolesi, and E. Traversa, Sci. Technol. Adv. Mater. **11**, 054503 (9pp) (2010).

35. Y. Li, Z. Wang, L. Sun, Z. Wang, S. Wang, X. Liu, and Y. Wang, Mater. Res. Bull. **50**, 36 (2014).

36. K. Funke, Solid State Ionics **105**, 195 (1998).

37. T. Zangina, J. Hassan, K. A. Matori, R. S. Azis, U. Ahmadu, and A. See, Results Phys. **6**, 719 (2016).

38. T. J. Klemmer, C. Liu, N. Shuklaa, X. W. Wua, D. Wellera, M. Tanaseb, D. E. Laughlinb, and W. A. Soffac, J. Magn. Magn. Mater. **266**, 1923 (2005).

39. A. Kocjan, M. Logar, and Z. Shen, Sci. Rep. **7**, 2541 (2017).

40. S. Alekseeva, A. B. D. S. Fanta, B. Iandolo, T. J. Antosiewicz, F. A. A. Nugroho, J. B. Wagner, A. Burrows, V. P. Zhdanov, and C. Langhammer, Nat. Commun. **8**, 1 (2017).

41. M. Jeyakanthan, U. Subramanian, and R. B. Tangsali, J. Mater. Sci. Mater. Electron. **29**, 1914 (2018).

42. A. Radon, D. Łukowiec, M. Kremzer, J. Mikuła, and P. Włodarczyk, Materials (Basel). **11**, 735 (2018).

43. A. El Bachiri, F. Bennani, and M. Bousselamti, J. Asian Ceram. Soc. **4**, 46 (2016).

44. S. Kumar, J. Pal, S. Kaur, P. S. Malhi, M. Singh, P. D. Babu, and A. Singh, J. Asian Ceram. Soc. **7**, 133 (2019).

45. A. Ray, A. Roy, S. De, S. Chatterjee, and S. Das, J. Appl. Phys. **123**, 104102 (2018).

46. R. B. Yadav, J. Phys. Chem. Solids **44**, 697 (1983).

47. S. J. Naik and A. V. Salker, Solid State Sci. **12**, 2065 (2010).

48. V. N. Shevchuk and I. V Kayun, Phys. SOLID STATE **47**, 632 (2005).

49. R. Bharati, R. A. Singh, and B. M. Wanklyn, J. Mater. Sci. **16**, 775 (1981).

50. N. F. MOTT, Philos. Mag. 465 (1995).

51. A. S. Hassanien and A. A. Akl, J. Non. Cryst. Solids **432**, 471 (2016).

52. N. Sivakumar, A. Narayanasamy, K. Shinoda, C. N. Chinnasamy, B. Jeyadevan, and J. M. Greneche, J. Appl. Phys. **102**, (2007).

53. M. Naeem, S. K. Hasanain, and A. Mumtaz, J. Phys. Condens. Matter **20**, (2008).

54. Y. Y. Li, X. Y. Qin, D. Li, J. Zhang, C. Li, Y. F. Liu, C. J. Song, H. X. Xin, and H. F. Guo, Appl. Phys. Lett. **108**, 3 (2016).

55. M. Liu and X. Y. Qin, Appl. Phys. Lett. **101**, 8 (2012).

56. J. Hee Kim, M. Jae Kim, S. Oh, J. S. Rhyee, S. D. Park, and D. Ahn, Dalt. Trans. **44**, 3185 (2015).

57. J. Deng, L. Chang, P. Wang, E. Zhang, J. Ma, and T. Wang, Cryst. Res. Technol. **47**, 1004 (2012).

58. F. Ahmadi, M. Rahimi-Nasrabadi, A. Fosooni, and M. Daneshmand, J. Mater. Sci. Mater. Electron. **27**, 9514 (2016).

59. Z. Kukua, E. Tomaszewicz, S. Mazur, T. Gro, H. Duda, S. Pawlus, S. M. Kaczmarek, H. Fuks, and T. Mydlarz, Philos. Mag. **92**, 4167 (2012).

60. A. A. Othman, M. A. Osman, E. M. M. Ibrahim, M. A. Ali, and A. G. Abd-elrahim, Mater. Sci. Eng. B **219**, 1 (2017).

61. E. M. M. Ibrahim, A. M. Abu-Dief, A. Elshafaie, and A. M. Ahmed, Mater. Chem. Phys. **192**, 41 (2017).

62. J. Juliet Josephine Joy and N. Victor Jaya, J. Mater. Sci. Mater. Electron. **24**, 1788 (2013).

63. S. R. De Oliveira Neto, E. J. Kinast, M. A. Gusmão, C. A. Dos Santos, O. Isnard, and J. B. M. Da Cunha, J. Magn. Magn. Mater. **324**, 3245 (2012).

64. X. Xing, Y. Gui, G. Zhang, and C. Song, Electrochim. Acta **157**, 15 (2015).

65. M. Feng, D. An, H. Zhang, G. Ma, C. Zhang, and Z. Ma, Int. J. Chem. Stud. **5**, 1954 (2017).

66. X. Xu, J. Gao, G. Huang, H. Qiu, Z. Wang, J. Wu, Z. Pan, and F. Xing, Electrochim. Acta **174**, 837 (2015).

67. J. F. Hunsberger, in *Handb. Chem. Phys.* (1977), pp. 141–144.

68. Y. Wang, C. Shen, L. Niu, Z. Sun, F. Ruan, M. Xu, S. Shan, C. Li, X. Liu, and Y. Gong, Mater. Chem. Phys. **182**, 394 (2016).

CHAPTER 6

CONCLUSIONS AND FUTURE SCOPE

6.1. Conclusions

In this chapter the main findings of the research work and discussion about the scope of the future work are summarized. $CoWO_4$ and $CoWO_4/PbWO_4$ (Pb/Co atomic ratios 0, 0.01, 0.015, 0.028, 0.036) nanocomposites (crystallite size between 24nm and 40nm by Scherrer formula) were successfully prepared in an aqueous medium by simple co-precipitation method without using surfactant and characterized. Larger crystallite sizes are observed for samples S2 and S3. Higher bandgap energies for more agglomerated samples S2 and S3 could be due to the orbitals overlapping of $CoWO_4$ and $PbWO_4$ compounds.

All the samples showed characteristic PL emission of $CoWO_4$. The highly agglomerated sample S3 (Pb/Co =0.028) was giving maximum PL emission which is approximately four times greater than that of S0 ($CoWO_4$) sample. Also slightly longer PL lifetime (<10% as compared to other samples) for S2 and S3 samples were observed. These are attributed to the cluster-to-cluster maximum excitonic charge-transfer (CCCT) process between $[WO_4]^{2-}$ in $PbWO_4$ and $[WO_6]^{6-}$ in $CoWO_4$ complexes on the surface due to intraparticle agglomeration leading to possible type I band alignment interfacing between $CoWO_4$ and $PbWO_4$ phases. This leads to more number of recombinations of electrons and holes in the $CoWO_4$ phase. Since luminescence is a surface property larger particle size may also contribute to the increase in the PL emission. This nanocomposite could be considered for producing blue component of emission for white LED .

Dielectric properties of $CoWO_4/PbWO_4$ nanocomposites are reported for the first time. Dielectric constant ε' at RT for all the measured frequencies are found to be maximum for S3 sample and at 500 Hz it is approximately 17 times (ε'=1803) greater than that of $CoWO_4$ (S0) sample (ε'=108). The tanδ of S3 sample (tanδ=2.8) for 500 Hz at RT is 2 times more than that of $CoWO_4$ sample (tanδ=1.3).

All the samples show dielectric constant peak at temperature T_m which is lies between 58 and 84 °C. In all our samples the T_m depends on the measurement frequency following an

empirical Vogel–Fulcher and modifed Curie–Weiss laws. But XRD pattern of S0 ($CoWO_4$) sample measured at 170°C and P–E hysteresis curves at different temperatures confirm no structural or phase transition above T_m and we conclude that our samples show relaxor like behavior. This behaviour could be explained by dipole model associated with different defects especially due to oxygen vacancies and Maxwell–Wagner model associated with electrical inhomogenity in the samples. The difference (ΔT_m) of T_m at 1 kHz and 500 kHz is highest for S0 sample and relaxor like bevaviour was not observed for the pure $PbWO_4$ phase. So frequency dependence of T_m may be attributed to the compositional disorder in the $CoWO_4$ phase of the samples due to the commonly present Co^{3+} ions in this phase. Samples sintered at high temperature (1000°C) do not show relaxor like behaviour and have less dielectric constant ε_m at T_m as compared to those sintered at 600°C. Reduction of oxygen vacancies is also one of the reasons for reduction of dielectric constant ε' and relaxor like nature of the samples sintered at 1000°C as compared to lower temperature 600°C sintered samples.

DC conductivity (intrinsic region) and ac conductivity (temperature and frequency dependent) are maximum for S3 sample. These could be because of the space charge layer (SCL) formation due to the defects at the heterostructured interface. Non-overlapping small polaron tunneling (NSPT) and correlated barrier hopping (CBH) are suitable conduction (AC) models for all the samples.

Enhanced Seebeck coefficient and power factor were also observed for composite samples due to interfacial energy barrier scattering. The most agglomerated sample S3 (Pb/Co =0.028) has the highest values of Seebeck coefficient and power factor than the other samples. The power factor of the sample S3 is much larger than that of other samples at high temperature (above 550K) and this sample could be considered for high temperature thermoelectric applications even though it is not a typical thermoelectric material.

The S0 ($CoWO_4$) sample shows good electrochemical activity with high specific capacitance of 700 F/g and therefore it could be a prominent electrode for pseudo capacitor applications. All the samples showed paramagnetic behavior at RT and antiferromagnetic behavior below the T_N. Presence of $PbWO_4$ phase in $CoWO_4$ has not altered the magnetic properties of $CoWO_4$ except for a small reduction in magnetization and T_N.

Sample S3 (Pb/Co =0.028) may be considered as an efficient multifunctional material because of its enhanced optical properties (PL emission), electrical properties (dielectric constant, AC conductivity, DC conductivity) and thermoelectric properties (Seebeck coefficient, power factor).

6.2. Future scope of the work

The results and conclusions of the present research work has the following scope for further investigations:-

- The preparation of $CoWO_4/PbWO_4$ nanocomposites by other methods (than coprecipitation) can be tried.
- Preparation of heterostructured nanocomposites with type I band alignment by the combination of metal tungstates and binary oxides for enhancing luminescence and electrical properties.
- Various shape of the particle in $CoWO_4$ and $CoWO_4/PbWO_4$ nanocomposites can be carried out and possible theory for shape formation can be predicted for photoluminescent and photocatalytic applications.
- Doping red emitting rare earth element on the $PbWO_4$ phase in $CoWO_4/PbWO_4$ nanocomposite for white light emission.
- Since $CoWO_4$ shows ferroelectric behaviour at room temperature, adding secondary ferrite phase to $CoWO_4$ could result in multiferroic material at room temperature.
- Other tungstate nanocomposites could be prepared for thermoelectric applications.

APPENDIX A

Journal Publications

Published

1. **"AC conductivity, electrochemical and magnetic studies of $CoWO_4/PbWO_4$ nanocomposites"** M. Jeyakanthan, Uma Subramanian, R. B. Tangsali, A.Ramesh. *Physica B: Condensed Matter*, 586, 412151 (2020).

2. **"Relaxor like colossal dielectric constant in $CoWO_4$ and $CoWO_4/PbWO_4$ nanocomposites"** M. Jeyakanthan, Uma Subramanian, R. B. Tangsali, Roshan Jose, Venkata saravanan K. *J Mater Sci: Mater Electron.* 30, 14657- 14668 (2019).

3. **"Enhanced Photoluminescence of $CoWO_4$in $CoWO_4/PbWO_4$ nanocomposites**"M. Jeyakanthan, Uma Subramanian, R. B. Tangsali. *J Mater Sci: Mater Electron*. 29, 1914–1924 (2018).

Under preparation

1. **"Enhanced Seebeck coefficient and DC conductivity of $CoWO_4/PbWO_4$ nanocomposites: Role of Interface"** M. Jeyakanthan, et.al (**Yet to be submitted**).

Conference Proceedings

1. **"Effect of Pb^{2+} doping on the luminescence properties of $CoWO_4$ nanoceramics"** M. Jeyakanthan, Uma Subramanian, R. B. Tangsali, *Proceedings in. Industrial Applications of Nanostructrured Materials*, **2015**, Bloomsbury Publishing India Pvt.Ltd., New Delhi, pp.193-196, **ISBN**: 978-93-85436-93-2.

PAPER PRESENTED IN CONFERENCES AND SYMPOSIUM

1. **"Size dependent photoluminescence of undoped and Mg doped CoWO4 nanomaterials for solid state lighting applications"**M. Jeyakanthan, Uma Subramanian, R. B. Tangsali, ***"International conference on Advanced nanomaterials for energy, environment and healthcare applications"***, 31August-01 september, 2018, KSR Arts and Science college for women, Tiruchengode, Tamilnadu, India.

2. **"Structural and optical properties of undoped and Dy^{3+} doped $CoWO_4$ nanomaterials prepared by coprecipitation method"** M. Jeyakanthan, Uma Subramanian, R. B. Tangsali, ***"National level symposium on Materials characterization and Manufacturing , MCM- 2016"***, 18-19 August 2016, Goa University, Goa.

3. **"Effect of Pb^{2+} doping on the luminescence properties of $CoWO_4$ nanoceramics"**M. Jeyakanthan, Uma Subramanian, R. B. Tangsali, ***"International conference on Nanomaterial and Nanotechnology, NANO-15***", 7-10 Dec, 2015, Centre for Nanoscience and Technology, KSR college of technology, Tiruchengode, Tamilnadu, India.

WORKSHOPS ATTENDED

1. Course on "**The principle and applications of electron paramagnetic resonance spectroscopy",** Organized by Global Initiative of Academic Networks in collaboration with NIT, Goa, 29th January– 9th February 2018.

2. Workshop on **"Scientific Typesetting and Diagram Plotting using LATEX",** Organized by Department of Mathematics, St. Xavier's College, Mapusa, Goa, 4th November 2017.

3. Workshop on **"Theory and practice of X-ray diffraction techniques (TPXRD) 2017",** Organized by Alagappa Chettiar College of Engineering and Technology, Karaikudi, Tamilnadu, 25th – 27 th September, 2017.

4. Workshop on **"Application of X – Rays & Neutrons in study of Condensed Matter",** Organized by Indian Association of Physics Teachers Goa Regional Council & Parvatibai Chowgule College of Arts & Science, Goa, 3rd – 4 th September 2015.

5. Course on **"Documentation Using LaTeX"** organized by Extra mural studies and Extension service, Goa**,** 24th March, 2015.

AWARDS /FELLOWSHIPS

1. **Basic Scientific Research Fellowship (BSR)** by University Grants Commission on 10th Dec. 2014 up to 10th Dec. 2019.